Experimental investigation of fluid dynamics and heat transport during single and multiple drop impingement onto a superheated wall

Alireza Gholijani

31.10.2022

TECHNISCHE UNIVERSITÄT DARMSTADT

TTD
Technische Thermodynamik

Experimental investigation of fluid dynamics and heat transport during single and multiple drop impingement onto a superheated wall

Vom Fachbereich Maschinenbau

an der Technischen Universität Darmstadt

zur Erlangung des akademischen Grades eines

Doktor-Ingenieurs (Dr.-Ing.)

genehmigte

Dissertation

vorgelegt von

M.Sc. Alireza Gholijani

aus Shiraz, Iran

Berichterstatter (1. Gutachten): Prof. Dr. -Ing. Peter Stephan
Mitberichterstatter (2. Gutachten): Apl. Prof. Dr. Tatiana Gambaryan-Roisman
Mitberichterstatter (3. Gutachten): Prof. Dr.-Ing. Jeanette Hussong

Technische Thermodynamik
Tag der Einreichung: 31.10.2022
Tag der mündlichen Prüfung: 28.02.2023

Darmstadt, 2023

Erklärung

Hiermit erkläre ich, dass ich die vorliegende Arbeit, abgesehen von den in ihr ausdrücklich genannten Hilfen, selbständig verfasst habe.

Darmstadt, 31.10.2022

Abstract

This thesis is devoted to experimental investigation of hydrodynamics and heat transport during the impingement of a single drop and multiple drops onto a wall, whose temperature is above the liquid saturation temperature and below the onset of nucleate boiling. The drop impingement onto heated surfaces occurs in many industrial applications, for instance, spray cooling, which is considered among the most efficient cooling methods. By considering the fact that spray systems are comprised of an enormous number of interacting drops, a detailed characterization of fluid dynamics and heat transport mechanisms during the impact of individual drops throughout spraying process is complicated. Thus, many studies concentrate on fluid dynamics and heat transport mechanisms of a single drop or a group of drops impacting onto a surface under well-controlled conditions to obtain detailed knowledge of underlying physics of the spray cooling process.

Although the drop dynamics during the isothermal drop impingement (non-heated surface) has been widely studied in the past decades, the fluid dynamics and heat transfer to the drop during the impingement process in the non-isothermal case (heated surface), in which evaporation plays a crucial role is not fully understood yet. Numerous studies on pool boiling and meniscus evaporation have reported a temperature minimum and accordingly, a huge evaporation rate in proximity of the three-phase contact line, where solid, liquid, and gas phases meet each other. The evaporation in this region constitutes a significant fraction of the overall heat transfer. Hence, any alteration in physical or thermodynamical parameter on the three-phase contact

Kurzfassung

Diese Arbeit widmet sich experimentellen Untersuchungen zur Hydrodynamik und zum Wärmetransport beim Aufprall eines einzelnen sowie mehrerer Tropfen auf eine Wand, deren Temperatur oberhalb der Sättigungstemperatur der Flüssigkeit und unterhalb des Blasensiedebeginns liegt. Der Tropfenaufprall auf beheizte Oberflächen kommt in vielen industriellen Anwendungen vor, z.B. bei der Sprühkühlung, die als eine der effizientesten Kühlmethoden gilt. In Anbetracht der Tatsache, dass Sprühsysteme aus einer enormen Anzahl von interagierenden Tropfen bestehen, ist eine detaillierte Charakterisierung der Fluiddynamik und der Wärmetransportmechanismen während des Auftreffens einzelner Tropfen während des Sprühvorgangs kompliziert. Daher konzentrieren sich viele Studien auf die Fluiddynamik und der Wärmetransportmechanismen eines einzelnen Tropfens, der unter gut kontrollierten Bedingungen auf eine Oberfläche auftrifft, um detaillierte Kenntnisse über die zugrunde liegende Physik des Sprühkühlungsprozesses zu erhalten.

Obwohl die Tropfendynamik während des isothermen Tropfenaufpralls (nicht beheizte Oberfläche) in den letzten Jahrzehnten umfassend untersucht wurde, ist die Fluiddynamik und der Wärmeübergang auf den Tropfen während des Aufprallprozesses im nicht-isothermen Fall (beheizte Oberfläche), bei dem die Verdampfung eine entscheidende Rolle spielt, noch nicht vollständig verstanden. Zahlreiche Studien zum Behältersieden und zur Meniskusverdampfung haben ein Temperaturminimum und dementsprechend eine hohe Verdampfungsrate in der Nähe der Dreiphasen-Kontaktlinie, wo

line could strongly affect the overall heat transfer. Some examples of influencing parameters are wall superheat, impact velocity, drop size, system pressure, and surface morphology. These parameters also affect the convection, considered to be the main heat transfer mechanism at the early stages of drop impingement. Therefore, the effects of aforementioned parameters on fluid dynamics and heat transport are investigated in the scope of this thesis.

This study employs a high-resolution temperature measurement technique, allowing high temporal and spatial resolution of the heat flux. It is an accurate and detailed approach to investigate the drop hydrodynamics and heat transport mechanism during non-isothermal drop impact.

The experimental results reveal that higher wall superheats, higher impact velocities, larger drop diameters, and lower system pressures each result in increasing heat flow to the drop after the impingement. The maximum spreading radius after impingement increases with the increase of impact velocity and impact diameter, and decreases with the increase of wall superheat and system pressure. Besides, the impact of a drop onto a porous surface is accompanied by lower heat flow at the early stages of impact, while it enhances significantly at the late stages of impact. The heat flow enhancement is due to the large solid–liquid contact area caused by the drop pinning effect.

The last part of the thesis focuses on impingement of multiple drops onto a superheated wall as it represents a next step in modeling of spray systems compared to a single drop impact. Multiple drop impingement is far less investigated than the single drop impingement due to its complexity of the fluid mechanic and heat transfer mechanisms. In this thesis, hydrodynamics and heat transport during vertical and horizontal coalescence of multiple drops (successive and simultaneous drop impact) over a heated surface are ad-

feste, flüssige und gasförmige Phasen aufeinander treffen, festgestellt. Die Verdampfung in diesem Bereich macht einen signifikanten Anteil am gesamten Wärmeübergang aus. Diese Parameter wirken sich auch auf die Konvektion aus, die als Hauptwärmetransportmechanismus in den frühen Phasen des Tropfenaufpralls gilt. Daher kann jede Änderung der physikalischen oder thermodynamischen Parameter an der Dreiphasen-Kontaktlinie den gesamten Wärmeübergang stark beeinflussen. Einige Beispiele für beeinflussende Parameter sind Wandüberhitzung, Aufprallgeschwindigkeit, Tropfengröße, Systemdruck und Oberflächenmorphologie. Daher werden im Rahmen dieser Arbeit die Auswirkungen der genannten Parameter auf die Fluiddynamik und den Wärmetransport untersucht.

In dieser Studie wird eine hochauflösende Temperaturmesstechnik eingesetzt, die eine hohe zeitliche und räumliche Auflösung des Wärmestroms ermöglicht. Es handelt sich um einen genauen und detaillierten Ansatz zur Untersuchung der Hydrodynamik des Tropfens und des Wärmetransportmechanismus beim nicht-isothermen Tropfenaufprall.

Die experimentellen Ergebnisse zeigen, dass höhere Wandüberhitzungen, höhere Aufprallgeschwindigkeiten, größere Tropfendurchmesser und niedrigere Systemdrücke jeweils zu einem zunehmenden Wärmestrom zum Tropfen nach dem Aufprallführen. Der maximale Ausbreitungsradius nach dem Aufprall nimmt mit der Erhöhung der Aufprallgeschwindigkeit und des Aufpralldurchmessers zu und sinkt durch die Erhöhung der Wandüberhitzung und des Systemdrucks. Außerdem kommt es beim Aufprall eines Tropfens auf eine poröse Oberfläche zu einem geringeren Wärmestrom in den frühen Phasen des Aufpralls, während er in den späten Phasen des Aufpralls deutlich zunimmt. Die Erhöhung des Wärmestroms ist auf die große Fest-Flüssig-Kontaktfläche zurückzuführen, die durch den Tropfen-

dressed, as well.
The investigations reveal that the solid–liquid contact area and accordingly heat flow rise after successive impacts. However, drop coalescence during simultaneous drop impingement delivers lower heat flow in comparison with non-coalescence cases.
The experimental results of single drop impact onto a bare heater and at atmospheric pressure are compared against the numerical model developed in the author's institute. A good agreement between measurements and model predictions has been observed. The simulation results are used to present a more accurate analysis and interpretation of the experimental results.

Pinning-Effekt verursacht wird.
Der letzte Teil der Arbeit konzentriert sich auf das Auftreffen mehrerer Tropfen auf eine überhitzte Wand, da dies industrielle Sprühsysteme besser beschreibt, als das Auftreffen einzelner Tropfen. Der Mehrfachtropfenaufprall ist aufgrund der Komplexität der Strömungsmechanik und der Wärmeübertragungsmechanismen weit weniger untersucht als der Einzeltropfenaufprall. In dieser Arbeit werden auch die Hydrodynamik und der Wärmetransport während der vertikalen und horizontalen Koaleszenz mehrerer Tropfen (sukzessiver und gleichzeitiger Tropfenaufprall) auf einer beheizten Oberfläche behandelt.
Die Untersuchungen zeigen, dass die Fest-Flüssig-Kontaktfläche und damit der Wärmestrom nach aufeinanderfolgenden Aufprallvorgängen ansteigen. Allerdings liefert die Tropfenkoaleszenz beim gleichzeitigen Tropfenaufprall einen geringeren Wärmestrom im Vergleich zu den Fällen ohne Koaleszenz.
Die experimentellen Ergebnisse des Einzeltropfenaufpralls auf einen glatten Heizer und bei atmosphärischem Druck werden mit einem numerischen Modell verglichen, das im Institut des Autors entwickelt wurde. Es wurde eine gute Übereinstimmung zwischen den Messungen und den Modellvorhersagen beobachtet. Die Simulationsergebnisse werden verwendet, um eine genauere Analyse und Interpretation der experimentellen Ergebnisse zu präsentieren.

Acknowledgments

I would like to express my deep and sincere gratitude to my research supervisors, **Prof. Peter Stephan** and **Apl. Prof. Dr. Sc. Tatiana Gambaryan-Roisman** for being such a inspiring, motivating and helpful people. I am extremely grateful to them for giving me the opportunity to work on this wonderful research project. Their supervision played the biggest role in shaping me as a researcher. I am also thankful to them for fostering a great working environment in the institute.

I am thankful to the Deutsche Forschungsgemeinschaft (DFG, German Research Foundation) - Project SFB-TRR 75, Project number 84292822 for the financial support and the several training activities which helped me to grow.

I am thankful to all the wonderful colleagues whom I got the opportunity to work with. This includes all of my co-fellows at SFB-TRR 75 and my colleagues at TU Darmstadt. **Iman**, **Abhijeet**, **Christiane**, **Jan**, **Benedikt**, and **Henrik**, I really enjoyed our cooperations and discussions covering a broad range of topics. It was an enjoyable experience sharing my office with **Jörn** and **Benjamin**.

I am grateful that I had the support of capable technical staff all throughout my PhD research. I would like to specially thank **Robert Schrod** and **Roland Berntheisel**.

This thesis would not exist in it's present form if it wasn't for the sincere efforts of my students, **Gokul Ramanan Parandaman**, **Ahmed Dhia Bahrouni**, **Christian Ehrt**, and **Hossein Ghaemi**. Their cooperations in performing the experiments and evaluation of the results are commendable.

I am grateful to all of my German language instructors, specially **Christina Braun**, under whose guidance I undertook my journey from almost elementary German skills to the C1-level.

In between stress at work, failed experiments and rejected papers, it is with family and friends that I found my inner peace. My parents, sisters always believed in me and motivated me to give my best. They were always there as a strong pillar of support.

Darmstadt, 31.10.2022 Alireza Gholijani

Contents

Nomenclature

Latin symbol	Description	Unit
A	surface area	m^2
c	thermal capacity	J kg^{-1} K^{-1}
c_p	thermal capacity at constant pressure	J kg^{-1} K^{-1}
D	diameter	m
d	distance	m
E	cumulative heat flow	J
E^*	dimensionless cumulative heat flow	
e	spacing parameter	
F	force	N
F	volume fraction	
f	volumetric force	N m^{-3}
f	frequency	Hz
g	gravitational acceleration on earth	m s^{-2}
h	height / thickness	m
h_{lv}	latent heat of vaporization	J kg^{-1}
I	electrical current	A
I_{dig}	digital intensity	
J	radiative energy flow	W
j	radiative energy flux	W m^{-2}
k	absorption coefficient	m^{-1}
l	length	m
n	unit normal vector	m
n	index of refraction	
p	pressure	N m^{-2}
$\dot{Q}$	heat flow	W
$\dot{Q}^*$	dimensionless heat flow	
$\dot{q}$	heat flux	W m^{-2}
R	radius	m
R_{hl}	electrical resistance of the heating layer	Ω
S	spreading ratio	
T	temperature	K
T′	temperature	°C
t	time	s
t′	time instant	
U	voltage	V
u,u	velocity	m s^{-1}
V	volume	m^3
w	width	m
Δx_{res}	resolution	m $pixel^{-1}$
x, y, z	coordinates	m

Greek symbol	Description	Unit
α	thermal diffusivity	$m^2\ s^{-1}$
ε	emissivity	
κ	interface curvature	m^{-1}
λ	thermal conductivity	$W\ m^{-1}\ K^{-1}$
μ	dynamic viscosity	$Pa\ s^{-1}$
ν	kinematic viscosity	$m^2\ s^{-1}$
θ	angle	$^\circ$
ρ	density	$kg\ m^{-3}$
ρ_{rad}	reflectivity	
Σ	source term	various
σ	surface tension	$N\ m^{-1}$
σ_{SB}	Stefan-Boltzmann constant	$W\ m^{-2}\ K^{-4}$
τ	dimensionless time	
τ_{rad}	transmittance	

Subscript	Description
0	initial conditions
1.4301	stainless steel alloy 1.4301 (X 5 CrNi 18 − 10)
20 °C	at 20 °C
abs	absolute
ad	adsorbed layer
av	average
B/W	high speed black and white camera
CaF	calcium fluoride
calc	calculated
calib	calibration
CL	contact line
crit	critical
Cr	chromium
CrN	chromium nitride
c	computational cell
ctr	center
DAQ	data acquisition system
dig	digital
evap	evaporative
exp	experiment
hl	heating layer
in	input
int	liquid–vapor interface
IR	high speed infrared camera
l	liquid
loss	due to losses
mat	nanofiber mat
max	maximal
mic	micro region
min	minimal

Subscript	Description
N	number of impact
num	numerical
PEEK	poly-ether-ether-ketone
pix	pixel
PS	power supply
Pt100	measured by Pt100
R	reduced (ratio of value / value at the crit. point)
rad	radiation
rel	relative
sat	saturation
sim	simulation
stat	statistics
sur	surrounding
TC	measured by thermocouples
thres	threshold
v	vapor
w	at the heater wall

Abbreviation	Description
B/W	black and white
CaF_2	calcium fluoride
CFD	Computational Fluid Dynamics
CHF	critical heat flux
Cr	chromium
CrN	chromium nitride
DAQ	data acquisition system
FOV	field of view
HF	heat flux
IR	infrared
LCT	liquid crystal thermography
LIF	laser induced fluorescence
LIP	laser induced phosphorescence
LWIR	long-wave infrared
MWIR	mid-wave infrared
NETD	noise equivalent temperature difference
NEHFD	noise equivalent heat flux difference
PEEK	poly-ether-ether-ketone
Pt100	Platinum temperature sensor, 100 ω resistance at 0 °C
PVD	physical vapor deposition
SEM	scanning electron microscope
SWIR	short-wave infrared
TC	thermocouple
Temp.	temperature
TLC	thermochromic liquid crystal
TTD	Institut für Technische Thermodynamik, TU Darmstadt

Dimensionless Number	Description
$Bo = \frac{\rho_l g D_0^2}{4\sigma}$	Bond number
$Ca = \frac{We}{Re} = \frac{\mu_l u_0}{\sigma}$	Capillary number
$Co = \frac{v_0 \Delta t_{num}}{\Delta x_{num}}$	Courant number
$Ja = \frac{c_l (T_w - T_{sat})}{h_{lv}}$	Jakob number
$Oh = \frac{\sqrt{We}}{Re} = \frac{\mu_l}{\sqrt{\rho_l D_0 \sigma}}$	Ohnesorge number
$Pr = \frac{\nu}{\alpha} = \frac{\mu_l c_l}{\lambda_l}$	Prandtl number
$Re = \frac{\rho_l D_0 u_0}{\mu_l}$	Reynolds number
$We = \frac{\rho_l D_0 u_0^2}{\sigma}$	Weber number

1 Introduction

1.1 Motivation

The impact of drops onto dry solid surfaces or a liquid film has been studied for over a century, not only because of the numerous physical phenomena of fundamental interest involved but also due to its importance in various technical applications such as spray cooling, spray painting, combustion systems, coating processes, steam turbine blade operations, etc. Early studies of the impact process were largely phenomenological in nature, determining relevant parameters influencing the spreading of the liquid film on the surface and also the final outcome of the impact. The recent studies attempt to quantify the influence of individual parameters in order to attain predictive capabilities of the impact process.

Despite numerous drop impact studies in past decades, the hydrodynamics of drop impacting onto a solid wall or a liquid film is still not fully understood, especially when heat transfer and evaporation during the impingement process are coupled with hydrodynamics. Lack of knowledge in non-isothermal drop impact hinders the prediction of the spray cooling phenomenon, where numerous drops interact with a dry or partially wetted hot surface. In spray cooling, the interaction between fluid and solid is a key parameter affecting heat transfer performance.

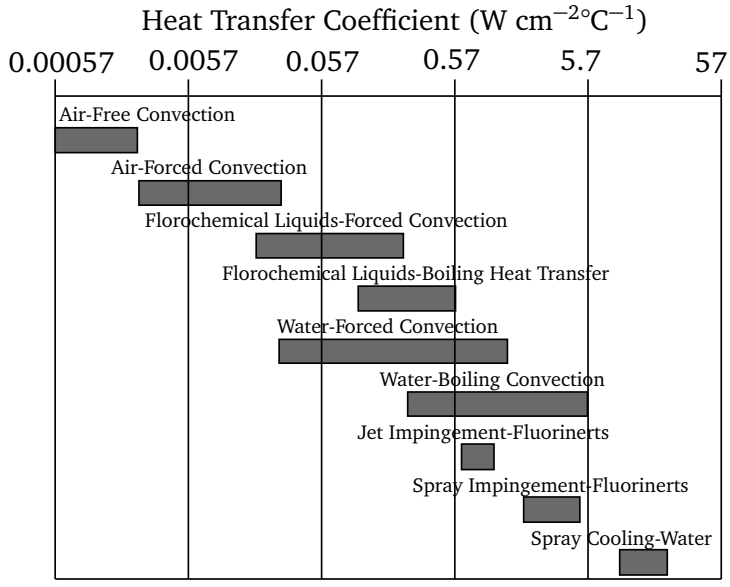

Figure 1.1.: Heat transfer coefficient for cooling techniques [1].

As depicted in figure 1.1, the heat transfer coefficient of spray cooling is between 1 and 4 orders of magnitude larger than that of single-phase natural or forced convective heat transfer. It performs even better than other two-phase cooling methods such as nucleate boiling while at the same time a reduced amount of fluid is needed [2]. Therefore, spray cooling technology is widely used in many technical applications, in which extremely high heat fluxes are required to be dissipated. Examples are die forging and hot rolling [3], light-water reactors [4], as well

as cryogenic cooling of human tissue [5]. Moreover, spray cooling is a promising technique for cooling of electronic devices (e.g., computer chips and sensors) [6], since miniaturization and breakthrough developments of these devices lead to continuously increasing the heat produced per unit area. In order to prevent the damages of such devices, heat removal from their surfaces should be uniform.

To comprehend the spray cooling operation, the investigation of relevant basic processes such as single drop impact, drop coalescence during the impact of multiple drops onto a heated solid dry wall or a liquid film becomes significant. Extensive research studies on single drop impact over non-heated and heated surfaces are available in the literature. However, the impact of multiple drops has not been sufficiently studied yet due to additional complexity associated with the underlying physics of these drop systems compared to the single drop impact. The present work deals with the experimental investigation of a single drop and multiple drops impinging onto a heated surface.

There are several methods to enhance heat transfer during spray cooling or pool boiling significantly. One promising and low-cost method is the surface modification, e.g., by using an electrospun nanofiber mat. Accordingly, a single drop impact onto a heated surface covered with an electrospun nanofiber mat is also addressed in the framework of this study.

In order to enhance the basic knowledge regarding the single and multiple drop impact in terms of hydrodynamics and heat transfer, numerous experiments and parametric studies are aimed in this work. This work employs a high temporal and spatial resolution temperature measurement technique to drive the heat flux with a high resolution. This is essential for obtaining detailed knowledge of hydrodynamics and heat transfer during the impact of one drop or a group of drops onto a heated surface. Together with an appropriate model, these experimental results can contribute to better understanding of the mechanisms of spray cooling that could be used for the improvement of spray systems in the future. This can be considered as a step towards a better understanding of the underlying physics occurring in spray cooling and, in general, any technologies where drop–wall interaction is relevant.

1.2 Structure of the thesis

A summary of the content and scope of the chapters presented in this thesis is given in the following:

Chapter 1 contains a short introduction to various cooling techniques and the motivation of this work. It is shown that spray cooling is considered among the most effective methods for heat removal applications, and to comprehend the underlying physics in spray systems, investigations of the influence of governing parameters on hydrodynamics and heat transport during drop–wall and drop–drop interactions are essential.

Chapter 2 describes the thermodynamic and hydrodynamic phenomena followed by regime classification under different substrate temperatures and impact conditions during drop impact onto a heated surface. Then the scope of this thesis is defined within the wide field of single and multiple drop impingement regimes. A brief overview of the existing numerical and experimental

works from the literature is presented. At the end of this chapter, the objectives of this thesis are outlined.

Chapter 3 provides a detailed description of the experimental concept. A survey of available drop generation methods and high resolution temperature measurement techniques with respect to the measurement task is given. The experimental setup and procedure are introduced along with the parameter space for which experiments have been conducted. The applied measurement methods are described along with the data treatment and data reduction techniques.

Chapter 4 is devoted to a brief description of the numerical model employed for the simulation of the single drop impingement onto a superheated surface. This chapter also contains the relevant assumptions and equations related to the heat and fluid flow in micro and macro scales during drop impingement.

In **Chapter 5**, the main results of this thesis are presented. The results are divided into single and multiple drop impingement sections. Initially, the influence of wall superheat, impact velocity, impact diameter, system pressure, and surface structure on hydrodynamics and heat transport during the impingement of a single drop onto the heater substrate are presented. Following that, the multiple drop impingement, where the drops coalescing either vertically or horizontally over the heater substrate, are presented. For the former mode (i.e., vertical coalescence), the influence of wall superheat and drop generation frequency are discussed, whereas for the latter (i.e., horizontal coalescence), the influence of spacing parameter, wall superheat, and the time interval between the impact are given.

Chapter 6 is the closing section, which contains a summary of the thesis, the main findings and an outlook for future research.

2 State of the art

Section 2.1 in the present chapter provides phenomenological description of the single drop impingement phenomena and introduces the governing dimensionless parameters. A literature review of single and multiple drop impingement is outlined in Section 2.2. The chapter is concluded with the aims and objectives of the present thesis in Section 2.3. Parts of the following Sections are published in [7].

2.1 Single drop impingement phenomena and governing dimensionless parameters

The phenomenology of the drop impingement process depends upon the boundary and initial conditions. In the following, the classification of various possible scenarios according to these boundary and initial conditions is described, and the relevant conditions used in the current study is given. Thereafter, possible impingement outcomes are outlined.

The outcomes of isothermal single drop impact depend upon the impact Reynolds number, which expresses the ratio of the inertial and viscous forces:

$$Re = \frac{\rho_l D_0 u_0}{\mu_l}, \tag{2.1}$$

the Weber number, which represents the ratio of the inertial and surface tension forces:

$$We = \frac{\rho_l D_0 u_0^2}{\sigma}, \tag{2.2}$$

the Bond number, which expresses the ratio of the gravitational force and surface tension force:

$$Bo = \frac{\rho_l g D_0^2}{4\sigma}, \tag{2.3}$$

the surrounding gas pressure, and the surface morphology and wettability. In these definitions, D_0 denotes the drop diameter, u_0 is the impact velocity, ρ_l and μ_l are the liquid density and dynamic viscosity, respectively, σ is the surface tension, and g denotes the gravitational acceleration. In some cases, it is more convenient to work with combinations of the Reynolds and Weber numbers. Among these combinations are the capillary number

$$Ca = \frac{We}{Re} = \frac{\mu_l u_0}{\sigma}, \tag{2.4}$$

and Ohnesorge number:

$$Oh = \frac{\sqrt{We}}{Re} = \frac{\mu_l}{\sqrt{\rho_l D_0 \sigma}}. \tag{2.5}$$

For the description of the phase change heat transfer, the Jakob number is typically applied. This number represents the ratio of sensible heat and latent heat transferred during the heat transport and phase change process:

$$Ja = \frac{c_l(T_\mathrm{w} - T_\mathrm{sat})}{h_\mathrm{lv}}\,, \tag{2.6}$$

where T_w and T_sat are the temperature at the heater wall and saturation temperature of the liquid, respectively. c_l denotes the specific heat and h_lv the enthalpy of vaporization of the liquid.

The thermal properties of the liquid are represented by the Prandtl number, which is the ratio of the viscous diffusion rate and thermal diffusion rate:

$$Pr = \frac{\nu}{\alpha} = \frac{\mu_\mathrm{l} c_\mathrm{l}}{\lambda_\mathrm{l}}\,, \tag{2.7}$$

where ν is kinematic viscosity, α thermal diffusivity, and λ_l thermal conductivity of the liquid.

The dimensionless time, τ, which represents the ratio of the inertial time scale and actual time is defined as follows:

$$\tau = \frac{u_0 t}{D_0}\,, \tag{2.8}$$

where t denotes the time. The spreading ratio, S, is defined as:

$$S = \frac{D_\mathrm{cl}}{D_0}\,, \tag{2.9}$$

where D_cl denotes the diameter of the wetted region.

The dimensionless cumulative heat flow is defined as the ratio of the cumulative heat flow transferred to the drop, E, and the amount of energy required to evaporate it completely

$$E^* = \frac{6E}{\pi \rho_\mathrm{l} D_0^3 h_\mathrm{lv}}\,. \tag{2.10}$$

The dimensionless representation of heat flow is given by the derivative of E^* with respect to the dimensionless time via

$$\dot{Q}^* = \frac{6\dot{Q}}{\pi \rho_\mathrm{l} D_0^2 u_0 h_\mathrm{lv}}\,, \tag{2.11}$$

where $\dot{Q}$ denotes the total heat flow at the liquid–solid interface.

2.1.1 Classification of impingement scenarios

Figure 2.1 presents an overview of possible combinations of hydrodynamic boundary conditions for single and multiple drop impingement inspired by [8, 9]. Different scenarios can be defined

based on liquid drop shape, hydrodynamic condition, drop composition, drop impact mode and configurations, impact angle, and the constitution of the target surface.

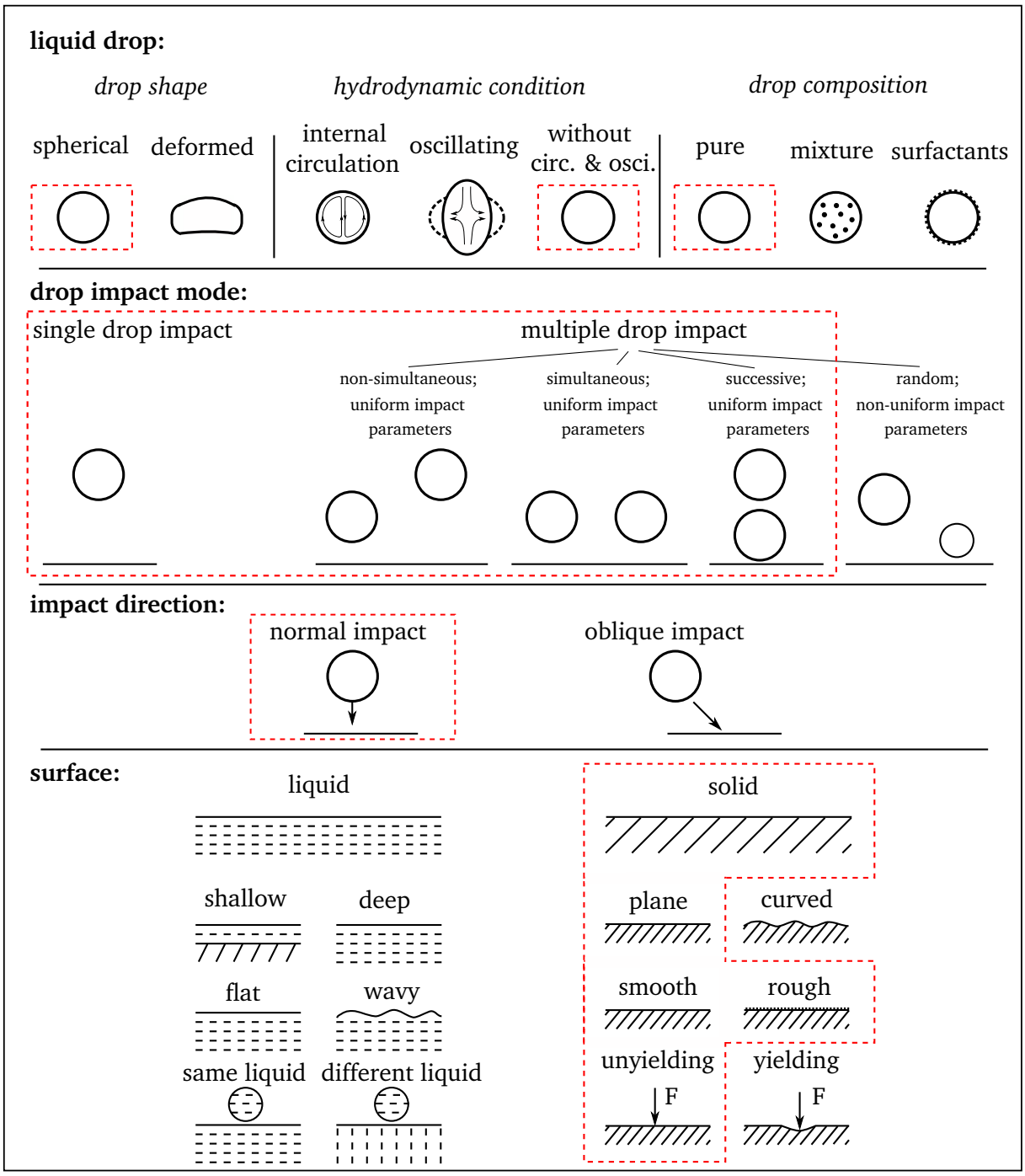

Figure 2.1.: Classifications of possible impingement scenarios inspired by [8, 9]. The conditions relevant to this thesis are indicated by red-dashed boxes.

The focus of this thesis is on spherical drops of a pure liquid without internal circulation and oscillation. In fact, the slight deformation or oscillation of the drop, especially at high system pressures due to low liquid density and surface tension, and in high drop generation frequencies due to fast production of the liquid drop, is undeniable. The working fluid used in this study is a Newtonian fluid.

In terms of drop impact mode and configurations, the normal impact of single and multiple drops is considered in this study. In the case of multiple drop impact, the vertical and horizontal coalescence of two drops with uniform impact parameters are taken into account.

The target surface is plane and rigid, whose deformation after the impact is negligible. The investigations have been performed for both smooth and rough surfaces (heater covered with a porous nanofiber mat).

Isothermal drop impact

The hydrodynamic behavior of isothermal drop impact is governed by the impact parameters (e.g., impact velocity and impact diameter) and surface properties of the wall. Figure 2.2 shows the systematic classification of impact outcomes for an isothermal drop impact, which have been observed in the work of Rioboo et al. [10].

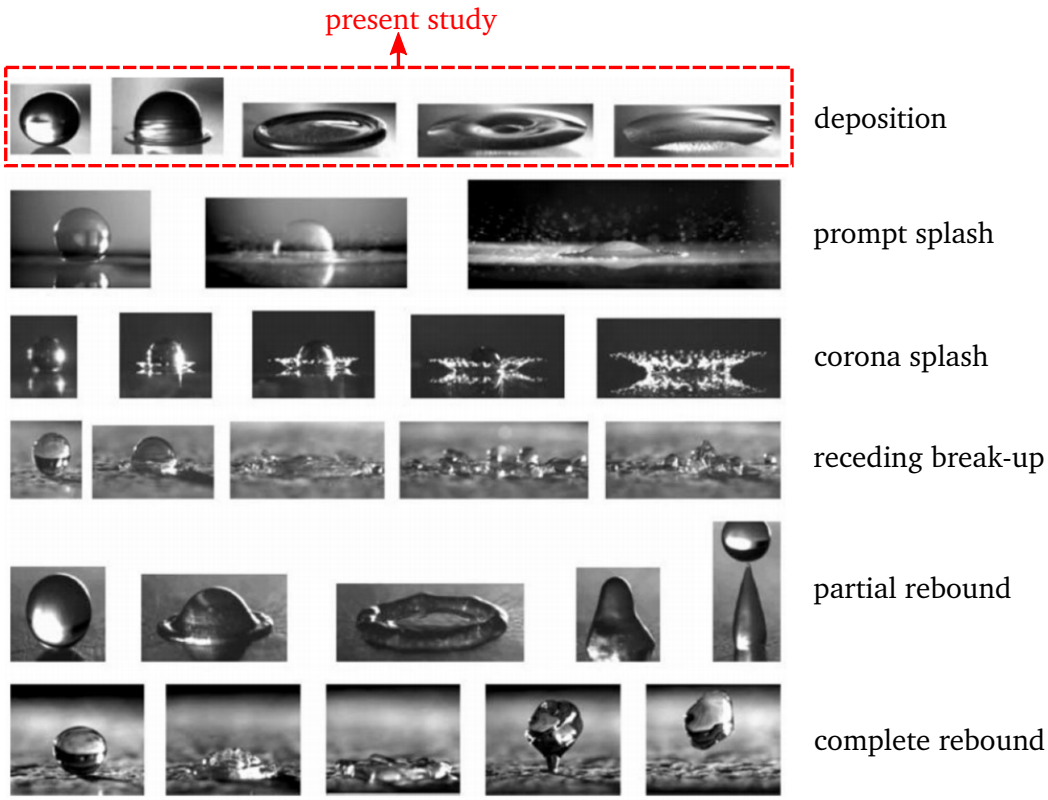

Figure 2.2.: Impingement morphologies over a dry wall. Image courtesy: Yarin [11] and originally published in [10]. The outcome relevant for the present thesis is indicated by a red-dashed box.

If the inertia of the drop is far below the viscous effects, i.e., low Re numbers, the drop deposition is observed. This regime is accompanied by no instabilities and no secondary drop during the entire impingement process. The drop impingement event during this regime can be divided into three subsequent phases: i) the drop spreading phase, ii) the drop receding phase, and iii) the sessile drop phase. In the drop spreading phase, where liquid motion is dominated by inertia forces, the contact line moves radially outwards. In this phase, a rim is formed near the contact line enclosing a thin liquid film near the center of the drop, called the lamella. This process ends

as soon as the contact line reaches its maximum due to the dissipation of kinetic energy. In the receding phase, the contact line starts to shrink. The surface tension is the driving force in this phase, which tends to minimize the surface area of the liquid. Since the kinetic energy increases, the contact line radius might reach a smaller value than that corresponding to the equilibrium form. The contact line moves again outward, and this oscillation phenomenon might be repeated until the drop reaches the equilibrium state, which corresponds to the sessile drop phase.

However, if the receding velocity is fast enough, the rebound of the liquid drop can be observed. In the case of a partial rebound, the initial drop is divided into a large secondary drop leaving the surface, and a liquid residual sitting over the surface. If the surface is superhydrophobic, i.e., the receding contact angle is large, the liquid drop leaves the surface completely. This phenomenon is referred to as complete rebound [10]. If the dynamic contact angle at the end of the spreading phase is very small (close to zero), the receding contact line will lead to the formation of several small secondary liquid drops on the surface, resulting in receding break-up.

Splashing occurs if the inertia of the drop dominates the viscous and capillary forces. In this regime, small secondary drops are generated near the contact line and during the spreading phase. Two types of splashes have already been reported; i) prompt splash and ii) corona splash. The prompt splash is observed only for rough surfaces and is characterized by the generation of the secondary drops at the beginning of the spreading phase; when the lamella has a high radial velocity. The corona splash is observed at a later stage of the impact process, where a crown is formed away from the solid surface, which then breaks up into small drops. Many studies proposed a characteristic K number as an appropriate measure for identifying the transition from the deposition to the splashing regime. The K number is defined as

$$K = We^{1.2} Ca^{-0.4} = We\ Oh^{-0.4} = We^{0.8} Re^{0.4}\,. \tag{2.12}$$

The probability of splashing increases with the value of K. The typical threshold is $K_{\text{splash}} = 657$ [12], but it is strongly influenced by surface roughness [10]. This value corresponds to the impact velocity of $u_0 \approx 0.6$ m s^{-1} for the millimeter-sized FC-72 drops used as the working fluid in this study. The experiments of the present study are conducted in the drop deposition regime, i.e., the impact velocities are always kept below 0.6 m s^{-1}.

However, the characteristic K number is applicable only for a narrow range of drop impact parameters. Recent experimental observations of Roisman et al. [13] suggested the following correlations for the boundary between drop deposition and corona splash:

$$Ca = 0.067 + 0.60\, Oh^{0.35}\,, \quad \text{for} \quad Re < 450\,, \tag{2.13}$$

$$Oh = 0.0044\,, \quad \text{for} \quad Re > 450\,. \tag{2.14}$$

The impact parameters set in present study lead to moderate Re ($1070 < Re < 2500$) and We ($20 < We < 66$) numbers. The Oh number is less than 0.0044 and, according to equation 2.14, leads to the drop deposition regime.

Non-isothermal drop impact

In non-isothermal drop impact, besides the impact parameters and the substrate properties, wall temperature plays a crucial role influencing both impact dynamics and heat transfer performance. Figure 2.3 shows the evaporation time and classification of the impingement outcomes with respect to the thermal boundary conditions. In general, six distinct heat transfer regimes, namely a) subcooled deposition, b) superheated deposition, c) nucleate boiling, d) transition boiling, e) thermal atomization, and f) film boiling can be identified depending on the wall temperature.

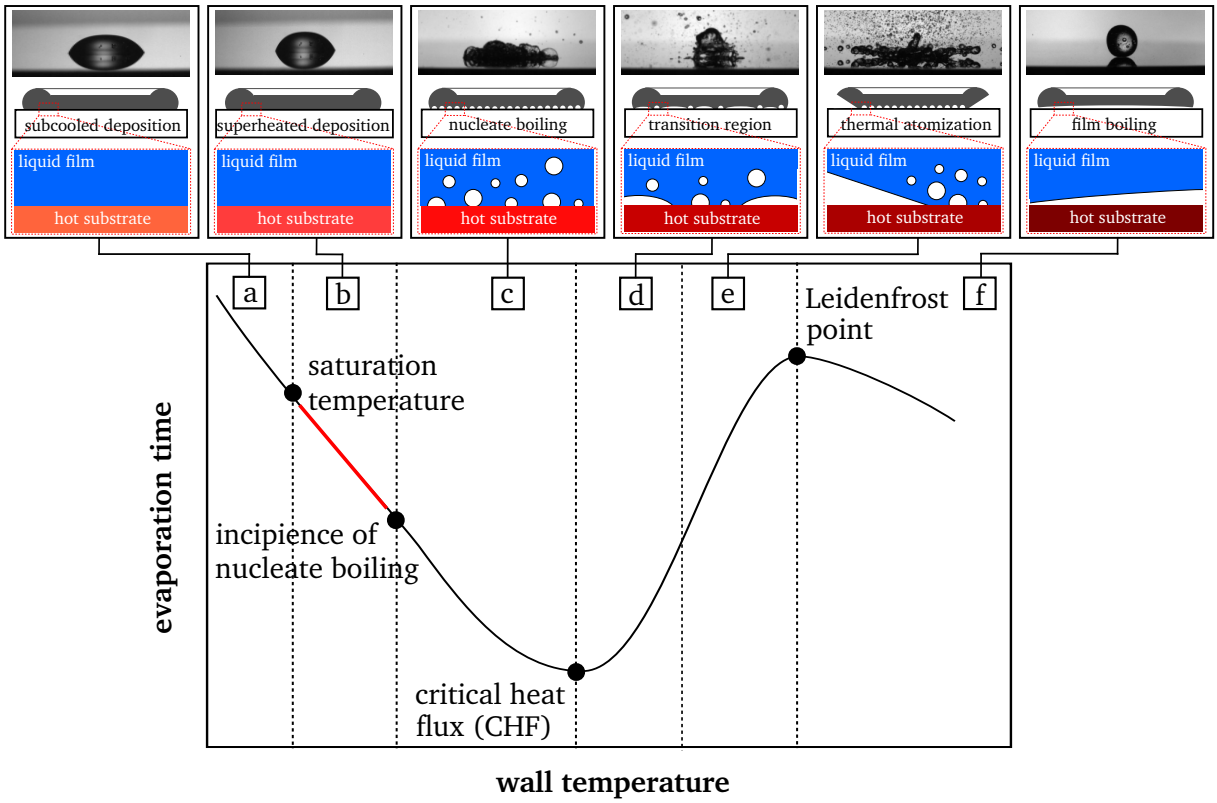

Figure 2.3.: Heat transfer regimes associated with a drop impinging a hot wall: (a) subcooled deposition, (b) superheated deposition, (c) nucleate boiling, (d) transition boiling, (e) thermal atomization, and (f) film boiling (B/W images are reprinted from [14]). The corresponding regime relevant for this thesis is indicated by the red line.

For a wall temperature below the liquid saturation temperature, the drop evaporation is driven by the diffusion of the vapor through the surrounding atmospheric air. In this regime, which is referred to as subcooled deposition (a), the drop evaporation time takes long due to the slow evaporation process caused by low wall temperature.

Superheated deposition (b) refers to the drop impinging onto a surface, in which the temperature is above the saturation temperature and is below the onset of boiling. Within the superheated deposition regime, the drop disappears faster due to intense evaporation. In this regime, the evaporation is determined not only by the vapor diffusion through the surrounding atmosphere but also by the heat transfer from the surface towards the drop.

If the surface temperature further increases, an array of growing bubbles nucleates on the substrate. This regime is referred to as nucleate boiling (c), in which the drop evaporates faster

than both aforementioned regimes. In this regime, the drop lifetime decreases with surface temperature, while the number of the created bubbles increases.

The transition regime (d) appears by a further increase of wall temperature and is characterized by a high density of bubbles coalescing before collapsing. The coalescence of the bubbles and formation of larger vapor regions partially separating the liquid from the wall becomes vigorous with the increase of surface temperature. This phenomenon increases the drop lifetime within the transition regime.

Recent observations unveiled a new regime called thermal atomization (e). The surface temperature in this regime is close to/and smaller than Leidenfrost temperature. If the Re number is high enough, the drop impact is accompanied by the generation of a fast vertical spray of fine secondary drops [15, 16].

Within the film boiling regime (f), the surface temperature is above the Leidenfrost temperature, which is defined as the minimum surface temperature. The drop lifetime at this temperature is maximal. Due to the high temperature difference between wall and drop, a film of vapor develops between the wall and liquid, preventing any direct contact between the liquid drop and wall surface. Due to the poor thermal conductivity of the vapor film, the heat transfer towards the drop reduces, and, accordingly, the drop evaporation takes longer within this regime.

In this study, the case of superheated deposition is addressed, i.e., the initial wall surface temperature is above the liquid saturation temperature but below the temperature corresponding to the onset of boiling (see the red curve in Fig. 2.3).

2.2 Review of single and multiple drop impingement

Many studies address the isothermal drop impact, where heat transfer and evaporation are not taken into account. In such a case, the hydrodynamic behavior is governed by the impact parameters (e.g., impact velocity and impact diameter), liquid material properties, surrounding gas pressure, surface morphology, and wettability. As comprehensively described by Rioboo et al. [10], Yarin [17], Marengo et al. [18], Yarin et al. [19], and already mentioned in Section 2.1.1, various regimes such as drop deposition, prompt splash, corona splash, receding breakup, partial rebound, and rebound can occur depending on the Re and We numbers. The maps of drop impact outcomes for different Re and We numbers are depicted in the mentioned studies.

Fukai et al. [20] performed numerical calculations of the isothermal drop impact using the moving mesh approach, while the gas phase was not included in their investigations. They documented the effects of impact velocity, drop diameter, surface tension, and material properties on the fluid dynamics of the deforming drop. The computational framework of Fukai et al. concerning the isothermal drop impact formed the basis of the work of Zhao et al. [21], who included the heat transfer term in their numerical calculations and studied the non-isothermal drop impact in detail. They determined the temperature fields developing in both the liquid drop and the substrate during the impact. They also found that the convection effects on the temperature field development are important. These effects lead to radial temperature variation during the spreading, especially in high impact velocities.

Wall temperature plays a significant role in the non-isothermal drop impingement, resulting in six distinct regimes explained in detail in Section 2.1.1. The following section addresses an overview of the former studies on single and multiple drop impact, whereby special attention is paid to the superheated deposition regime, which is the main focus of this thesis.

a) Subcooled deposition

In this regime, the wall temperature is below liquid saturation temperature, which results in a slow drop evaporation, and, accordingly, large drop lifetime. Most of the investigations in this regime are limited to the sessile drop evaporation. Erbil [22] published an overview of the theoretical and experimental investigations carried out in this regime.

b) Superheated deposition

This regime refers to the drop impinging on a surface whose temperature is larger than liquid saturation temperature and below the onset of boiling. In this regime, the physical mechanisms of drop impact are almost similar to drop impact under subcooled deposition regime and even isothermal conditions. Yarin [17], Marengo et al. [18], Roisman et al. [13], Josserand and Thoroddsen [23], and Yarin et al. [19] comprehensively studied this regime. This regime is accompanied by higher heat flow to the drop compared with the subcooled deposition regime, since the contribution of the evaporation in the overall heat transfer is higher. Another reason for higher heat flow in the superheated deposition regime compared with the subcooled deposition regime is higher sensible heat due to higher wall superheat.

Experimental studies [24] and numerical simulations [2, 24, 25] reveal three subsequent phases for the drop impingement event in superheated deposition regime on impermeable surfaces: i) the drop spreading phase where the contact line moves radially outward due to inertia forces, ii) the drop receding phase where the contact line starts to contract due to the surface tension, and iii) the sessile drop evaporation phase. During all mentioned phases, heat is transferred by conduction, convection, and partial evaporation; however, the contribution of each heat transfer mechanism differs during various phases.

Lee et al. [26] observed in their experiments that the maximum heat flow occurs during the spreading phase. This maximum is attributed to the high heat transfer rate immediately after the contact between a cold liquid and a hot substrate.

Evaporation is the primary heat transfer mechanism during the receding and sessile drop evaporation phases. A significant fraction of evaporation occurs in the proximity of the three-phase contact line of the drop at which solid, liquid, and vapor phases meet each other. It is due to the significant reduction in temperature in the proximity of the three-phase contact line. This has been observed by Sodtke et al. [27], who measured the local temperature distribution close to the solid–fluid interface for sessile drops evaporating in a saturated vapor atmosphere.

The high-temperature gradient in the proximity of the three-phase contact line is a universal phenomenon. This phenomenon was observed by Ibrahem et al. [28], Höhmann and Stephan [29], and Fischer [30], who performed single meniscus evaporation experiments. A temperature

minimum close to the three-phase contact line has been observed during pool boiling [31–34], as well.

Marchuk et al. [35] and Cheverda et al. [36] measured local temperature distribution at the surface of a metal foil heater under evaporating sessile water drops using an infrared camera and derived the heat flux field by solving the Cauchy problem for the heat conduction equation [37]. Their results reveal that the maximum heat flux is achieved in the three-phase contact line region and exceeds the average heat flux density from the entire foil surface by a factor of 5—7. Herbert et al. [24] and Batzdorf [2] developed a numerical model for heat transfer and evaporation during single drop impact. They reported that during the sessile drop evaporation phase, the heat transferred in the proximity of the three-phase contact line constitutes a considerable fraction of the total heat transfer (almost 50 %). Furthermore, they numerically studied the influence of relevant dimensionless numbers on hydrodynamics and heat transfer during single drop impingement onto a heated wall [2, 25]. Numerical and experimental works by Raj et al. [38] revealed that the apparent contact angle and the local heat flux in the proximity of the three-phase contact line increase at higher wall superheats. They observed that high wall supeheats increase the vapor diffusion, which in turn increase the evaporation rate leading to higher contact angle. Liang et al. [39] showed experimentally that evaporation rate and average heat flux increase linearly with increasing wall temperature.

(c) Nucleate boiling

The nucleate boiling regime spans the region between the onset of boiling, which occurs at a wall temperature slightly above liquid saturation temperature, and the critical heat flux (CHF) point, which corresponds to the shortest drop lifetime as shown earlier in Fig. 2.3. This regime is characterized by the nucleation of growing bubbles on the substrate entrapped between solid and liquid. Effects of parameters such as the drop volume, the wall material and the thickness [40], and the surface tension [41] on nucleate boiling were studied earlier. The former study revealed that the evaporation of drops at their boiling depends significantly on the thermal inertia of material, wall thickness, and state of the heated wall surface. The latter study showed a faster boiling process in case of liquid drops with smaller surface tension and low latent heat of evaporation. Besides, Itaru and Kunihide [42], Chandra and Avedisian [43], Tartarini et al. [44], Abu-Zaid [45], Buchmüller [46], Breitenbach et al. [47] performed numerical and experimental studies for better understanding of this regime.

(d) Transition regime

Transition boiling bridges the region between the CHF and Leidenfrost points. There are limited studies addressing this regime since determining the accurate CHF and Leidenfrost points is challenging. Akhtar et al. [48] derived a correlation for maximum spreading diameter of the drop for specific wall temperatures and We numbers. Nikolopoulos et al. [49] observed a circular vortex ring of air inside the drop in their numerical investigations. They also found that the bubble size increases with increasing wall temperature.

(e) Thermal atomization

During the thermal atomization regime, the surface temperature is close to (and smaller than) Leidenfrost temperature. In this regime, the Re number is high enough, so that drop impact is accompanied by the generation of a fast vertical spray of fine secondary drops. As observed in [15, 16], the central part of the drop lamella is in contact with the solid surface. However, the peripheral part of the lamella levitates in vapor near the contact line and remote from the solid surface.

(f) Film boiling

Film boiling of a liquid drop impinging on a hot surface is termed as the Leidenfrost phenomenon. In 1756, J.G. Leidenfrost published his pioneering article on this topic [50]. He observed a very thin vapor layer between the drop and the wall in extremely high wall temperatures [51]. Bernardin and Mudawar [52] provided a comprehensive review on Leidenfrost temperature and concluded that the surface roughness has a strong effect on Leidenfrost temperature.

Testa and Nicotra [53] and Celestini et al. [54] showed experimentally that the increase in Leidenfrost temperature follows the same trend as saturation temperature under vacuum conditions, i.e., the Leidenfrost temperature decreases with decreasing pressure. Chatzikyriakou et al. [55] and Schmidt et al. [56] performed experiments for single drop impingement in this regime. Both utilized thermography techniques to record the temperature field at the solid–fluid interface; and thereafter, to derive the local heat flux. Breitenbach et al. [57] developed a model to predict the heat transfer during drop impingement in this regime.

Besides wall temperature, additional parameters such as impact parameters, surrounding gas composition and its pressure, surface morphology, and substrate properties influence both impact dynamics and heat transfer performance. The numerical and experimental studies of Pasandideh-Fard et al. [58] indicated that increasing the impact velocity enhances the spatially averaged heat flux from the wall at the end of the spreading phase by only a nominal amount. This is attributed to the increase of liquid–solid contact area due to the larger kinetic energy. Guo et al. [59] showed numerically that the evaporation starts earlier at higher impact velocities. Liang et al. [39] showed experimentally that the impact velocity has only a minor effect on the drop evaporation during the whole evaporation process.

The composition of the surrounding gas is another important parameter influencing hydrodynamics and heat transport mechanisms, particularly during the receding and sessile drop evaporation phases. Numerous investigations of drop evaporation were performed in the air atmosphere [35, 36, 60]. In this case, the drop evaporation is driven by the diffusion of vapor through the non-condensable gases. However, the thermal resistance of the liquid layer is the major limiting factor during the drop evaporation process under a pure vapor atmosphere, causing different evaporation behavior, and, accordingly, apparent contact angle. Cioulachtjian et al. [61] experimentally studied the influence of the surrounding gas on the sessile drop evaporation. They compared the behavior of water drop evaporating in moist air with saturated vapor conditions. They measured a larger apparent contact angle and faster evaporation rate of the drop evaporating under pure saturated vapor conditions.

The ambient gas pressure also affects the hydrodynamics and heat transport during the drop impact [62, 63]. Mitchell et al. [64] experimentally investigated the hydrodynamics of drop impact on an isothermal surface at reduced ambient pressure. They concluded that the splashing could be suppressed by sufficiently lowering the surrounding gas pressure. The same effect has also been observed by Xu et al. [62].

Hsieh et al. [65] modeled drop vaporization at near-critical conditions. They examined a significant influence of ambient pressure on the drop vaporization mechanism, especially near the critical state. They figured out that the drop evaporation rate increases progressively with pressure. This is attributed to the low latent heat of vaporization at higher pressures. This behavior was also observed in [66, 67]. However, a large evaporation rate at elevated pressures does not necessarily mean that the heat flux enhances at elevated pressures during the drop impact while the impact parameters stay constant. The meniscus evaporation experiments at elevated pressures performed by Fischer [30] revealed an extreme decline in heat flux in the proximity of the three-phase contact line from which a significant fraction of the total heat is transferred.

Schlawitschek [68] numerically investigated the non-isothermal drop impact on superheated surfaces at various ambient pressures. She has also examined the strong influence of the ambient pressure on the apparent contact angle and the heat being transferred in the three-phase contact line. She also developed correlations for the maximum spreading ratio, spreading duration, and energy transmitted.

Besides the aforementioned parameters, substrate properties influence the drop dynamics and heat transport during the drop impact. Most boiling and drop evaporation studies [28, 69–71] have employed heating foils exhibiting substantially lower thermal inertia in comparison to the novel IR transparent heaters used in [24, 30]. The temperature differences at the liquid–solid interface are significantly smaller on walls with higher thermal inertia, leading to a different heat transfer behavior. The thermal capacities of IR transparent heaters are much closer to real applications than thin foil heaters.

Surface morphology is another important parameter affecting hydrodynamics and heat transfer during the drop impact. Alizadeh et al. [72] studied the spreading and receding dynamics on the hydrophilic and hydrophobic textured surfaces with different temperatures up to 85 °C. They measured the contact diameters and contact area at the final equilibrium state. Negeed et al. [73] studied the effect of surface roughness and an oxidation layer on the dynamic behaviors of drops impacting on a heated textured surface. They employed stainless Steel with different surface roughness amplitudes. They reported that the spreading period does not change with the surface roughness, but the receding period increases with increasing surface roughness. During the spreading process, the inertia force of drop overcomes the surface roughness, whereas, during the receding process, the surface roughness interrupts the shrinkage of drops.

A porous surface can enhance the cooling rate during drop impact cooling [74–79]. One method to generate porous surfaces is the coating of the substrate with a layer of electrospun nanofiber mat. Weickgenannt et al. [75, 76] studied in detail the non-isothermal water drop impact on an electrospun polymer nanofiber mat deposited on a heated stainless–steel foil. Their measurements were conducted in ambient air. The temperature distribution at the back side

of the foil was measured by an IR camera. They found that the presence of the nanofiber mat prevents the receding motion of drops after their complete spreading. This promotes the moisture spreading inside the mat over a large area of the heater, which significantly enhances the heat removal. Avedisian and Koplik [80] showed that surface porosity increases the Leidenfrost temperature. Besides, Srikar et al. [74] and Weickgenannt et al. [76] reported that the Leidenfrost phenomenon is suppressed if the surface is permeable.

The transport processes during spray cooling are determined not by the impact of a single drop onto a hot wall but rather by a cumulative effect of the impact of multiple drops onto a solid dry wall or a liquid film. However, the hydrodynamics and heat transfer during the impact of multiple drops have not yet been sufficiently studied. This is because of the additional complexity involved in the physics of multiple drops compared with that of a single drop. This complexity arises due to the interaction between the individual drops on the hot wall determined by the interaction mode (for example, a simultaneous impact of several drops onto different locations or a successive impact of drops onto the same location) and other governing parameters (such as the distance between the impact locations and the drop impact frequency).

Liang et al. numerically simulated the fluid mechanics during the successive and simultaneous impact of multiple drops onto a thin liquid film [9, 81–83]. Their results showed that the impact of multiple drops could affect the splashing threshold. Furthermore, the impact of multiple successive drops led to a non-uniform distribution of the local heat flux.

The hydrodynamic mechanisms of isothermal drop impact onto a sessile drop were numerically and experimentally investigated by Fujimoto et al. [84–87]. They studied the hydrodynamics of the liquid during the collision of a water drop with a hemispherical static water drop on a solid surface. They realized that the liquid around the bottom of the incoming drop swells after the collision and moves radially outward with time. Simultaneously, the liquid height near the center of the liquid decreases. They validated their findings experimentally using a flash photographic method.

Minamikawa et al. [88] performed numerical and experimental investigations of the deformation mechanisms of two drops impinging successively onto a hot solid surface in the film boiling regime. They reported that the liquid deforms into a crown shape during successive impacts. The size of the crown was found to be dependent on the spacing between the two drops before the impact. The authors also determined that the time evolution of the drop shape depends on the surface temperature.

Guggilla et al. [70, 71] numerically and experimentally studied the spreading and heat transfer dynamics of two water drops impinging successively onto a heated surface. In the experimental study, the two drops impacted onto the surface with a time interval of approximately 3 s. It was observed that the spreading ratio (the ratio between the diameter of the wetted region and the initial drop diameter) is higher for drop-on-drop impingement than for the impact of the first drop. The maximum heat flow in the case of drop-on-drop impingement was measured to be lower than that in the case of single impingement. The experiments were conducted under the air atmosphere, and a thin heated metal foil was used as a heating substrate.

Roisman et al. [89] studied the hydrodynamics of two drops impinging simultaneously onto a smooth, dry, and solid substrate both experimentally and theoretically. They observed that the interaction of the flow in their respective lamellae leads to the appearance of a symmetric central uprising sheet. However, the untouched regions of the rim proceeded to expand and were not influenced by the interaction. The hydrodynamics of simultaneous impingement of two drops while having different impact velocities onto a smooth, dry and solid substrate was numerically studied by Raman et al. [90]. They investigated the effect of the tangential component of impact velocity of one of the drops. They concluded that the untouched regions of the rim of the drop having the higher impact velocity expands and is not influenced by interaction with the second drop.

Batzdorf et al. [91] modeled the heat transport mechanisms during the simultaneous impact of two equal drops onto a dry solid wall in the drop deposition regime. Their model predicted a decrease in heat flow due to the interaction and coalescence of drops over the solid substrate. Additionally, the maximum heat flow increased with increasing the distance between the impact locations.

A detailed overview of further investigations and modeling approaches can be found in the comprehensive review of Liang and Mudawar [92]. The review paper addresses the main heat transfer regimes. Each of these regimes is discussed in detail in terms of available depictions of drop deformation and/or breakup, proposed heat transfer mechanisms, predictive correlations and models. They concluded that understanding the underlying physics for each heat transfer regime highly depends on the experimental methods researchers have adopted.

2.3 Objectives of this thesis

Numerous applications and industrial processes involve non-isothermal interaction of drops with hot surfaces, e.g., spray cooling, widely used in many technical applications ranging from die forging and hot rolling to electronics. In spray cooling technology, higher heat flux densities are a necessity in order to enhance the performance of the products, reduce cycle times during the production process, and enhance the efficiency of the electronic devices. In recent years, a trend towards miniaturization of electronic, optical, and radiological components poses further challenges in the cooling processes of such hot devices. Therefore, many investigations are devoted to determine efficient approaches to enhance the heat removal during the cooling process, e.g., surface modification.

The tendency of heat removal enhancement during spray cooling requires a profound understanding of the physics involved in the phenomena. The transport processes during spray cooling are determined not only by the impact of a single drop onto a hot wall but rather by a cumulative effect of the impact of multiple drops onto a solid dry wall or a liquid film. However, the progress made over the past years in hydrodynamics and heat transfer during the impact of a single drop single drop, especially multiple drops, is far from complete, and the exact mechanisms are not fully clear. Therefore, high-resolution measurement techniques are required to obtain detailed information concerning the hydrodynamics and heat transport mechanisms during single and multiple drop impact onto a heated surface. It also enables thorough investigations into the

effect of influencing parameters on non-isothermal drop impact to optimize the spray parameters for heat transfer enhancement during the spray cooling processes.

The present thesis has the objectives to enhance the understanding of non-isothermal drop–wall interactions in a pure vapor atmosphere and at a moderate wall surface temperature (above the saturation temperature but below the temperature corresponding to the onset of boiling). This study uses high-resolution temperature measurement techniques to comprehensively understand hydrodynamics and heat transport mechanisms during non-isothermal drop impact. To the authors' knowledge, up to now, no attempt has been made to investigate the influence of wall superheat, impact parameters (impact diameter and impact velocity), system pressure, and surface porosity on hydrodynamics and heat transfer during the single drop impingement under saturated vapor atmosphere. Besides experimental investigations into the influence of the parameters, as mentioned earlier, a detailed study of hydrodynamics and transient heat flux distribution during the vertical and horizontal coalescence of two drops is another objective of this thesis.

The experimental results, together with a predictive model, can contribute to better insights into the mechanisms of spray cooling and the improvement of spray systems in the future.

3 Experimental Apparatus, Measurement Methods and Data Reduction

This chapter addresses first a survey concerning available drop generation methods (Section 3.1) and high-resolution temperature measurement techniques and (Section 3.2). Subsequently, the employed experimental apparatuses and relevant components required for the measurements is outlined. Afterwards, the experimental procedure followed by measurement methods and data reduction are presented.

3.1 Survey of drop generation methods

The review of experimental works conducted on drop impingement in the previous section shows that, in general, various methods can be utilized to generate liquid drops. The applied method in this work should fulfill several requirements:

1. Generation of reproducible drops of the employed working fluid (FC-72, see Section 3).
2. Possibility to control the frequency of drop generation
3. Possibility to generate drops under high pressure
4. Convenient generation of two successive and/or simultaneous drops

In order to identify the most appropriate method of drop generation for this work, the following methods are taken into account and possibly tested.

Drop generation with a subcooled needle

This method was used by Herbert et al. [93]. In this method, a needle is placed inside a cell and is slightly subcooled against the saturation temperature of the working fluid. Within this method, reproducible drops of FC-72 can be formed at the needle tip by condensation of the surrounding vapor. However, controlling the frequency of the drop generation, especially at high system pressures, requires a sophisticated cooling system. Besides, the generation of two simultaneous drops is questionable with this method.

Drop generation with a monodisperse piezoelectric drop generator

Another possible method for drop generation is using monodisperse piezoelectric drop generators. Breitenbach [14] used a piezoelectric drop generator[1] to generate reproducible drops. The frequency of the drop generation can be controlled well with this device, and also two similar devices can be used in parallel to generate simultaneous drops. However, the generation of reproducible FC-72 drops with frequencies less than 1000 Hz is impossible when tested. This frequency is far beyond the required frequency for the single drop impact investigations.

[1] FMP drop generator from FMP technology GmbH (https://fmp-technology.com)

Additionally, the generation of the drops under high system pressures is questionable with this method.

Drop generation with a micro pump

A micro pump can be used to generate drops with a wide range of frequencies. The main drawback of this method is the incompatibility of this system with low viscous liquids. As tested, with the micro pump[2], the process of drop generation is not quite reproducible, and the frequency of the drop generation is not stable. This makes the investigations on multiple drop impact challenging. Moreover, the generation of the drops under high system pressures is not easy as well.

Drop generation with a syringe pump

One popular approach of generating single drops or drop chains with moderate frequencies among researchers is using a syringe pump. The standard syringe pumps available in the market cannot tolerate high pressures. But the mid pressure syringe pump manufactured by CETONI GmbH[3] can stand up to 100 bar. Moreover, the units can be connected in parallel to generate two simultaneous drops.

Following the survey of available drop generation methods given above, a mid pressure syringe pump has been chosen, as it is the only available method for the generation of reproducible FC-72 drops in single and multiple modes. In combination with a high-pressure test cell described in Section 3.5, the drop impingement investigations under high system pressures can be feasible with this syringe pump.

3.2 Survey of high-resolution temperature measurement techniques

In general, the temperature distribution at the wall can be measured with several techniques, namely laser-induced fluorescence and laser-induced phosphorescence [94–96], liquid crystal thermography [29, 97], and infrared thermography [28, 30, 55, 71]. The applied measurement technique for this work should fulfill the following requirements:

1. High spatial and temporal resolution
2. Fast response time
3. High measurement sensitivity
4. No addition of extra heat
5. No mechanical disruption of the heater surface
6. No change in properties of the working fluid

In Table 3.1, the advantages and disadvantages of each measurement technique are listed.

[2] mzr-2505 micro pump from HNP Mikrosysteme GmbH (https://www.hnp-mikrosysteme.de)
[3] https://www.cetoni.com

Table 3.1.: The advantages and disadvantages of various wall surface temperature measurement techniques

measurement technique	advantages	disadvantages
Laser-induced fluorescence (LIF) and phosphorescence (LIP)	+ High spatial resolution less than 1 μm + High temporal resolution up to 1000 Hz + Relatively good measurement sensitivity down to 0.6 K	- Introduction of extra heat from the laser to the heater - Agglomeration of the fluorescence/ phosphorescence dye or particles in contact line due to high evaporation rate
Liquid crystal thermography (LCT)	+ High spatial resolution down to 1 μm/pixel	- Unrepeatable measurements due to aging and hysteresis of the uncapsuled TLCs - Large response time due to large thermal inertia
IR thermography	+ High spatial resolution down to 25 μm/pixel + High framerates of up to several thousands Hz + High measurement sensitivity down to 0.1 K	- Relatively complex calibration process

Following information regarding high-resolution temperature measurement techniques given in Table 3.1, IR thermography has been chosen for this work.

3.3 Basic concept

With regard to the objective of this thesis presented in Section 2.3, a drop impact experimental setup is designed and constructed. Figure 3.1 demonstrates the core part of the setup. A liquid drop is generated at the tip of a needle embedded inside an enclosed temperature-controlled test cell filled with a degassed single species fluid. The drops are generated by pumping the same liquid from a reservoir into the cell with a syringe pump[4]. The pressure inside the cell is determined by the fluid temperature. Hot liquid from a high temperature thermostat passes through the channels drilled in the wall of the cell in order to establish and control the fluid temperature and consequently the system pressure.

Since the influence of the pressure is planned to be investigated, all components must resist the system pressure and temperature, preferably up to the critical pressure and temperature of the experiment fluid. Two robust sapphire windows are integrated on the sides of the cell to enable drop visualization.

Refrigerant FC-72 (perfluorohexane) is used as the working fluid. Having relatively low critical temperature ($T_{crit} = 452$ K) and critical pressure ($P_{crit} = 18.3$ bar) make this liquid suitable for

[4] neMESYS Mid Pressure syringe pump from CETONI GmbH

high pressure investigations. Apart from being thermally and chemically stable, non-flammable and non-toxic, this liquid leaves essentially no residue upon evaporation. Furthermore, the properties for this liquid are known (see Annex A.1).

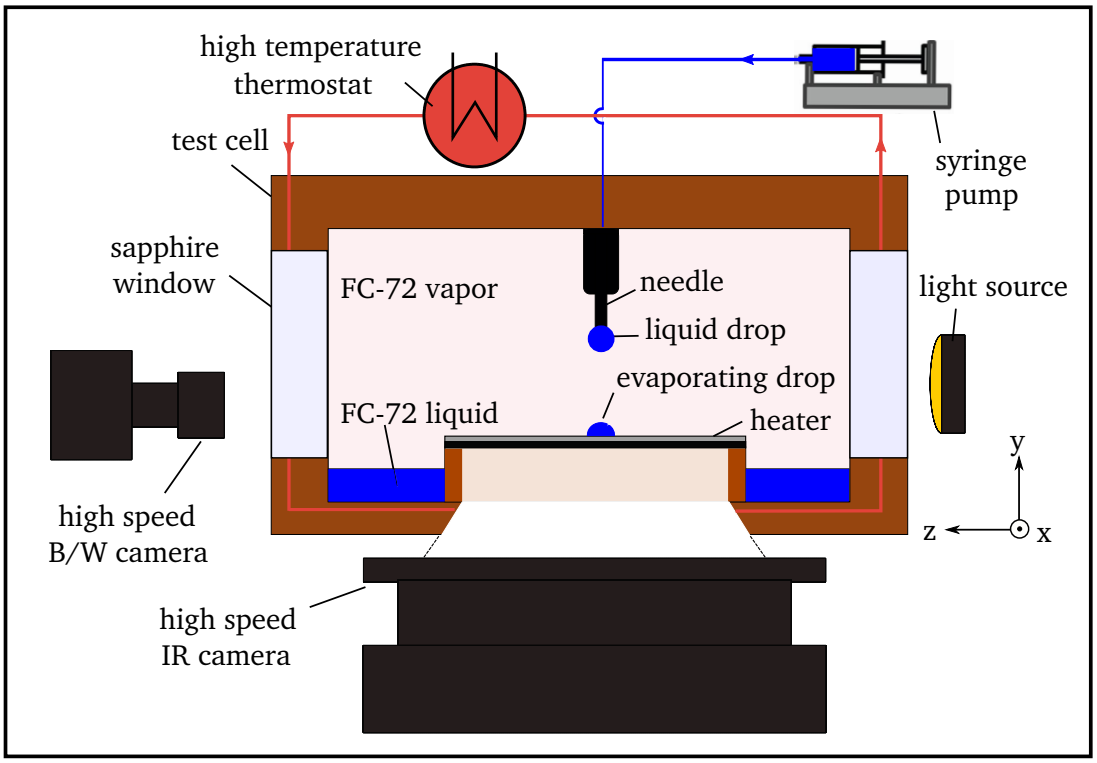

Figure 3.1.: Schematics of experimental concept

3.4 Heater design

Heating foils as the hot substrates have been used in many boiling and drop evaporation studies so far [31, 70, 71]. The heating foil requires a complicated pressure equalization system to avoid the deformation and rupture of the foil at high pressures. Instead of a heating foil, a novel pressure-resistant heater in which two metallic layers sputtered on top of an IR transparent substrate is employed. In the present study, besides being mechanically robust, this heater design allows the measurement of wall temperature by IR thermography considerably closer to the fluid–solid interface (approx. 800 nm) than with heating foils. Additionally, the thermal capacity of the sputtered heater is closer to the technical applications in comparison with the heating foils.

An exploded view of the heater design and heater flange are shown in Fig. 3.2. The heater is comprised of a 4 mm thick IR transparent CaF_2 substrate, coated with a 400 nm CrN layer and an additional layer of 400 nm pure Cr on top. The thermal diffusivity of CaF_2 substrate is $\alpha_{CaF} = 3.575 \cdot 10^{-6}$ m^2 s^{-1} [98], which is in the same range as that of the stainless steel alloys (e.g. $\alpha_{1.4301,20^\circ C} = 4.040 \cdot 10^{-6}$ m^2 s^{-1} [99]). Thus, the thermal properties of the heater, such as thermal capacity and thermal diffusivity, are very close to the heated walls commonly used in technical applications. The thickness of CaF_2 is chosen to be 4 mm to ensure its stability at high pressures up to the critical pressure of the working fluid. The properties of the CaF_2 substrate are given in Annex A.1.

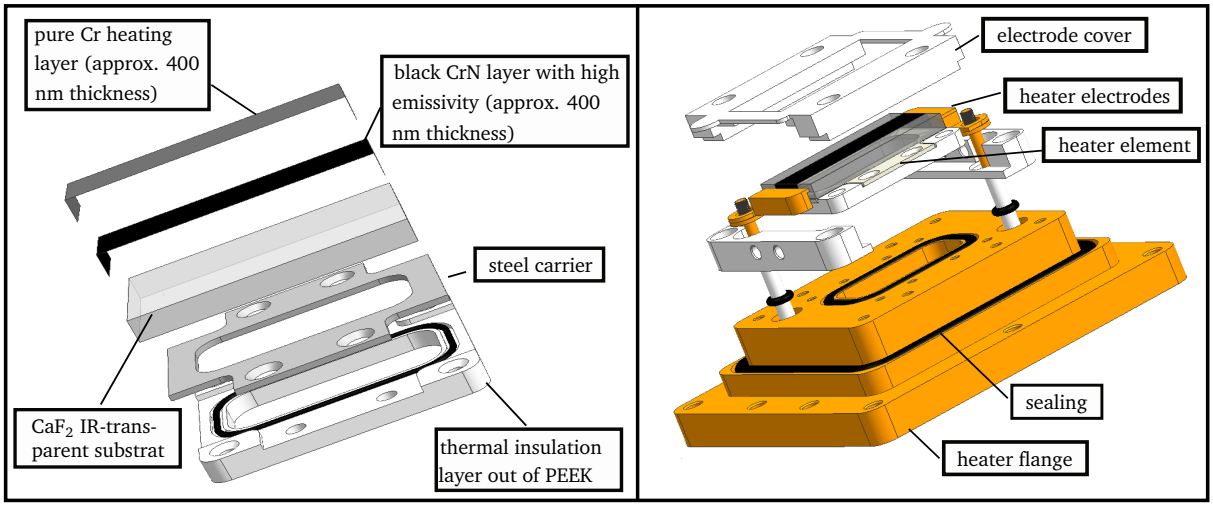

Figure 3.2.: Exploded view of the heater design (left) and heater flange assembly (right).

The black CrN layer with a high emissivity is applied to optimize the temperature measurements with the IR camera. The pure Cr layer acts as a Joule heating layer. The Cr and CrN layers have been deposited through Physical Vapor Deposition (PVD) processe [100]. The thickness of 400 nm for each layer facilitates the temperature measurements extremely close to the fluid–solid interface. Since both Cr and CrN layers are very thin, the energy storage and thermal resistance in these layers are negligible. The thickness, and, accordingly, the resistance of the Cr layer sputtered on the heater substrate is homogeneous, leading to a uniform heat flux distribution inside the heater. More details regarding the heat flux distribution are given in [30]. The uniformity of the heat flux on the heater surface is also confirmed by the observed homogeneous temperature and heat flux distributions prior to the drop impact.

The arithmetical mean deviation, maximum valley depth, maximum peak height, and maximum height of the profile for the heater surface are 5, 15, 15, and 30 nm, respectively. Therefore, the heater surface can be considered as a smooth surface. Under isothermal conditions, the static contact angle for FC-72 on the surface is measured to be less than 3°. The sputtering process and surface topography measurement of the heater has been performed at the Staatliche Materialprüfungsanstalt Darmstadt, Fachgebiet und Institut für Werkstoffkunde (MPA-IFW).

The coated substrate is glued[5] onto a 2 mm thick stainless steel carrier plate and then screwed to a 2 mm thick PEEK structure both equipped with optical access to the bottom side of the CrN layer in such a way that the central part of the plate with the area of 495 mm^2 (33x15 mm) is accessible for optical diagnostics. The PEEK structure is used to thermally insulate the heater from the cell body and consequently reduce the thermal losses through the cell body. The heater is clamped with two copper foil electrodes at each of its sides and finally connected to the laboratory power supply[6] controlled by a data acquisition system (DAQ).

The electrical resistance of each heater varies between production batches, although the parameters for the deposition process are always maintained the same. Therefore, the resistance of each heater is measured individually according to the following procedure:

[5] Polytech EP 655-T
[6] Elekto-Automatik EA-PS 3065 – 05 B

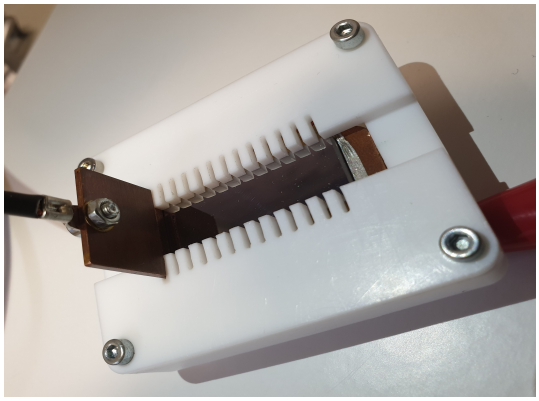

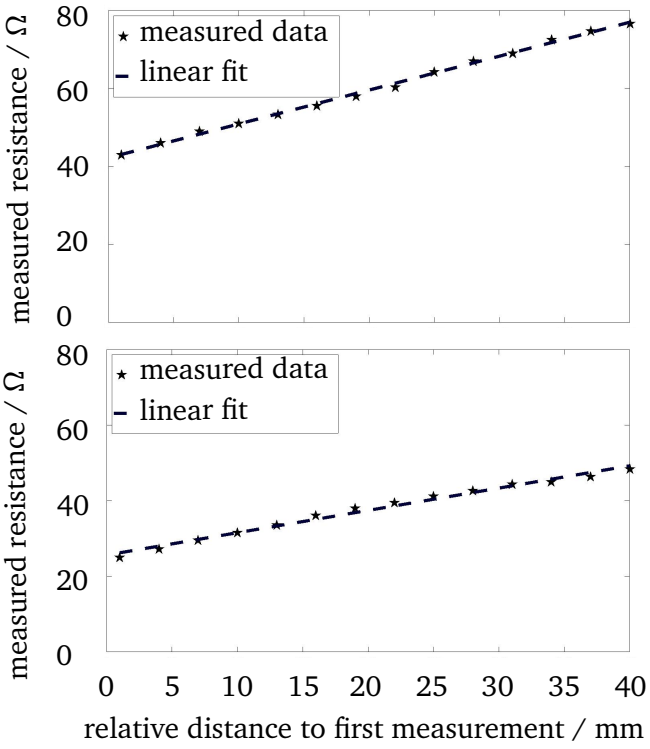

Figure 3.3.: Measurement apparatus for measuring the heater resistance (left); measured heater resistance and linear fit versus distance to first measurement point for two heaters of different production batches (right).

The heater is embedded inside a structure depicted on the left side of Fig. 3.3. The heater is clamped with a copper foil electrode at one side. A second copper foil electrode is placed vertically on the top of the heater, inside the grooves created in 3 mm intervals. The electrical resistance between both electrodes is measured for each position of the foil electrode. The slope of the line fitted to the measured value indicates the heater resistance per length of the heating layer in $\Omega\ \mathrm{m}^{-1}$ (see Fig. 3.3, right). The heater resistance of an individual heater is the product of the slope of the linear fit and the length of the heater. With this method, the contact resistance of the heater electrodes is eliminated, and the resistance of the heating layer only is obtained. The resistance measurement is always performed at the end of drop impact experiments, since the mentioned technique may partially destroy the heater surface.

3.5 Experimental setup

The basic concept introduced in Section 3.3 is realized in a drop impact experimental setup. Figure 3.4 depicts the schematic of the setup. A sealed temperature-controlled test cell is the core component of the setup that allows drop impact investigations under pure vapor atmosphere and at elevated pressures. The test cell is comprised of three compartments; heater flange, main body, and cell cap. Exploded and sectional views of the test cell are provided in Annex A.2.

The heater flange described in Section 3.4 is screwed to the bottom of the cell. Power is supplied to the heating layer through electrical feedthroughs connected to a laboratory power supply controlled by DAQ.

The working fluid is transferred from a transportable reservoir to the cell through a liquid connector integrated into the main body of the cell. The pressure inside the cell is determined by the fluid temperature. A high-temperature thermostat[7] is employed to pass heated silicone oil[8] through the thermalization channels drilled in the main body of the cell to control the fluid temperature, and, accordingly, the system pressure. The main body of the cell is provided with eight symmetrical thermalization channels at the side and two channels at the bottom. Silicone oil enters from both bottom channels in parallel and then is directed to the side channels in series so that the temperature distribution of the fluid becomes approximately homogeneous.

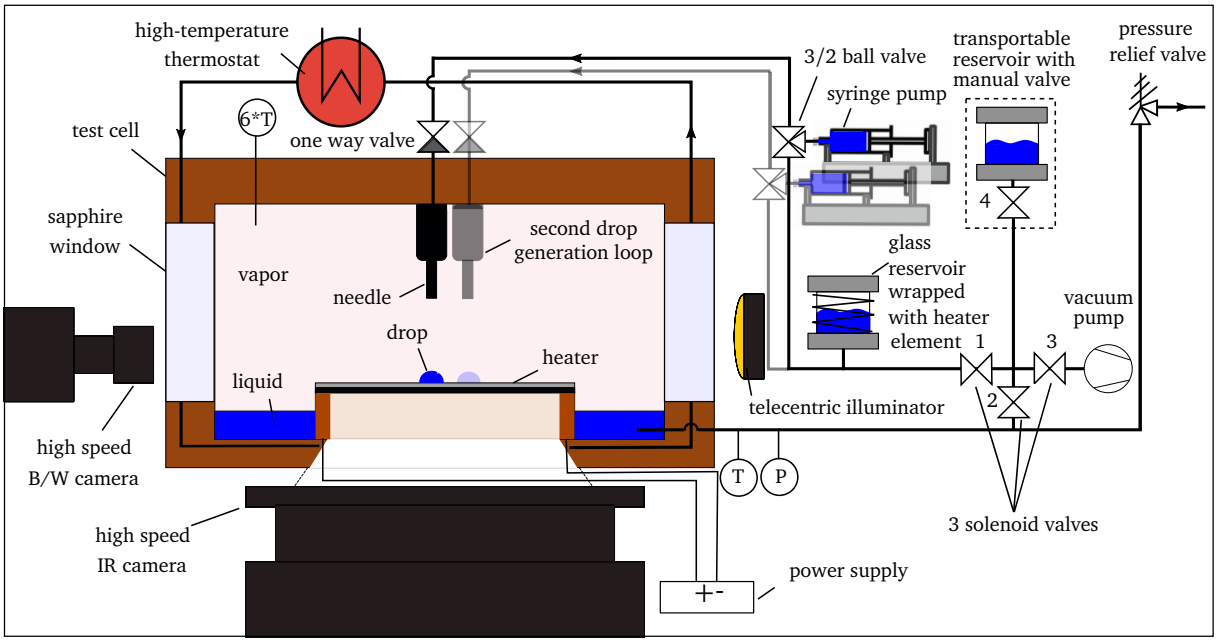

Figure 3.4.: Schematics of experimental setup

Two 10 mm thick sapphire windows are mounted on each side of the cell to provide optical access to the drop; one side for optical access of the high-speed black and white (B/W) camera and the other for the light source[9]. Since the impact velocity in this study is determined by the drop height and gravitational acceleration, the height of the main body is designed such that it covers the desired drop impact velocities.

The cell cap is equipped with six thermocouple feedthroughs. The thermocouples[10] are connected at different heights and radial directions to measure the liquid and vapor temperatures. A liquid drop is transferred to the cell through the liquid feedthrough inserted at the middle part of the cell cap. The cell cap also contains two feedthroughs for liquid circulation during in situ calibration of the IR camera.

For safety reasons, the setup is equipped with an overpressure relief valve designed to open at 20 bar. It is installed at the pipe connecting the transportable reservoir to the cell. A pressure sensor[11] is connected to this pipe to measure the cell pressure that is read out by the DAQ.

7 Huber ministat 125 with Pilot ONE
8 Huber thermofluid P20.275.50
9 telecentric illuminator from Opto Engineering GmbH
10 Mineral insulated thermocouples, type K, D = 0.5 mm
11 Wika ® Precision Pressure Transmitter Type P—10, 0 — 25 bar, abs.

One of the most challenging requirements for the setup is to generate reproducible drops at high pressures. The variation of one parameter while keeping the others constant is desired within the employed system to perform the parametric study. The parameters are impact velocity, drop size, and drop generation frequency. In addition, the system should be able to generate two similar drops within as short a time difference as possible in order to study simultaneous coalescence of two drops. Following the survey of available drop generation techniques described in Section 3.1, a high-pressure syringe pump is selected, as it is the only method to generate reproducible drops under the desired conditions. The drop generation system comprises of the following compartments:

- a glass reservoir in which the degassed liquid is filled from the transportable reservoir.
- a syringe pump unit that is capable of being connected to another unit in parallel.
- a 5 ml glass syringe.
- a 3/2 ball valve that can connect the syringe pump either to the glass reservoir for filling or to the cell for dispensing purposes.
- a one-way valve to prevent backflow in the system.

The drop diameter with this technique is highly reproducible, since the detachment of the drop is governed by the balance of gravity and surface tension forces. The impact velocity and impact diameter can be varied by using different needle heights and diameters, respectively.

Three solenoid valves are used to connect the system to a vacuum pump and to connect the transportable reservoir to the cell and glass reservoir. The valves are controlled with labVIEW.

Photographs of the experimental setup are provided in Figs. 3.5 and 3.6.

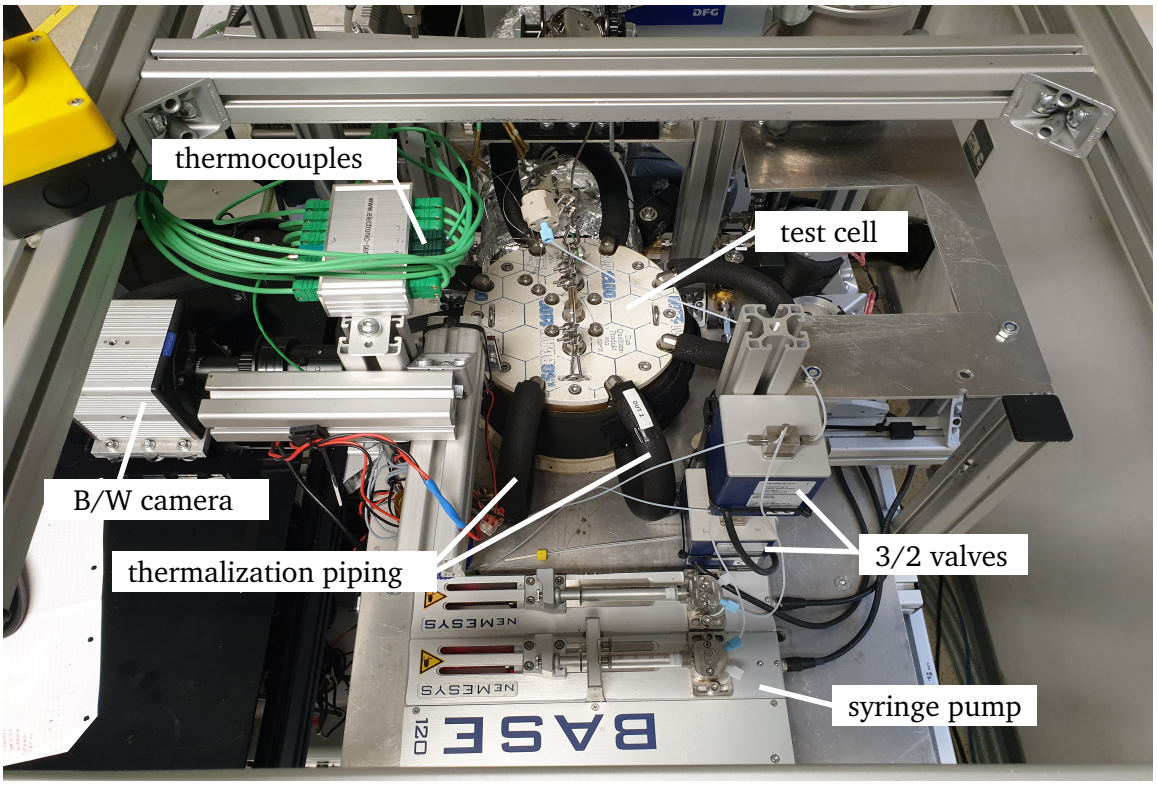

Figure 3.5.: Photograph of the experimental setup core

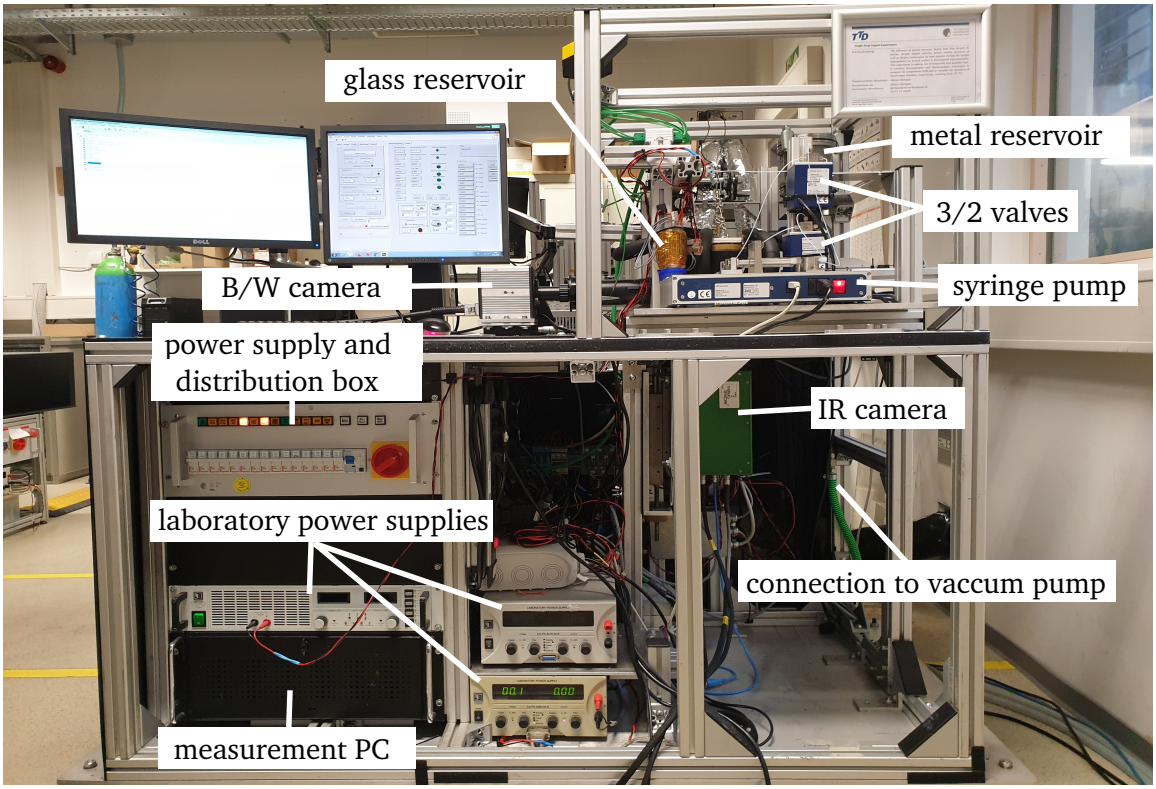

Figure 3.6.: Photograph of the experimental setup

3.6 Experimental procedure and parameters

The main interest in this study is the drop impact investigations under a pure vapor atmosphere. The presence of non-condensable gases alters the local saturation conditions, depending on the local vapor concentration in the gaseous phase. This is not desired in this work. Therefore, the non-condensable gases are extracted from the liquid using a degassing experimental setup [30]. The setup is filled with the working fluid (FC-72), from which the non-condensable gases are separated by continuous evaporation and re-condensation. These processes occur inside an evaporator and condenser vessels connected to hot and cold thermostats, respectively. The non-condensable gases are accumulated at the top part of the condenser and are drawn from the setup by opening a valve connected to a vacuum pump every 10 minutes time intervals repeatedly. The amount of non-condensable gases inside the liquid reduces after each period. After one hour, a reduction of the non-condensable gas content of approximately 90 % is measured, which suggests a very high quality of the applied degassing procedure [30]. To check the quality of the degassed liquid, the results from gas chromatography-mass spectrometry of the degassed and non-degassed liquid are compared (see Annex A.3).

Finally, the degassed liquid is fed into the transportable reservoir, which can be transferred and mounted on the drop impact setup. The whole system is vacuumed prior to each experimental run to ensure a pure saturation atmosphere. This has been accomplished by connecting the whole setup to the vacuum pump and opening all three solenoid valves (Nr. 1, 2, and 3) shown in Fig. 3.4. The air leakage rate of the whole system is $1.5 \cdot 10^{-4}$ mbar l s^{-1} over the time period of 24 hours. This corresponds to the partial pressure rise of non-condensable gases inside the

system of 1 mbar during 2 hours until the cell pressure reaches the lowest measurement pressure (0.94 bar). From this moment on, the leakage rate extremely reduces since the relative pressure is almost zero. This amount of non-condensable gases added to the system is negligible, since the system is refilled before each experimental run.

After the complete evacuation of the setup, the degassed liquid inside the transportable reservoir is fed into the test cell by opening the valves Nr. 2 and 4, shown in Fig. 3.4. The filling process of the cell takes a few seconds until the cell is partially filled with the liquid. It should be noted that the heater must not be immersed in the fluid after the thermalization process. Then valves Nr. 1 and 4 are opened to fill the glass reservoir with the degassed liquid. The cell pressure after the filling process is equivalent to the saturated pressure of FC-72 at the laboratory room temperature, which is about 0.3 bar.

After the filling process, the thermostat is switched on, and its temperature is set to a little higher than the saturated temperature of the desired pressure level. The heated oil is passed from the thermostat to the channels drilled inside the outer shell of the cell body. Since the cell is continuously heated and its volume is constant, the pressure level inside the cell rises. This proceeds until the transferred energy from the thermostat is in equilibrium with the heat loss from the cell to the ambiance. Then the measurements are started as soon as the stationary condition is reached. This is checked through the temperature measurements from the six thermocouples installed at different positions inside the cell.

To generate a drop, the syringe is initially filled with the degassed liquid stored inside the glass reservoir. This is carried out with labVIEW software by pulling back the syringe plunger while the 3/2 ball valve connects the syringe pump to the glass reservoir. It was observed that the syringe is partially filled with FC-72 vapor during the suction process. To inhibit the formation of vapor inside the syringe and speed up the filling process, a heater foil is wrapped around the glass reservoir (see Fig. 3.4). This increases the liquid pressure and temperature inside the glass reservoir locally and leads to faster liquid transportation and prevention of vapor formation inside the syringe.

The liquid enters the cell by pushing the syringe plunger when the 3/2 ball valve connects the syringe pump to the cell. The filling and dispensing processes are extremely slow; therefore, the liquid temperature before entering the cell is about the room temperature. However, the liquid temperature increases when it passes through the heated cell cap until it reaches the needle tip. The transported liquid gradually accumulates at the tip of the needle and forms a fine drop. The drop detaches and falls onto the heater described in Section 3.4 once the gravity force dominates the surface tension force.

Variation of the input heat flux to the heater, and, accordingly, wall superheat has been realized by varying the electrical power of the laboratory power supply controlled by DAQ. The impact velocity and impact diameter have been varied by using different needle heights and diameters, respectively. The pressure inside the cell is varied by setting the thermostat at various temperatures. Alteration of the thermostat temperature leads to various cell pressures. This allows us to investigate the influence of the cell pressure on hydrodynamics and heat transport during drop impingement. In the scope of this work, nanofiber mats with various thicknesses have

been produced with an electrospinning device to investigate the influence of the porous surfaces during drop impingement.

In this work, the investigations are not limited to the single drop impingement. Multiple drops are produced by either variation of the dispensing volume flow rate of the syringe pump leading to the vertical coalescence of drops (successive drop impact) or by mounting second syringe pump unit in parallel with the main unit causing horizontal coalescence of drops (simultaneous drop impact). The flow rate of dispensing volume of each pump is set and controlled in a way that the simultaneous impact occurs. With the employed syringe pump unit, the minimum time difference between drop generation for each individual pump is about 1 ms. Therefore, "simultaneous drop impact " in this work represents the impact of two drops with the time difference of around 1 ms. This small time difference between the impacts does not significantly influence the results, since the horizontal coalescence occurs later than 1 ms after impact.

Table 3.2 represents the parameter space for single and multiple drop impingement investigated in this study. In this table, each row corresponds to one measurement campaign. The first column is the varied parameter during each measurement campaign, and the second is related to the influencing parameter under investigation. The other columns are the corresponding dimensional and dimensionless parameters. The parameter space is set up by all possible combinations of four input heat fluxes, and, accordingly, wall superheats, four impact velocities, four drop sizes, and four reduced pressures during the single drop impact. In this study, the influence of the nanofiber coated surfaces during single drop impact is investigated, as well. Besides, three frequencies and two spacing parameters for vertical and horizontal drop coalescence are chosen. Each experiment set is run at least three times to check the reproducibility.

Table 3.2.: Experimental parameter ranges

parameter	influenced properties	ΔT/K	u_0/ms^{-1}	D_0/mm	P_R/-	Re/-	We/-	Ja/-	Bo/-	Pr/-
input heat flux q_{in}	wall superheat (ΔT)	6.9 ... 17.2	0.44	0.93	0.05	1450	34	0.10 ... 0.22	0.4	9.7
needle height	impact velocity (u_0)	6.3	0.33 ... 0.57	0.93	0.05	1070 ... 1905	20 ... 59	0.08	0.4	9.7
needle gauge	impact diameter (D_0)	6.3	0.44	0.97 ... 1.60	0.05	1520 ... 2500	37 ... 61	0.08	0.4 ... 1.2	9.7
cell temperature	system pressure (p_R)	6.5	0.34	0.94	0.05 ... 0.5	1220 ... 1530	23 ... 53	0.10 ... 2.08	0.4 ... 1.4	7.3 ... 9.7
nanofiber coated surface	surface porosity	1.2 ... 17	0.32 ... 0.58	0.95	0.05	1070 ... 2030	18 ... 66	0.01 ... 0.22	0.4	9.7
drop generation frequency (f)	vertical coalescence	12.4	0.54	1.14	0.05	2160	64	0.16	0.6	9.7
spacing parameter (e)	horizontal coalescence	7.3	0.54	0.93	0.05	1700	49	0.10	0.4	9.7

3.7 Measurement methods and data reduction

This section explains the applied methods to evaluate the drop diameter and impact velocity by post-processing of the B/W images captured with the high-speed camera. Besides, the wall temperature measurements with IR thermography and the procedures of heat flux calculation and contact line radius detection from the IR images are comprehensively described. In addition, the measurement uncertainty is outlined at the end of this section.

3.7.1 High-speed shadowgraphy for evaluation of the drop diameter and impact velocity

To determine the drop diameter and impact velocity, the images captured by the high-speed black and white (B/W) camera are used. The drop appears dark in the B/W images, since the parallel beams emitted from the telecentric illuminator are mainly reflected or refracted when they collide with the liquid drop surface. The drop surroundings are bright inside the B/W images as the light beams can pass well through the vapor. The optical resolution of the high-speed camera is set to $\Delta x_{\mathrm{res,B/W}} = 10.87$ μm/pixel, and its frame rate is set to f= 1000 Hz.

Figure 3.7 presents the implemented steps to process the original images captured from the B/W camera until the drop contour is obtained. To determine the drop contour, the following steps have been carried out:

- The corresponding frames before impact are detected, and each is subtracted from the reference image, inside which the drop is not present.
- Then, the result is binarized according to Otsu's method [101] by which the pixels are subdivided to above (one= white) and below (zero= black) a predefined threshold.
- Any small remaining elements inside the drop due to the light reflection are removed from the image, and finally, the drop contour is obtained.

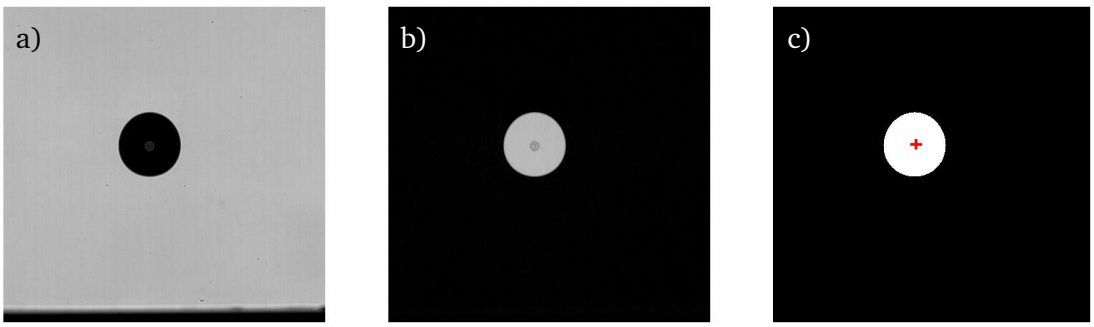

Figure 3.7.: The method for determination of the drop contour; a) raw image, b) subtraction of the raw image from the reference image, and c) binarized image. The center of the drop is marked with a red cross and is tracked to evaluate the impact velocity.

One common method for the evaluation of the equivalent diameter of the drop is to assess the drop area by image-processing and thereby derive the equivalent diameter of the drop (2D method). The drop area is the product of the total amount of white pixels (depicted in Fig. 3.7c) and the area of one pixel. This method is valid for perfectly spherical drops. However, the generation of drops in this study was accompanied by a slight oscillation. This is mainly due to the use of liquid with low viscous and high density ($\mu_{\mathrm{l,FC\text{-}72}} = 4.5 \cdot 10^{-4}$ kg m^{-1} s^{-1} and

$\rho_{l,FC\text{-}72} = 1620$ kg m^{-3} at saturation pressure of 1 bar), leading to long oscillation decay time [102].

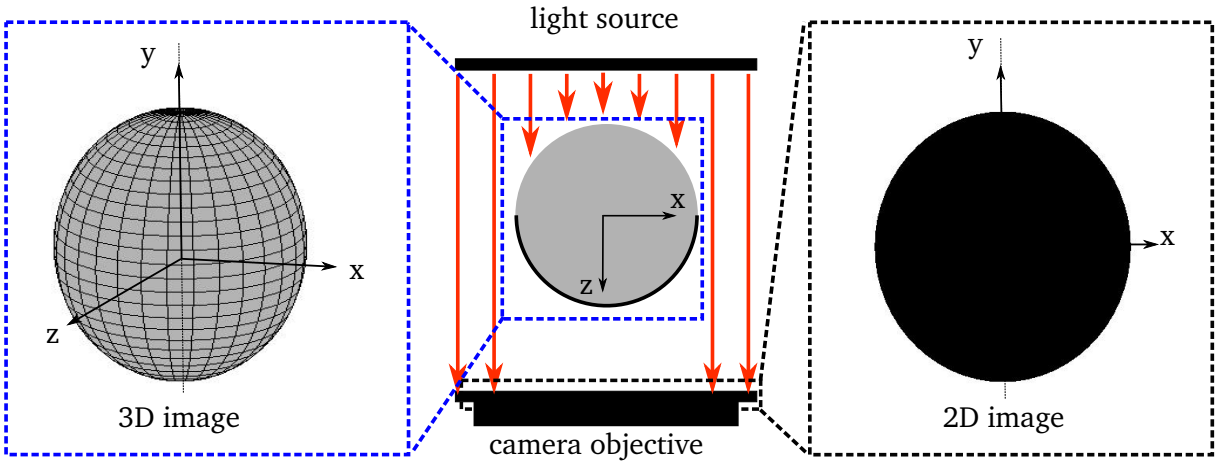

Figure 3.8.: Three-dimensional representation of the drop (left), schematic of the shadowgraphy technique (middle), the two-dimensional image captured by the camera objective, which is the orthogonal projection of the drop (right).

In order to minimize the effect of drop oscillation on diameter evaluation, the equivalent diameter of the drop is evaluated by the three-dimensional volume integration method illustrated in Fig. 3.8. This method is based on the fact that the two-dimensional images of the drop captured by the high-speed camera using a telecentric lens are orthogonal projections of the drop. In this method, the drop is assumed to be symmetric about the vertical axis. Based on this method, the drop volume is comprised of many rings of square cross-section, as indicated in Fig. 3.9.

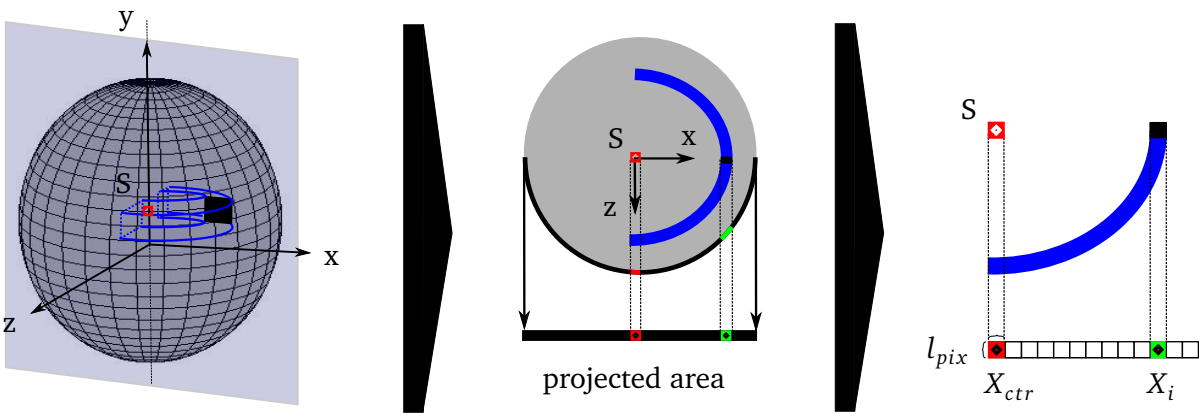

Figure 3.9.: The method for determination of the drop volume from integrating the volume of the rings (left); projected pixels from two-dimensional image (middle), the method to evaluate the volume of each ring (right).

The drop volume is the sum of the volumes of all these rings and is calculated as

$$V = \sum_{n=1}^{N} V_{\text{ring,n}} \,, \tag{3.1}$$

where V denotes the drop volume and N the number of pixels within the projected area. $V_{\mathrm{ring,n}}$ is the volume of a half-ring defined as

$$V_{\mathrm{ring,n}} = l_{\mathrm{arc}} l_{\mathrm{pix}}^2 \,, \tag{3.2}$$

where l_{pix} denotes the pixel size (10.87 μm), and l_{arc} is the perimeter of the half-circle depicted on the right side of Fig. 3.9, and is defined as

$$l_{\mathrm{arc}} = \pi l_{\mathrm{pix}} \,|\, X_{\mathrm{i}} - X_{\mathrm{ctr}} \,|\,, \tag{3.3}$$

where $|\, X_{\mathrm{i}} - X_{\mathrm{ctr}} \,|$ is the distance between pixel number i and the center of the drop in x-direction. By inserting equations 3.2 and 3.3 in 3.1, the following equation for the drop volume is obtained

$$V = \pi l_{\mathrm{pix}}^3 \sum_{n=1}^{N} |\, X_{\mathrm{i}} - X_{\mathrm{ctr}} \,| \;. \tag{3.4}$$

The following equation is used to evaluate the equivalent diameter of the drop

$$D = \sqrt[3]{6\frac{V}{\pi}} \,. \tag{3.5}$$

Figure 3.10 compares the drop diameters assessed from the method described at the beginning of this section (2D method) and the three-dimensional volume integration method of three arbitrary drops impacting the surface. One can notice that the fluctuations of the drop diameter during five frames before impact is eliminated by using the three-dimensional volume integration method.

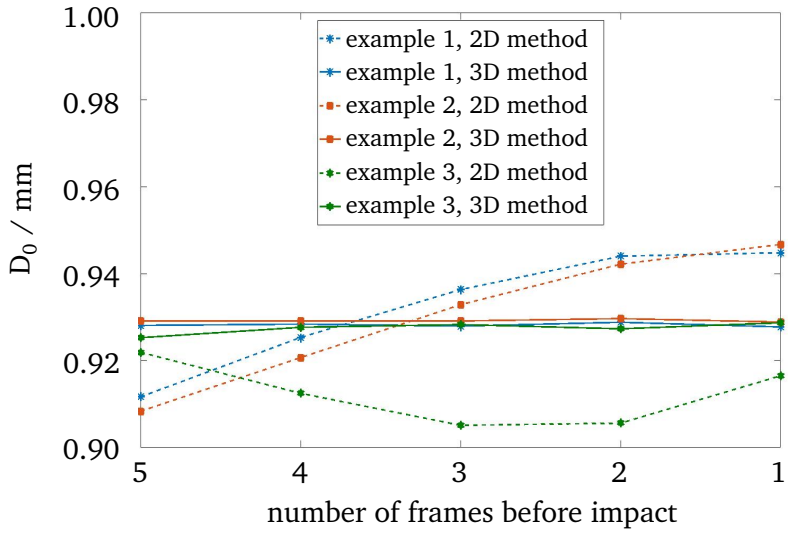

Figure 3.10.: Comparison between 2D and 3D methods of drop diameter evaluations for five frames before impact.

Figure 3.11 illustrates the method employed to evaluate the impact velocity. In order to calculate the impact velocity, the velocity of the drop for five frames before impact is initially calculated.

The velocity is the ratio between the displacement of the drop center and the time interval, which is 1 ms.

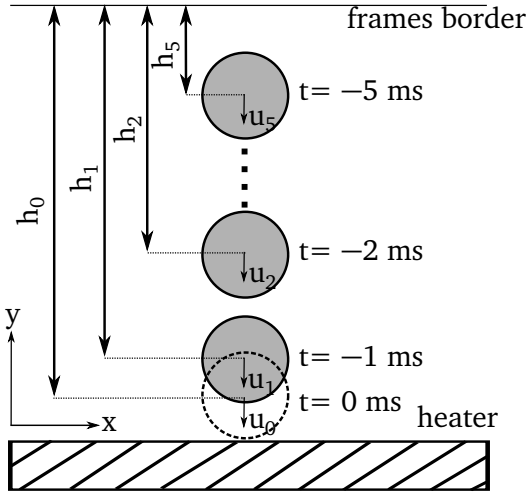

Figure 3.11.: The applied method to evaluate the impact velocity; the average drop velocity for five images before impact is evaluated, the impact velocity is evaluated by extrapolating the curve fitted to the velocities.

Due to the fast impact dynamics, the exact moment and velocity of impact are unknown. Therefore, the distance between the center of the drop in the frame immediately preceding the impact and the heater surface is assessed. Then the law of conservation of energy in the case of free fall for two different time instances is used:

$$E_{\text{kinetik},t'} + E_{\text{potential},t'} = E_{\text{kinetik},t'+1} + E_{\text{potential},t'+1}\,, \tag{3.6}$$

where t denotes the time instant, E_{kinetik} is the kinetic energy equal to $\frac{1}{2}mu^2$, and $E_{\text{potential}}$ is the potential energy equivalent to mgh. This gives

$$\frac{1}{2}m_{t'}u_{t'}^2 + m_{t'}gh_{t'} = \frac{1}{2}m_{t'+1}u_{t'+1}^2 + m_{t'+1}gh_{t'+1}\,. \tag{3.7}$$

By assuming a constant drop mass for the two time intervals and reforming the equation 3.7 in terms of $u_{t'+1}$, the following equation can be expressed:

$$u_{t'+1} = \sqrt{2g(h_{t'} - h_{t'+1}) + u_{t'}^2}\,. \tag{3.8}$$

Based on equation 3.8, a square root function is fitted to the calculated velocities. The impact velocity is finally evaluated by curve extrapolation.

3.7.2 IR thermography for wall temperature measurement

Following information regarding high-resolution temperature measurement techniques given in Section 3.2, IR thermography has been selected to capture the temperature distribution on the back side of the heater at an extremely close distance to the liquid–solid interface (less than 1 μm).

IR camera systems can be distinguished by either the optical arrangement, detector technology, or the wavelength band of the detector [103, 104]. Two optical arrangements, namely staring systems and scanning systems, exist in the market. In a staring system, the surface radiation of the object is transferred to the infrared sensor arrays or focal-plane arrays. Therefore, every element of the object is transferred to a corresponding sensor element of the focal-plane. In a scanning system, however, the surface radiation of the object is transfered point by point to a single infrared detector using oscillating mirrors and rotating prisms. This arrangement introduces additional noises to the measurement. Thus, the majority of IR cameras that are used today are staring systems.

The detector technologies used in IR cameras are broken down into two categories: thermal detectors and quantum detectors. A microbolometer made of a metal or semiconductor material is a common type of thermal detector. Quantum detectors are made of materials such as HgCdTe (CMT), which generally operate faster with more sensitivity than thermal detectors. IR cameras with quantum detectors operate based on the change of state of electrons in a crystal structure reacting to incident photons. These cameras must be actively cooled to reach acceptable photon counts, and, accordingly, signal-to-noise ratio. This makes the IR cameras with quantum detectors relatively large and expensive.

IR cameras operate over one of three wavelength regions or bands of the electromagnetic spectrum. The wavelength band employed depends on application and measurement requirements. These three bands are: i) short-wavelength infrared (SWIR), expanding from 0.4 to $2-3$ μm, ii) mid-wavelength infrared (MWIR), expanding from $2-3$ to 5 μm, and iii) long-wavelength infrared (LWIR), expanding from 8 to 12μm. SWIR cameras are generally used for laser applications. MWIR cameras generally provide thermal imaging with higher quality and resolution as well as lower noises in comparison with the LWIR cameras.

The IR camera employed in the scope of this work is a staring semi-conductor photon detector camera working in the spectral range of 3.4 - 5.1 μm with 14 bits ($2^{14} = 16384$) digital resolution[12]. The thermal sensitivity of the camera is less than 10 mK. A field of view of 224 pixel x 224 pixel is resolved by $\Delta x_{\mathrm{res,IR}} = 29.27$ μm/pixel, resulting in the FOV of 6.56 mm x 6.56 mm. In order to fit the largest drop for drop size investigations (see Section 5.1.3) and two drops for horizontal drop coalescence investigations (see Section 5.2.2) in the FOV of the IR camera, its spatial resolution is set to the lower resolution of 40.82 μm/pixel, resulting in the FOV of 9.14mm x 9.14mm.

The IR camera with the framerate of 1000 Hz is synchronized to the high-speed B/W camera described in Section 3.7.1. Within the integration time period, each pixel of the detector chip

[12] Thermosensorik® CMT 256 M HS

is discharged corresponding to the incident photons. The remaining charge is read out and mapped to the digital resolution of the camera so that 0 represents the fully discharged pixel and 16383 represents the fully charged pixel. Higher surface temperatures lead to higher energy fluxes introduced to the pixel, and thus, lower digital values. Each integration time possesses a saturation temperature, defined as the maximum temperature that can be measured by each pixel within the integration time period.

The radiative energy flux emitted by a black body surface according to the Stefan-Boltzmann law is:

$$j = n^2 \sigma_{\mathrm{SB}} T^4 \,, \tag{3.9}$$

where j denotes the radiative energy flux, n denotes the index of refraction of the medium the radiation is emitted into, and σ_{SB} denotes Stefan-Boltzmann constant. In this study, the radiation is emitted from the CrN surface with an unknown emission coefficient, $\varepsilon_{rad,CrN}$, through CaF_2 medium with refraction index unequal to 1.

In this study, the radiative energy flow of the CrN layer, J_{CrN}, is:

$$J_{CrN} = A\varepsilon_{\mathrm{rad,CrN}} n^2 \sigma_{\mathrm{SB}} T^4 + \rho_{\mathrm{rad,CrN}} J_{\mathrm{sur}} \,, \tag{3.10}$$

where A is the surface area observed by one pixel, $\varepsilon_{\mathrm{rad,CrN}}$ is the emissivity of the CrN surface seen by the pixel, $\rho_{\mathrm{rad,CrN}}$ is the reflectivity of the CrN surface seen by the pixel, and J_{sur} is the radiative energy flow coming from the surroundings. The radiation is damped by absorption within the CaF_2 substrate according to the following equation [105]:

$$J(z) = J_{\mathrm{CrN}} e^{-k_{\mathrm{rad,CaF}} z} = \tau_{\mathrm{rad,CaF}} J_{\mathrm{CrN}} \,, \tag{3.11}$$

where $J(z)$ is the radiative energy flow after passing distance z, and $k_{\mathrm{rad,CaF}}$ is the absorption coefficient of the medium. According to the data sheet provided by the CaF_2 manufacturer, the mean absorption coefficient of the CaF_2 in the spectral range of the IR camera is $k_{\mathrm{rad,CaF}} = 5.1293 \cdot 10^{-4}\ \mathrm{mm}^{-1}$ [98]. This leads to a transmissivity of $\tau_{\mathrm{rad,CaF}} = 0.998$ at $z = 4$ mm (thickness of the CaF_2 substrate).

The emissivity of the substrate material can be calculated by combining radiative energy conservation ($\tau_{\mathrm{rad,CaF}} + \rho_{\mathrm{rad,CaF}} + k_{\mathrm{rad,CaF}} = 1$) with Kirchhoff's law ($k_{\mathrm{rad,CaF}} = \varepsilon_{\mathrm{rad,CaF}}$) for a system in thermodynamic equilibrium, and neglecting the reflection within the medium ($\rho_{\mathrm{rad,CaF}} = 0$)

$$\varepsilon_{\mathrm{rad,CaF}} = 1 - \tau_{\mathrm{rad,CaF}} = 0.002 \,. \tag{3.12}$$

This shows that the radiation emitted by the substrate is negligible. The net radiation introduced into every single pixel of the camera chip, J, can be evaluated by combining equations 3.10 and 3.11, and considering the radiation, J_{pix}, emitted by the physical pixel of the measurement detector chip itself

$$J = \tau_{\mathrm{rad}} A\varepsilon_{\mathrm{rad,CrN}} n^2 \sigma_{\mathrm{SB}} T^4 + \tau_{\mathrm{rad}} \rho_{\mathrm{rad,CrN}} J_{\mathrm{sur}} - J_{\mathrm{pix}} \,, \tag{3.13}$$

where τ_{rad} is the overall transmissivity of the heater substrate, the IR camera lens system, and the air in between the detector and the heater. Since the chip characteristics and internal transformation of the camera electronics are unknown, an in situ calibration of the infrared signal versus temperature for each pixel is necessary. Based on equation 3.13 and on 14 bits as the digital resolution of the camera, the calibration function between the temperature and digital intensity representation I_{dig} can be formulated as

$$T = A[(16383 - I_{\mathrm{dig}}) + B]^{\frac{1}{4}} + C\,, \tag{3.14}$$

where constants A and B are related to unknown radiation properties from equation 3.13 and pixel characteristics including gain, offset, and integration time. Constant C is connected to an unknown data processing conducted by the frame grabber of the camera [30].

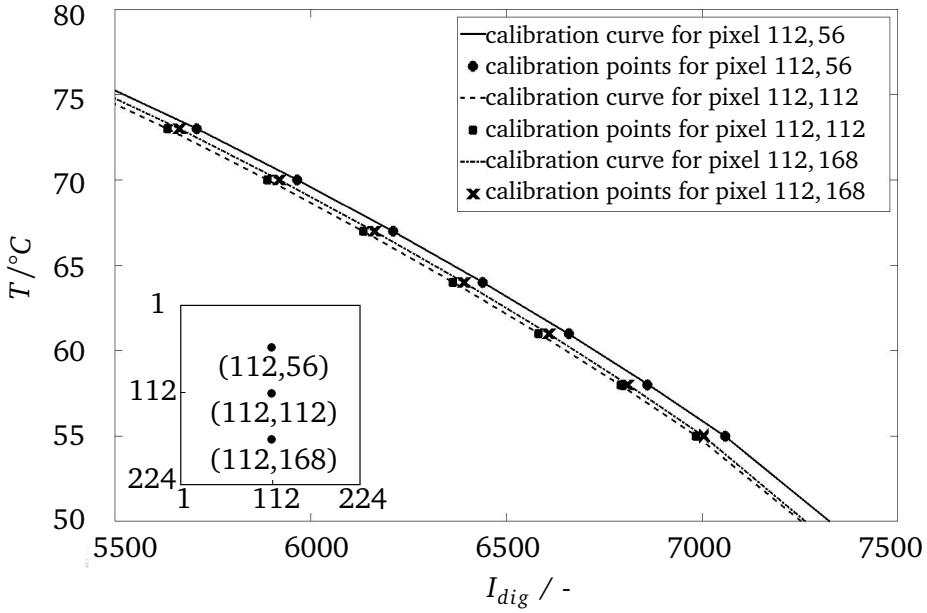

Figure 3.12.: Calibration curves for three exemplary pixels of the IR camera calibrated with 0.8515 ms integration time within the calibration temperature range from 55 to 71 °C (pixel positions within the IR FOV are shown in the bottom left corner).

The calibration process for infrared signal versus temperature has been performed after the measurements to avoid heater surface destruction. Neither heater nor IR camera is moved between measurements and calibration. The calibration is accomplished by pressing a copper block onto the top surface of the heater, where the Cr layer is sputtered. The calibration block is thermalized through interior channels by a thermostat. To minimize the influence of air temperature surrounding the lens of the IR camera, the cell temperature is set equal to the thermostat temperatures during the calibration process. To measure the reference temperature, a type K thermocouple is inserted in the center of the calibration block, approximately 1 mm above the Cr layer. Measurements are performed at several uniform constant temperature levels which cover the whole measurement temperature range. At each temperature level, 200 frames are recorded with the IR camera, once the temperature of the calibration block reaches stationary conditions (T_{calib} ±0.02 K). The framerate and integration time of the camera are equal to those taken during the measurements. The intensity value of every single pixel ($I_{\mathrm{dig,x,z}}$) is the average of measured intensities over the 200 frames. The evaluated intensity values are then correlated to the temper-

ature measurement of the thermocouple. For each pixel, constants A(x,z), B(x,z), and C(x,z) in equation (3.14) are assessed through a least square errors curve fitting algorithm in MATLAB®.

Figure 3.12 presents calibration curves for three exemplary pixels for the integration time of 0.8515 ms. As can be seen, the measurement points are matched well with the calibration curves using the aforementioned constants. One can also notice that the calibration curve for each pixel differs from the other. This indicates how crucial the pixel-wise in-situ calibration procedure is.

3.7.3 Heat flux calculation procedure

One of the main targets in this work is to quantify the heat flux distribution from the heater to the fluid domain. The local heat flux is derived from the temperature field by solving a transient three-dimensional conduction equation within the CaF_2 substrate using the finite volume method within the CFD toolbox OpenFOAM. The governing equation for the heat transfer within the CaF_2 heater substrate has the following form:

$$\frac{\partial T}{\partial t} = \alpha_{\mathrm{CaF}} \nabla^2 T \,, \tag{3.15}$$

where α_{CaF} denotes the thermal diffusivity of the substrate material. Since both Cr and CrN layers on the CaF_2 substrate are extremely thin, the energy storage and thermal resistance in these layers are negligible, and they are not considered in the numerical calculation.

The Courant number is a measure of how much information traverses a computational grid cell (Δx_{num}) in a given time-step (Δt_{num}) and must be below 1 in order for the numerical calculation to be stable. The Courant number is defined as

$$Co = \frac{u_{num,max} \Delta t_{\mathrm{num}}}{\Delta x_{\mathrm{num}}} \,, \tag{3.16}$$

where $u_{num,max}$ is the maximum velocity with which information can propagate in the numerical calculation and can be calculated by

$$u_{num,max} = \frac{\alpha_{\mathrm{CaF}}}{\Delta x_{\mathrm{num}}} \,. \tag{3.17}$$

The maximum time step size is calculated to be 0.239 ms by inserting the data for $\alpha_{\mathrm{CaF}} = 3.575 \cdot 10^{-6}$ m^2 s^{-1} and $\Delta x_{\mathrm{num}} = \Delta x_{\mathrm{res,IR}} = 29.27 \cdot 10^{-6}$ m. Considering the time spacing of 1 ms between the temperature fields captured by the IR camera, the temperature fields are linearly interpolated in-between frames to obtain $\Delta t_{\mathrm{num}} = 0.1$ ms, and, accordingly, Co= 0.417, to ensure the convergence of the calculation. The temperature field at the numerical time instant of t_{num} is calculated by linear interpolation of ten values at each pixel between two subsequent frames of the IR camera at time t_{IR} and $t_{\mathrm{IR+1}}$ as the following equation:

$$T(x,z,t_{\mathrm{num,i}}) = T(x,z,t_{\mathrm{IR}}) + \frac{\mathrm{i}}{10}[T(x,z,t_{\mathrm{IR+1}}) - T(x,z,t_{\mathrm{IR}})] \,\mathrm{with\,i} = 1...10 \,. \tag{3.18}$$

Mesh

As depicted in Fig. 3.13, the computational domain is the volume of the CaF_2 substrate appearing in the FOV of the IR camera. This region is discretized into a numerical mesh with three different zones. In the uppermost zone (zone 1), the high spatial resolution of the mesh equal to the spatial resolution of the IR camera on the upper mesh block is implemented. The thickness of this zone is 2 mm and its volume is resolved by 68 cells in thickness direction. If such a fine resolution had been implemented for the entire thickness of the heater, the total number of cells would be 6.8 million, which leads to a very long computation time. To save computation time, two additional zones with lower spatial resolutions are defined: zone 2 from a depth between 2 and 3 mm, where the resolution reduces two-fold, and zone 3 from a depth of 3 mm onwards, where the resolution reduces four-fold in comparison to zone 1. This step-wise coarsening approach reduces the number of the cells from 6.8 to 3.6 million, and, accordingly, the computation time. The results of heat flux assessed by a fully resolved mesh are compared with the results from the step-wise coarsened mesh, and no significant differences were observed.

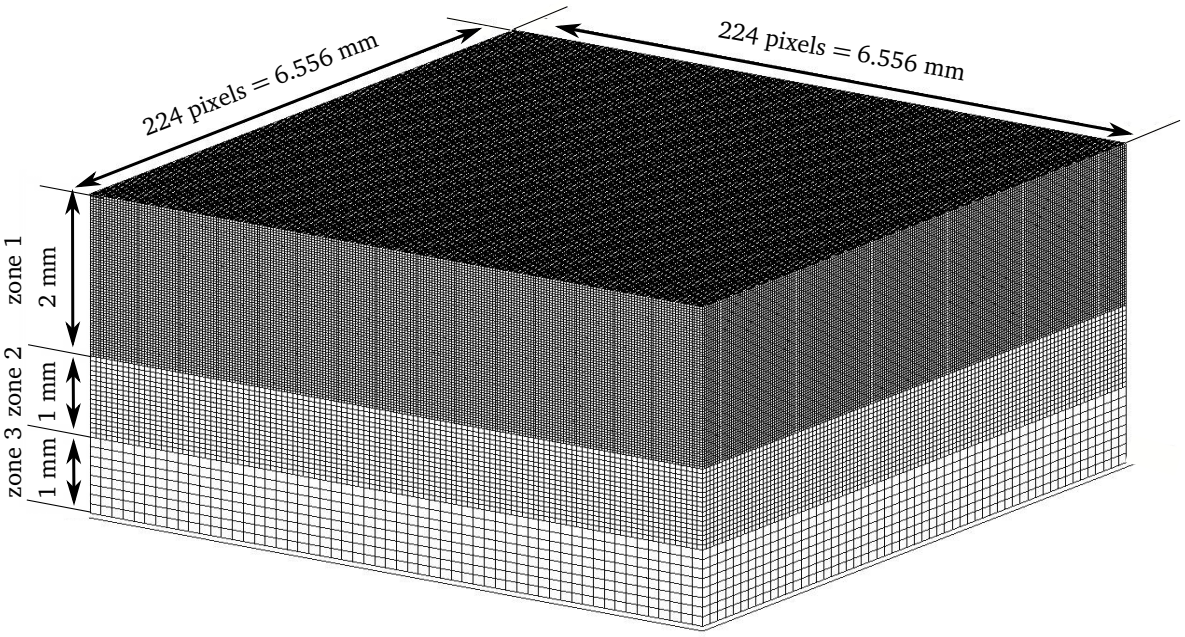

Figure 3.13.: Three-dimensional numerical mesh for the heat flux calculation.

Boundary conditions

Figure 3.14 shows the boundary conditions employed for the numerical heat flux calculation. To remove the noises of the IR images, the temperature field is smoothed with a symmetric Gaussian lowpass filter of the size of 10 elements with a standard deviation of 2 in MATLAB. The smoothed temperature field obtained from IR thermography (see Section 3.7.2) is used as the boundary condition at the top of the computational domain, which corresponds to the interface between CaF_2 substrate and black CrN layer.

The other boundaries of the computational domain are assumed to be adiabatic (see Fig. 3.13). This assumption is verified by numerical calculations described in [30].

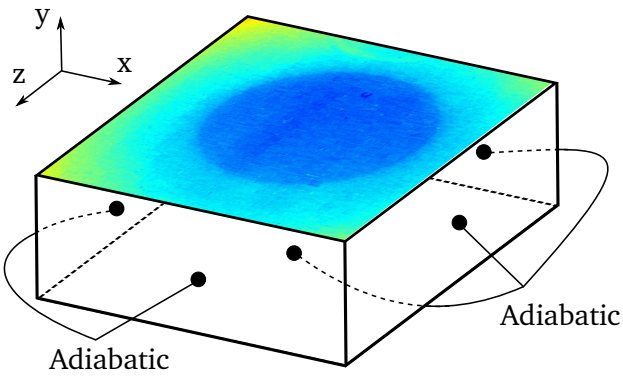

Figure 3.14.: Boundary conditions for the heat flux calculation.

Initial condition

As an initial condition, the three-dimensional temperature field in the computation domain is set to the steady state solution evaluated from the first two-dimensional temperature field acquired through IR thermography.

Post-processing

The outcomes of numerical calculations are the two-dimensional heat flux fields at the interface between the CaF_2 substrate and the black CrN layer. Under the assumption of homogeneous thickness of the Cr layer (and, accordingly, uniform electrical power density) and negligible thermal resistance and thermal storage of extremely thin Cr and CrN layers, the heat flux at the fluid–solid interface is calculated as

$$q(x,z,t) = q_{\text{num}}(x,z,t) + q_{\text{in}}\,, \tag{3.19}$$

where $q_{\text{num}}(x,z,t)$ is the outcome of numerical calculation and q_{in} is the electrical power density at the heater, calculated with the following equation:

$$q_{\text{in}} = \frac{R_{\text{hl}} I^2}{lw}\,. \tag{3.20}$$

Herein, R_{hl} denotes the electrical resistance of the Cr heating layer measured according to the description presented in 3.4, l and w denote the length and width of the Cr layer, respectively, and I denotes the electrical current supplied to the Cr layer.

3.7.4 Contact line radius detection procedure

Besides the heat flux distribution, the contact line radius is of major interest when investigating drop impingement onto the heated surfaces. In this section, the methods applied to evaluate the radius of the three-phase contact line are outlined in detail.

In general, two approaches can be implemented to evaluate the contact line radius; contact line radius evaluation through i) shadowgraphy and ii) post-processing of IR images. The former approach was found to be not proper for all cases of drop impact due to the following reasons:

1. The drop after impact moves in a random direction and consequently does not stay in the focus of the B/W camera. This phenomenon is even more profound at higher wall superheats, at which the apparent contact angle becomes larger.
2. At elevated pressures the density ratio (and by that the ratio of the indices of refraction) is reduced, which leads to lower contrast at the interface.

Therefore, acquiring reliable information about the contact line radius from the shadowgraphy technique is questionable. Hence, the IR images are used to detect the contour of the three-phase contact line and to evaluate its radius. Depending on the heat flux distribution, two stages of drop impact and thus two detection methods are employed.

At the early stages of impact (t < 4 ms), the heat flux field is almost homogeneous (see Section 5.1, Fig. 5.1). At this stage, the drop footprint has been determined by defining an appropriate threshold (1 kW m^{-2} $\leq \dot{q}_{thres} \leq$ 4 kW m^{-2}) that distinguishes high and low heat flux regions. Then the results are binarized, and the wetted area and the radius of the three-phase contact line are evaluated.

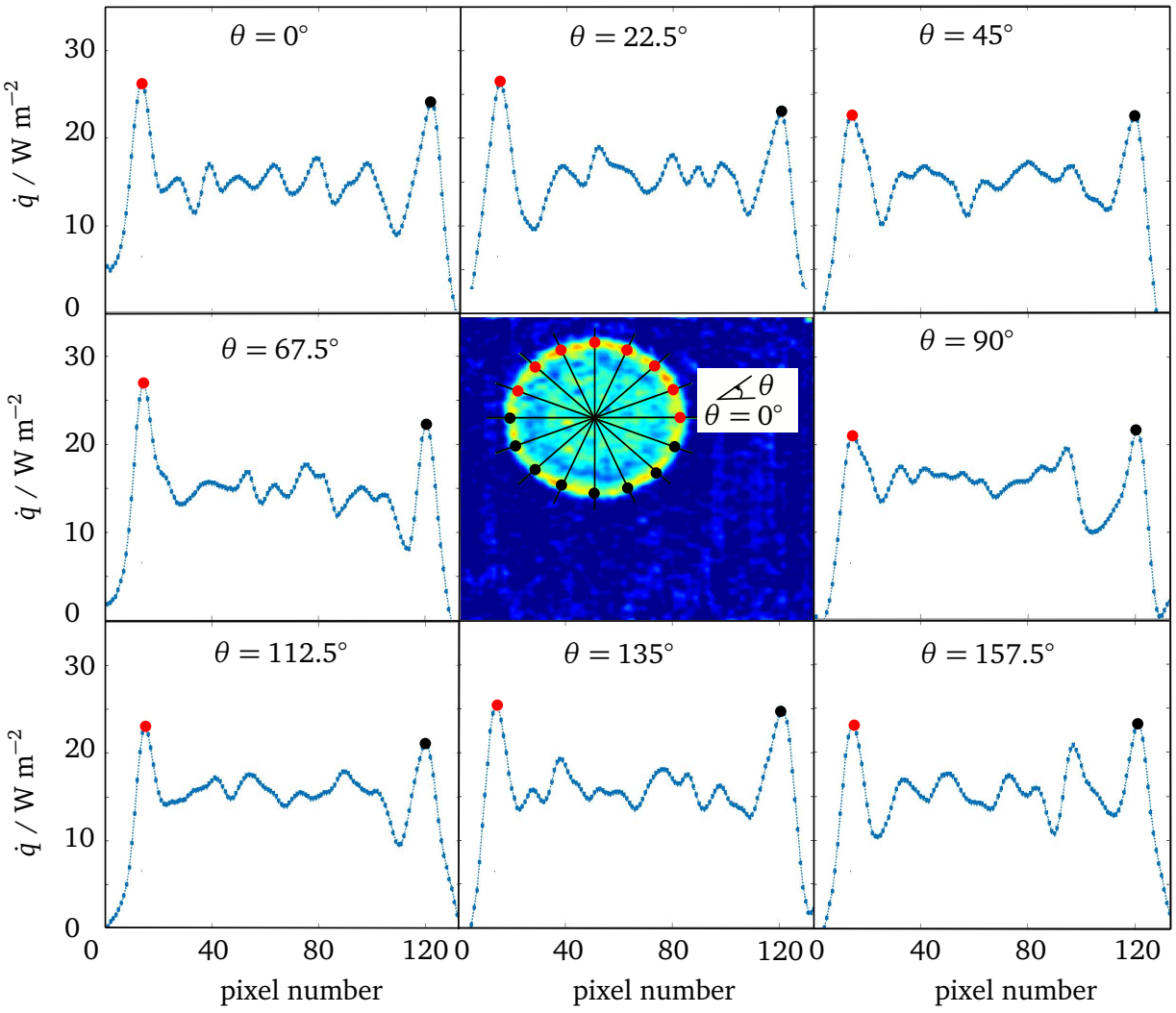

Figure 3.15.: Method for detection of three-phase contact line position; 8 lines passed through the image of the heat flux field (middle), the heat flux along all lines, and their corresponding maximums, which show the position of the three-phase contact line.

At the later stages of impact shortly before the onset of the receding phase (t $\geq$ 4 ms), the heat flux distribution attains a strong local maximum in the immediate vicinity of the three-phase contact line, forming a ring-shaped region. The position of the contact line and its radius from this moment on is assumed to be in the region where the maximum heat flux occurs. Figure 3.15 presents the employed method to evaluate the contact line position and its radius with respect to the maximum heat flux. In this method, several lines at distinct angles are passed through the center of the wetted area, and the position of the two heat flux maximums along each line is detected. A circle is fitted to the detected points to determine the contact line position and its radius. In principle, more lines lead to better estimation of the position of the contact line; however, the standard deviation of the radius in the case of more than 8 lines is 2%. Therefore, to save computing time, eight lines have been used to detect the position of the contact line and calculate the contact line radius.

Figure 3.16 compares the evolution of the contact line radius evaluated from the B/W and IR images at $\Delta T = 4.5$ K and $P_R = 0.05$. As expected, a good agreement between the curves at low wall superheats and reduced pressures can be observed.

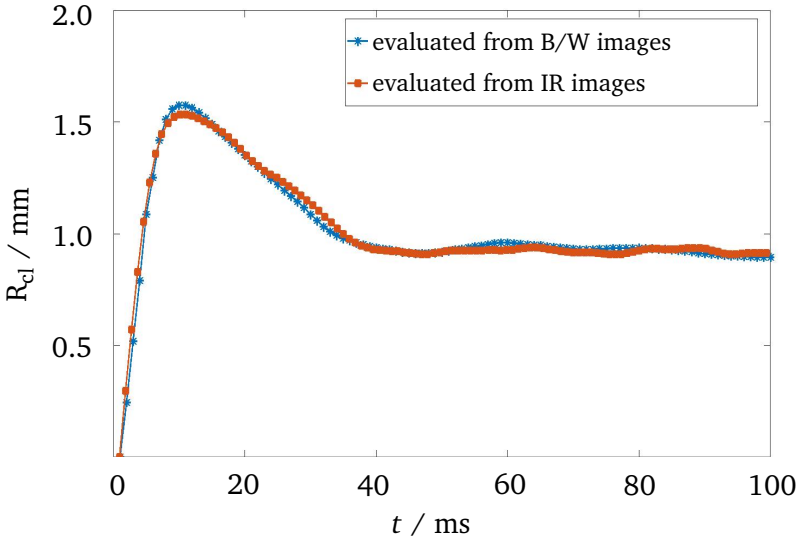

Figure 3.16.: Comparison between contact line radius evaluated from the B/W and IR images at $\Delta T = 4.5$ K and $P_R = 0.05$.

3.7.5 Heat flow and cumulative heat flow calculation procedures

The heat flow for each time step, $\dot{Q}_{\text{drop}}(t)$, is evaluated by the integration of local heat flux from equation 3.19 over the drop footprint depicted in the middle of Fig. 3.15

$$\dot{Q}_{\text{drop}}(t) = l_{\text{pix}}^2 \sum_{x=1}^{224} \sum_{z=1}^{224} \dot{q}_{\text{drop}}(x,z,t)\,, \tag{3.21}$$

where $l_{\text{pix}} = \Delta x = \Delta z = 29.27 \cdot 10^{-6}$ m is the pixel size, and $\dot{q}_{\text{drop}}(x,z,t)$ is defined as:

$$\dot{q}_{\text{drop}}(x,z,t) = \begin{cases} \dot{q}(x,z,t), & \text{if} \quad x,z \in \text{A}_{\text{drop}}\,, \\ 0, & \text{if} \quad x,z \notin \text{A}_{\text{drop}}\,. \end{cases} \tag{3.22}$$

Herein A_{drop} denotes the area of the drop footprint. The total heat transferred to the drop is the integration of the heat flow from equation 3.21 over time and can be expressed as:

$$E_{drop}(t) = \sum_{t=1}^{t} \dot{Q}_{drop}(t)\,. \tag{3.23}$$

3.7.6 Measurement uncertainties

The evaluated measurement uncertainties described in this section are based on the worse case assumption of linear error propagation [106].

Drop diameter and impact velocity

Figure 3.17 shows the magnified view of the B/W picture for one exemplary measurement. As can be seen, the boundary of the drop can be easily distinguished within one pixel due to high picture contrast. Therefore, the relative uncertainty of the drop diameter is equal to the size of two pixels,

$$\Delta D_{rel} = 2 l_{pix} = \pm 21.74\ \mu\text{m}\,. \tag{3.24}$$

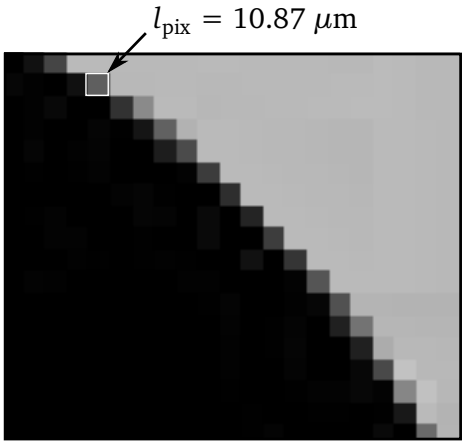

Figure 3.17.: Magnified view of the B/W picture for one exemplary measurement.

The relative uncertainty of the impact velocity is calculated by the propagation uncertainty of center displacement corresponding to one pixel, which is

$$\Delta u_{rel} = \frac{l_{pix}}{t} = \pm 10.87\ \text{mm s}^{-1}\,. \tag{3.25}$$

To evaluate the absolute uncertainties of the calculation procedures related to drop diameter and impact velocity, a bunch of drop impact measurements have been performed, and their drop diameters and impact velocities according to the methods described in 3.7.1 are assessed. Since the needle size and height, liquid properties, and ambient conditions remained unchanged, the drop diameters and impact velocities must be constant. The standard deviation for the calculated drop diameters ($\Delta D_{stat} = 9.32\ \mu$m) and impact velocities ($\Delta u_{stat} = 11.23$ mm s^{-1}) are added

to the relative uncertainty. These refer to the uncertainty of the calculation procedures of drop diameter and impact velocity, which are

$$\Delta D_{\text{abs}} = \Delta D_{\text{rel}} + \Delta D_{\text{stat}} = \pm 31.06\ \mu\text{m}\,, \tag{3.26}$$

$$\Delta u_{\text{abs}} = \Delta u_{\text{rel}} + \Delta u_{\text{stat}} = \pm 22.10\ \text{mm s}^{-1}\,. \tag{3.27}$$

Temperature measurements

As mentioned earlier, type K thermocouples (TC) are employed to measure the temperature at different locations inside the cell and at the calibration block. Prior to the experiments, the thermocouples are calibrated against a Pt100 temperature probe as a reference temperature. The Pt100 has an absolute accuracy of $\Delta T_{\text{Pt100}} = \pm 0.15$ K. For each thermocouple, a polynomial curve was fitted to the measured temperature points and then checked versus the Pt100 reference temperature. The maximum deviation of the polynomial curve from reference temperature for all thermocouples was found to be within $\Delta T_{\text{TC}\Leftrightarrow\text{Pt100}} = \pm 0.25$ K. This leads to relative and absolute measurement uncertainties for the thermocouples of

$$\Delta T_{\text{TC,rel}} = \Delta T_{\text{TC}\Leftrightarrow\text{Pt100}} = \pm 0.25\ \text{K}\,, \tag{3.28}$$

$$\Delta T_{\text{TC,abs}} = \Delta T_{\text{TC,rel}} + \Delta T_{\text{Pt100}} = \pm 0.40\ \text{K}\,. \tag{3.29}$$

Pressure measurements

The measurement accuracy of the pressure transducer during the entire operating pressure of $0 \ldots 25$ bar and output voltage of $0 \ldots 10$ V is 0.05%. This results in the measurement uncertainty of the sensor of $\Delta p_{\text{sensor}} = \pm 12.5$ mbar. Considering the DAQ read out measurement uncertainty of $\Delta U_{\text{DAQ}} = \pm 0.98$ mV, the absolute pressure measurement uncertainty can be calculated as

$$\Delta p_{\text{abs}} = \Delta p_{\text{sensor}} + \frac{dp}{dU}\Delta U_{\text{DAQ}} = \pm 14.95\ \text{mbar}\,. \tag{3.30}$$

IR thermography

The temperature sensitivity curves of the IR camera versus temperature for different integration times are depicted in Fig. 3.18. One can notice that higher integration times result in increasing the temperature measurement sensitivity. However, the maximum measurable temperature at which the pixels reach saturation is lower for higher integration times. Therefore, selecting the appropriate integration time is a trade-off between desired measuring temperature and measurement sensitivity. In the framework of this study, the integration time is always set to the highest value of 0.8515 ms, except for investigations of the influence of system pressure, at which the cell temperature has reached its highest value. The integration time, in this case, is set to 0.5931 ms.

The noise level of the chip detector from the IR camera represents the temperature measurement uncertainty of the IR camera. This noise level, or Noise Equivalent Temperature Difference (NETD), is a function of temperature and the optical setup of measurement. The NETDs provided by the IR camera manufactures are only reliable for a specific temperature level.

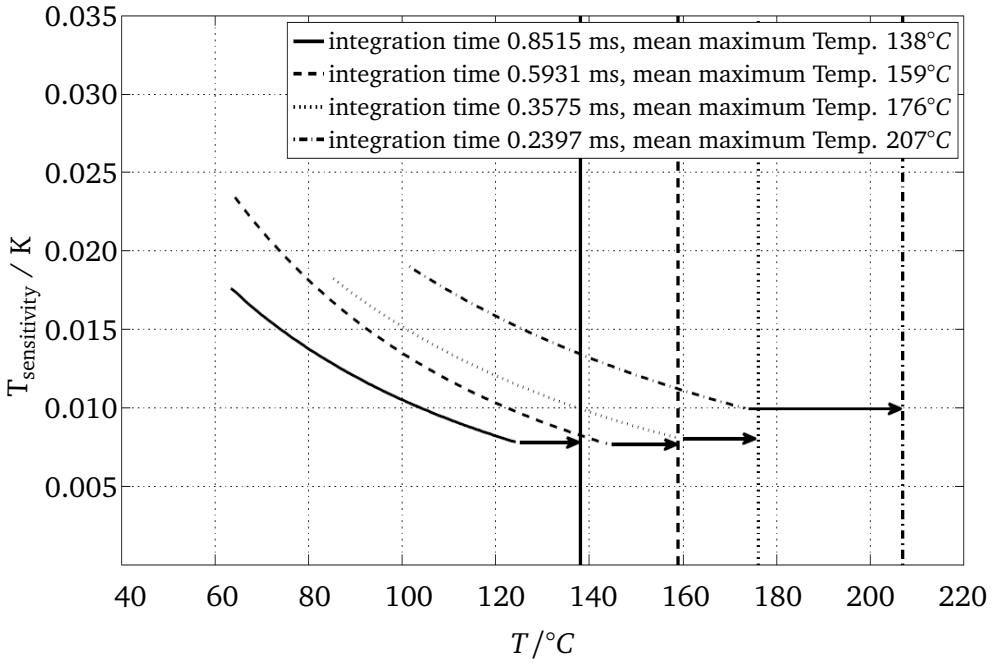

Figure 3.18.: Mean noise equivalent temperature difference (NETD) for different integration times of the IR camera, reprinted from [30].

Calibration images are used to calculate the NETD for the whole measurement range. For each calibration temperature, the difference between the maximum and minimum temperature values of each pixel for all 200 frames is calculated. This corresponds to the noise of the IR camera chip (NETD) since the temperature is maintained constant during one calibration sequence. Figure 3.19a presents the mean NETD of the IR camera versus temperature for the integration time of 0.8515 ms.

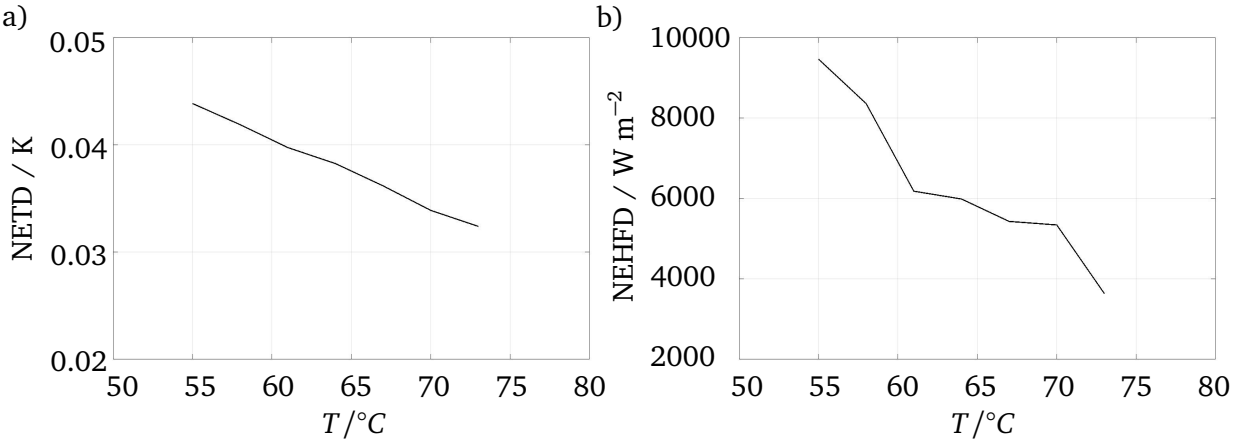

Figure 3.19.: a) Mean noise equivalent temperature difference (NETD) and b) mean noise equivalent heat flux difference (NEHFD) at integration time of 0.8515 ms in the temperature range of 55 to 73 °C.

The relative wall temperature measurement uncertainty is evaluated by adding the maximum NETD calculated from the calibration images and the temperature sensitivity as depicted in Fig. 3.18. Since the calibration was performed using a thermocouple, its measurement uncertainty is added to calculate the absolute wall temperature measurement uncertainty

$$\Delta T_{\mathrm{IR,rel}} = \pm 0.18 \text{ K}, \tag{3.31}$$

$$\Delta T_{\mathrm{IR,abs}} = \Delta T_{\mathrm{IR,rel}} + \Delta T_{\mathrm{TC,abs}} = \pm 0.58 \text{ K}. \tag{3.32}$$

Heat flux calculation

The uncertainty of the heat flux calculations arises from i) deviation from the assumption of adiabatic boundary conditions at the sides and the back of the computational domain with reality, and ii) the NETD of the IR camera. The assumption of adiabatic boundary conditions is validated in [30], in which the heater was in direct contact with the metal cell. This assumption is even more reliable for this work where the heater is installed on top of a PEEK structure with very low thermal conductivity ($\lambda_{\mathrm{PEEK}} = 0.25$ W m^{-1}K^{-1}).

The NETD of the IR camera results in deviations in heat flux, referring to noise equivalent heat flux difference (NEHFD). To calculate the NEHFD, the heat flux fields corresponding to the calibration images are evaluated from the method described in Section 3.7.3. The heat flux should be equal to zero since the temperature is constant and homogeneous during the calibration process. The NEHFD of each pixel is equal to the difference between the maximum and minimum value of the heat flux. Figure 3.19b presents the mean NEHFD versus temperature for the integration time of 0.8515 ms.

The overall heat flux uncertainty transferred through the liquid–solid interface is the superposition of the NEHFD and uncertainty of the input heat flux calculations governed by the uncertainty of the current measurement. The employed power supply has the maximum current output deviation of $\Delta I_{\mathrm{PS}} = 6$ mA and maps its output range of $0 \ldots 5$ A to an analog voltage signal of $0 \ldots 10$ V read out by the DAQ with an uncertainty of $\Delta U_{\mathrm{DAQ}} = 0.98$ mV. Considering the heater area of $41.7 \cdot 15$ mm^2, the maximum heater resistance of 80 Ω and a maximum current of 220 mA, the maximum uncertainty of the input heat flux is

$$\Delta q_{\mathrm{in,max}} = 2\frac{R_{\mathrm{hl}} I}{lw}\left(\Delta I_{\mathrm{PS}} + \frac{dI}{dU}\Delta U_{\mathrm{DAQ}}\right) = \pm 365 \text{ W m}^{-2}. \tag{3.33}$$

The relative uncertainty of the heat flux calculation procedure is the calculated NEHFD in the calibration range, whereas the absolute uncertainty of the heat flux fields is increased by the uncertainty of the input heat flux

$$\Delta q_{\mathrm{rel}} = \pm 9463 \text{ W m}^{-2}, \tag{3.34}$$

$$\Delta q_{\mathrm{abs}} = \Delta q_{\mathrm{rel}} + \Delta q_{\mathrm{in,max}} = \pm 9828 \text{ W m}^{-2}. \tag{3.35}$$

According to [30], the NETDs and NEHFDs are larger at the integration time of 0.8515 ms and lower temperatures compared to the shorter integration times and larger temperatures. Therefore, the relative wall temperature measurement uncertainty and overall heat flux uncertainty are lower at elevated pressures, in which the cell temperature is high and the integration time is set to 0.5931 ms.

These uncertainty values are only maximum uncertainty estimations and only valid for single time steps and individual pixels of the heat flux fields. However, the uncertainty of the temperature and heat flow generated in the pixels covered by the drop footprint is the major interest in this work.

Temperature and heat flux at the liquid–solid interface

Figure 3.20 presents the histograms for temperature and heat flux distribution of a single frame from the calibration of the IR camera. A normal (Gaussian) distribution of temperature and heat flux around the mean value can be observed. The relative temperature and heat flux uncertainty for such a statistical distribution of the measurement noise is decreased with increasing the number of pixels (N_{pix}) averaged to generate them [107]. In this study, N_{pix} differs for each experiment and is defined as the number of pixels at the liquid–solid interface. As an example, the temperature and heat flux uncertainty for one case, which is depicted in Fig. 5.3 at $\Delta T = 6.9$ K are:

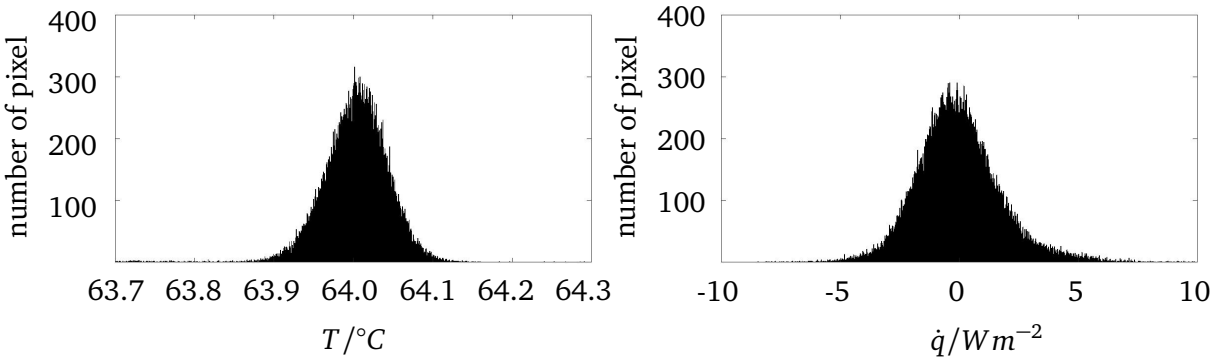

Figure 3.20.: Exemplary temperature (left) and corresponding heat flux (right) histogram for a single frame of a calibration point of the IR camera with an integration time of 0.8515 ms.

$$\Delta T_{\mathrm{drop,rel}} = \frac{\Delta T_{\mathrm{IR,rel}}}{\sqrt{N_{\mathrm{pix}}}} = \pm 1.75 \cdot 10^{-3}\ \mathrm{K}\,, \tag{3.36}$$

$$\Delta \dot{q}_{\mathrm{drop,rel}} = \frac{\Delta \dot{q}_{\mathrm{rel}}}{\sqrt{N_{\mathrm{pix}}}} \pm 95.5\ \mathrm{W\ m^{-2}}\,. \tag{3.37}$$

The absolute temperature and heat flux uncertainty at the liquid–solid interface are

$$\Delta T_{\mathrm{drop,abs}} = \Delta T_{\mathrm{drop,rel}} + \Delta T_{\mathrm{TC,abs}} = \pm 0.402\ \mathrm{K}\,, \tag{3.38}$$

$$\Delta \dot{q}_{\mathrm{drop,abs}} = \Delta \dot{q}_{\mathrm{drop,rel}} + \Delta \dot{q}_{\mathrm{in,max}} = \pm 460.5\ \mathrm{W\ m^{-2}}\,. \tag{3.39}$$

Heat flow

The measurement uncertainty of the heat flow for each time step is calculated through the propagation of the contact line radius and heat flux uncertainties

$$\Delta\dot{Q}(t) = \sqrt{(A_{\mathrm{drop}}(t)\Delta\dot{q}_{\mathrm{drop}})^2 + (\frac{\dot{Q}_{\mathrm{drop}}(t)}{A_{\mathrm{drop}}(t)}\Delta A_{\mathrm{drop}})^2}\,, \tag{3.40}$$

where

$$\Delta A_{\mathrm{drop}} = \pi\frac{\Delta D_{\mathrm{abs}}^2}{4}\,. \tag{3.41}$$

The contact line radius and heat flux uncertainties are constant. The heat flow uncertainty varies and is dependent upon the contact line radius and heat flux. Therefore, the maximum heat flow uncertainty for every single measurement occurs at the maximum of the contact line radius. As an example, the maximum heat flow uncertainty for one case, which is shown in Fig. 5.3 at $\Delta T = 6.9$ K is 0.056 W.

4 Numerical Methods

This chapter is devoted to a brief description of the numerical model employed for simulating the drop impingement onto a superheated surface. The model describes the hydrodynamics and heat transfer during single and multiple drop impact. In this model, evaporation has been introduced by Herbert et al. [24] and Batzdorf [2] and used for parametric studies in [7, 25]. This model pays special attention to the vicinity of the three-phase contact line. Thus, the heat and fluid flow is modeled on a micro-scale at the three-phase contact line (given in Section 4.1) and in the macro scale (given in Section 4.2), and finally, the results are coupled together. Some of the experimental results are compared with the model predictions. The comparison is addressed within the present thesis in Chapter 5.

4.1 Micro scale heat and fluid flow near contact lines

As already outlined in Section 2.2, various experimental and numerical studies during boiling and drop impingement have reported a significant local heat transfer near the three-phase contact line. This is attributed to the small thermal resistance across the liquid layer due to its small thickness in this region. If the wall is superheated, the small thermal resistance leads to an extremely large heat flux as the temperature at the liquid–vapor interface is fixed to local saturation temperature in equilibrium.

Potash and Wayner [108] introduced a concept by which no actual contact line is specified on a microscopic scale. Their concept was originally developed for perfectly wetting liquids. As depicted in Fig. 4.1, they suggested that the apparent dry region of the wall near the contact line is covered with a thin adsorbed film of liquid molecules, having a thickness of the order of few nanometers. The liquid molecules within this layer are adsorbed to the solid wall due to the action of intermolecular dispersion forces, which follow from van der Waals interaction forces. Due to the action of this force, the fluid pressure near the wall either increases when the force is attractive or decreases when the force is repulsive. This pressure change is termed "disjoining pressure". No evaporation occurs in this region because of strong attractive forces between fluid and wall.

The transition region between adsorbed layer and the macro region is referred to as "micro region" (see Fig. 4.1). This region is characterized by a sharp maximum in the curvature of the liquid–vapor interface. There are three main aspects distinguishing the heat transfer in the micro region from the macro region:

- Intermolecular attraction forces between fluid and wall molecules must be taken into account in this region due to its small length scale. However, this can be neglected on the macroscopic scale.
- The high values of the curvature leads to a pressure jump across the liquid–vapor interface resulting in a strong deviation of the local vapor pressure, and, accordingly, saturation temperature from the pressure and saturation temperature in the macroscopic domain.

Hence, the curvature and the attraction forces change the local thermodynamic equilibrium in this region.

- The interfacial thermal resistance, which can be negligible on the macroscopic scale, must be taken into account when describing the heat transfer in the micro region.

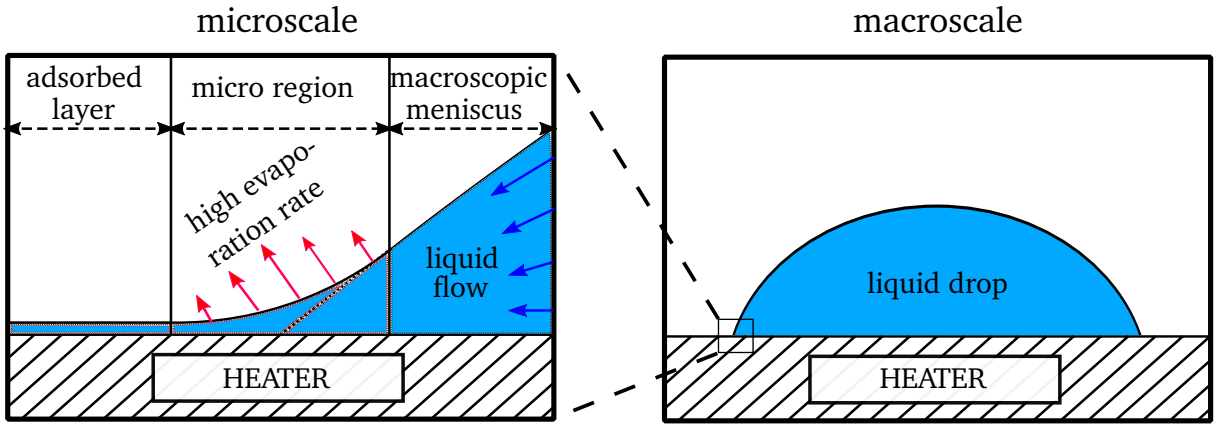

Figure 4.1.: Sketch of a liquid drop (macroscale) and the three-phase contact line (microscale).

It is difficult to experimentally validate the micro region models since the measurements of physical quantities within this region are complex due to their short time and small length scales. However, various studies reported that macroscopic characteristics of an evaporating contact line are qualitatively correct if a micro region model is employed.

The employed model in this work, which is used to describe the heat and mass transfer at the three-phase contact line, was initially proposed and used by Stephan and Busse [109] and later was developed by [38, 110–112]. In the recent model developed by Batzdorf [2], the effects of the contact line motion and the recoil pressure were included. More details can be found in [2].

The micro region model is solved independently from the macro scale model. The input variables in this model are the contact line velocity, and wall superheat, whereas, the output variables are apparent contact angle and local heat flux at the three-phase contact line. A correlation is fitted to the results of the micro region model and implemented in the macro simulations in order to save computational time.

4.2 Macro scale heat and fluid flow

To model heat and fluid flow within the macro region, conservation equations for mass, momentum, energy, and volume fraction should be solved. The mass equation reads

$$\nabla \cdot \mathbf{u} = \Sigma_V \,, \tag{4.1}$$

where Σ_V is the volume change in case of phase change due to the density difference between the two phases. Cauchy's equation of motion is

$$\rho\left(\frac{\partial \mathbf{u}}{\partial t} + (\mathbf{u}\cdot\nabla\mathbf{u})\right) = \nabla\cdot\mathbf{T} + \rho\mathbf{g} + \mathbf{f}_\sigma \,. \tag{4.2}$$

The last two terms on the right-hand side of equation 4.2 include the effects of the gravity and surface tension, and **T** is the stress tensor. Since both liquid and vapor phases are considered as Newtonian fluids, the stress tensor can be expressed as

$$\mathbf{T} = -\left[P + \frac{2}{3}\mu(\nabla \cdot \mathbf{u})\right]\mathbf{I} + \mu\left[\nabla\mathbf{u} + (\nabla\mathbf{u})^T\right]. \tag{4.3}$$

According to Fourier's law, the reformulated energy conservation in form of temperature is

$$\frac{\partial(\rho c T)}{\partial t} + \nabla \cdot (\rho c \mathbf{u} T) = \nabla \cdot (\lambda \nabla T) + \Sigma_{\mathrm{e}}\,, \tag{4.4}$$

In this equation, the pressure work and dissipation effects are neglected. The source term Σ_e accounts for the latent heat of vaporization. The energy equation within the solid phase is

$$\frac{\partial(\rho c T)}{\partial t} = \nabla \cdot (\lambda \nabla T)\,. \tag{4.5}$$

The surface tension effects shown in equation 4.2 can be calculated via

$$\mathbf{f}_\sigma = \sigma\kappa\nabla F\,, \tag{4.6}$$

where F denotes the volume fraction and κ denotes the interfacial mean curvature. It reflects if the entire cell is occupied by the liquid phase ($F = 1$) or vapor phase ($F = 0$) and is defined as

$$F = \frac{V_{\mathrm{l}}}{V_{\mathrm{c}}}\,. \tag{4.7}$$

In order to track the interface, the Volume of Fluid method proposed by Hirt and Nichols [113] is implemented. Within this method, the interface is located where the value of F is between 0 and 1. The conservation of the volume fraction is also solved by

$$\frac{\partial F}{\partial t} + \nabla \cdot (\mathbf{u}F) + \nabla \cdot (c_{\mathrm{F}} \mid \mathbf{u} \mid \mathbf{n}_{\mathrm{int}}(1-F)F) = \Sigma_{\mathrm{V}} F\,, \tag{4.8}$$

where $\mathbf{n}_{\mathrm{int}}$ denotes the unit normal vector of the interface and c_{F} denotes the numerical factor, which influences the strength of the compression, which is set to unity in this work.

The evaporation model developed by Kunkelmann and Stephan [33] is further added to the set of above mentioned equations. In this model, the temperature at the liquid–vapor interface is assumed to be equivalent to the saturation temperature of the fluid, which corresponds to the system pressure. The evaporation heat flux at the interface is calculated by the temperature gradient normal to the interface on the liquid and vapor side, respectively. The macroscopic model is implemented into the open source CFD software OpenFOAM. For discretization of the conservation equations, the Finite Volume Method is utilized. More details of macroscopic model can be found in [2].

5 Results and Discussion

The present chapter is divided into the results corresponding to the impingement of a single drop (section 5.1) and multiple drops (section 5.2) onto a heated surface. Within each section, the influence of relevant parameters on hydrodynamics and heat transport during the drop impingement is presented.

5.1 Single drop impingement

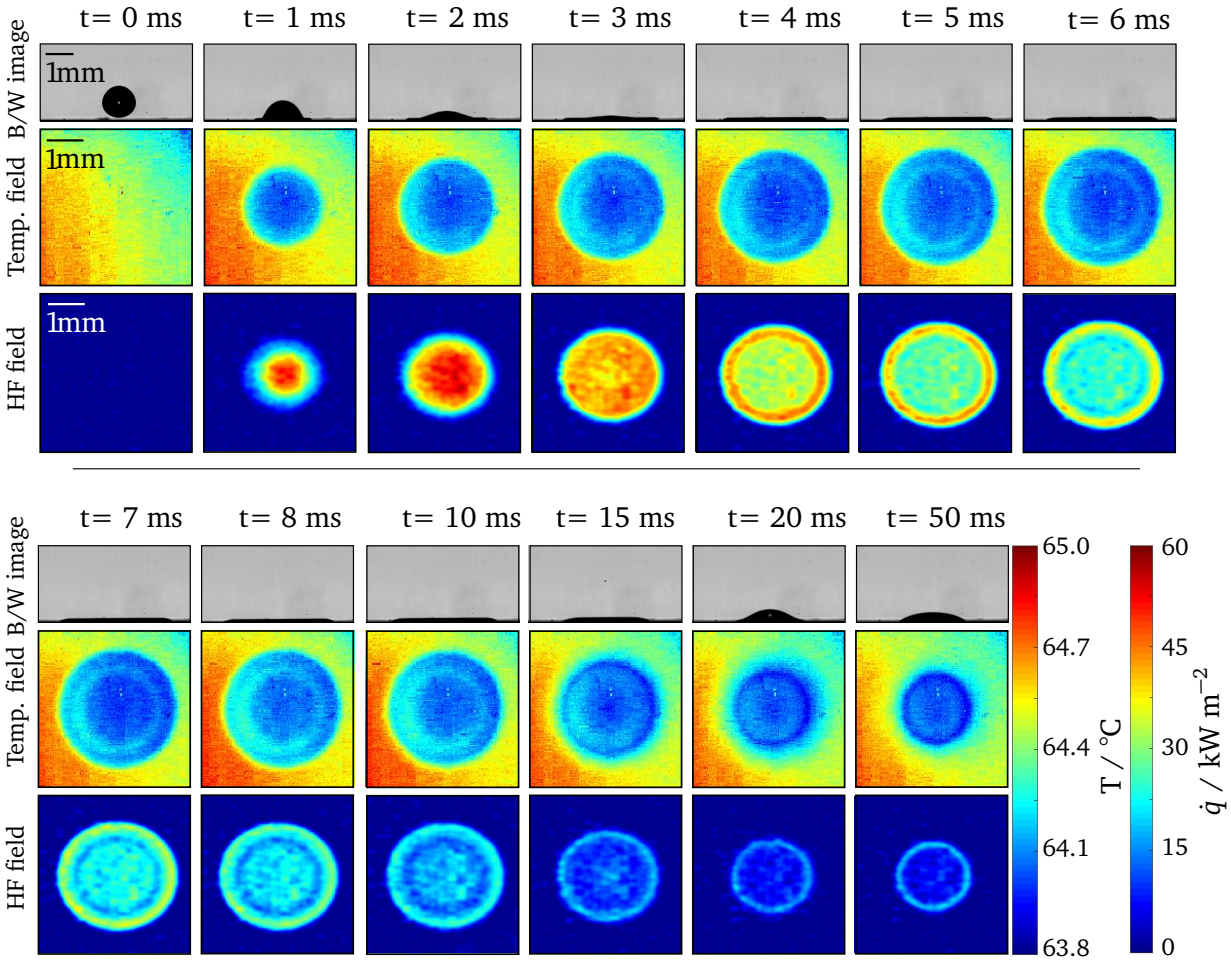

Figure 5.1.: B/W images, temperature and heat flux fields during the impingement of a single drop onto a bare heater for 50 ms after impact ($D_0 = 0.93$ mm, $u_0 = 0.44$ m s^{-1}, $\Delta T = 9.5$ K, p= 0.9 bar, Re= 1450, We= 34, Bo= 0.4, Ja= 0.13, Pr= 9.7, and $p_R = 0.05$).

This section addresses the influence of wall superheat, impact velocity, drop size, system pressure, and surface structure on hydrodynamics and heat transport during single drop impingement onto moderately superheated surfaces. The side-view of the drop shape evolution captured by the B/W camera and temporal evolution of the temperature and heat flux distribution at the

fluid–solid interface determined from the IR images are presented in Fig. 5.1. One can notice that the heater surface is colder at the drop footprint. High local heat flux is transferred to the liquid during the first few milliseconds when the drop wets the heater surface. At the early stages of impact, the highest heat flux is transferred through the center of the drop footprint. At this stage, the heat flux is uniform at the center and reduces radially outwards, so that it is the lowest in the proximity of the three-phase contact line. At t = 4 ms, before the drop reaches its maximum radius, high local heat flux near the three-phase contact line is observed. The radius of the contact line reaches its maximum, and the heat flux at the center of the drop footprint reduces gradually. Since then, the heat flux in the proximity of the contact line is larger than that at the center, indicating the high rate of evaporation in this region. Qualitatively similar behavior of the heat flux distribution has been observed in the whole parameter ranges.

i. Hydrodynamic behavior

Figure 5.2a compares the corresponding numerical and experimental results for contact line radius for the example depicted in Fig. 5.1. As demonstrated, the drop impingement event is subdivided into three subsequent phases: i) the drop spreading phase, ii) the drop receding phase, and iii) the sessile drop evaporation phase. During the drop spreading phase, the liquid motion is dominated by inertia forces, and the contact line moves radially outwards. This process ends as soon as the contact line reaches its maximum due to the dissipation of kinetic energy. In the receding phase, the contact line starts to shrink. The surface tension is the driving force in this phase, which tends to minimize the surface area of the liquid. Since the kinetic energy rises, the contact line radius, R_{cl}, may reach a smaller value than that corresponding to equilibrium form. The contact line moves again outward, and this oscillation phenomenon could be repeated several times until the drop reaches the equilibrium state corresponding to the sessile drop evaporation phase.

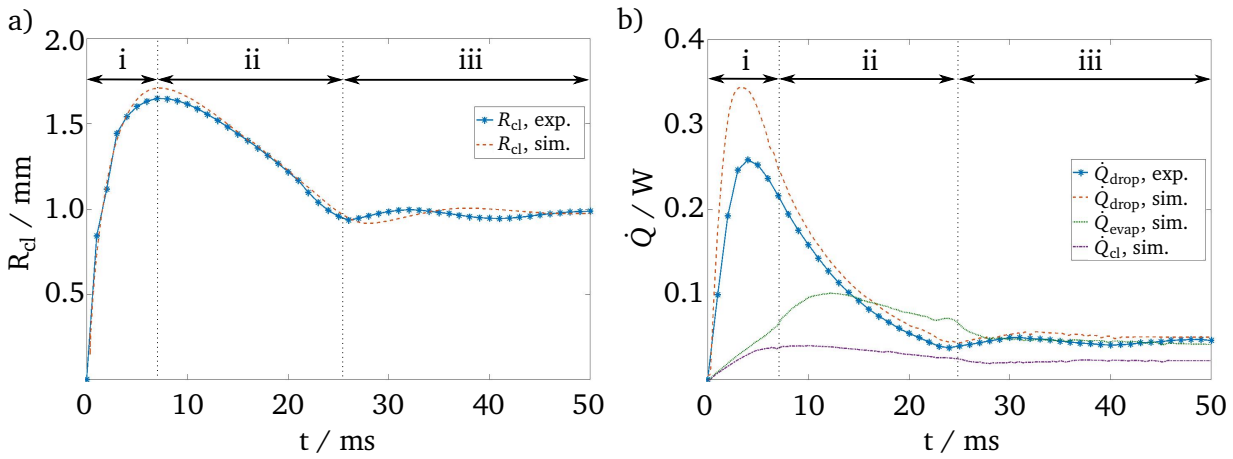

Figure 5.2.: Temporal evolution of the a) contact line radius and b) heat flow during the impingement of a single drop onto a bare heater evaluated from experimental data and predicted from numerical simulations ($D_0 = 0.93$ mm, $u_0 = 0.44$ m s^{-1}, $\Delta T = 9.5$ K, and p= 0.9 bar).

ii. Heat transfer behavior

Figure 5.2b depicts the numerical and experimental results for heat flow evolution, for the example shown in Fig. 5.1. In this figure, the global heat flow, $\dot{Q}_{drop}$, is defined as the heat

transferred to the drop at the liquid–solid interface. The temporal evolution of the heat flow corresponding to the evaporation, $\dot{Q}_{\text{evap}}$, and the proportion of the heat transferred in the circular region of 10 μm around the contact line position (from where the reconstructed interface intersects the wall into the liquid bulk), $\dot{Q}_{\text{cl}}$, are evaluated numerically and illustrated in this figure, as well.

During the three phases following the drop impact, the heat is transferred by conduction, convection, and evaporation. However, the contribution of each heat transfer mechanism differs during different phases. The driving heat transfer mechanism during the spreading phase is mainly convection from the wall to the drop. This phase is characterized by a fast increase in heat flow because of the increasing contact area between the cold liquid and the hot dry wall. The maximum heat flow is transferred to the drop during this phase before the contact line radius reaches its maximum. As the fluid motion slows down and the temperature difference between the liquid and the wall reduces, the heat flow decreases despite the enlargement of the contact line radius. During the receding phase, the motion direction reverses, and the superheated liquid is transported from the superheated thermal boundary layer towards the liquid–vapor interface. This eases the evaporation at the liquid–vapor interface. In this phase, the global heat flow reduces continuously until it reaches its minimum. During the sessile drop evaporation phase, the heat transport takes place mainly by evaporation. As shown in Fig. 5.2b, around 50% of total heat flow is transferred in the proximity of the three-phase contact line. A summary of the dominating heat transfer mechanisms for each phase of the impingement is presented in [2].

Unlike in numerical simulations, it is not possible to distinguish between evaporation, conduction, and convection heat transfer during experiments. But the numerical results presented in [2, 24, 25] and in the present work allow good predictions with respect to the behavior of the evaporation heat transfer for experimental results. It can be seen in Fig. 5.2b that the contribution of evaporation to the total heat transfer rate is low during the drop spreading phase (i) and its relative influence increases continuously during the receding phase (ii). During the sessile drop evaporation phase (iii), the total heat is transported mainly by evaporation, and the evaporation in the proximity of the three-phase contact line contributes around half of the total heat flow. Therefore, the influence of the experimental parameters on the heat transfer rate during the sessile drop phase, which is reported in the following sections reflects the influence of these parameters on evaporation heat transfer.

5.1.1 Influence of wall superheat

The experimental results and numerical simulations on the influence of wall superheat ranging from 6.9 to 17.2 K on the contact line radius and the heat flow are shown in Figs. 5.3a and b, respectively. As can be observed in Fig. 5.3a, increasing wall superheat leads to a decrease of the maximum contact line radius, the spreading and the receding durations, and also leads to a slightly faster drop receding phase. This behavior can be mainly attributed to the higher evaporation rate in the proximity of the three-phase contact line, particularly during the receding and sessile drop evaporation phases, and concomitant higher apparent contact angle [38]. The larger wall superheat is accompanied by a stronger oscillation of the drop at the end of the receding phase and results in the formation of smaller drops during the sessile drop evaporation phase. A good qualitative and quantitative agreement between the experimental data and numerical simulations is observed.

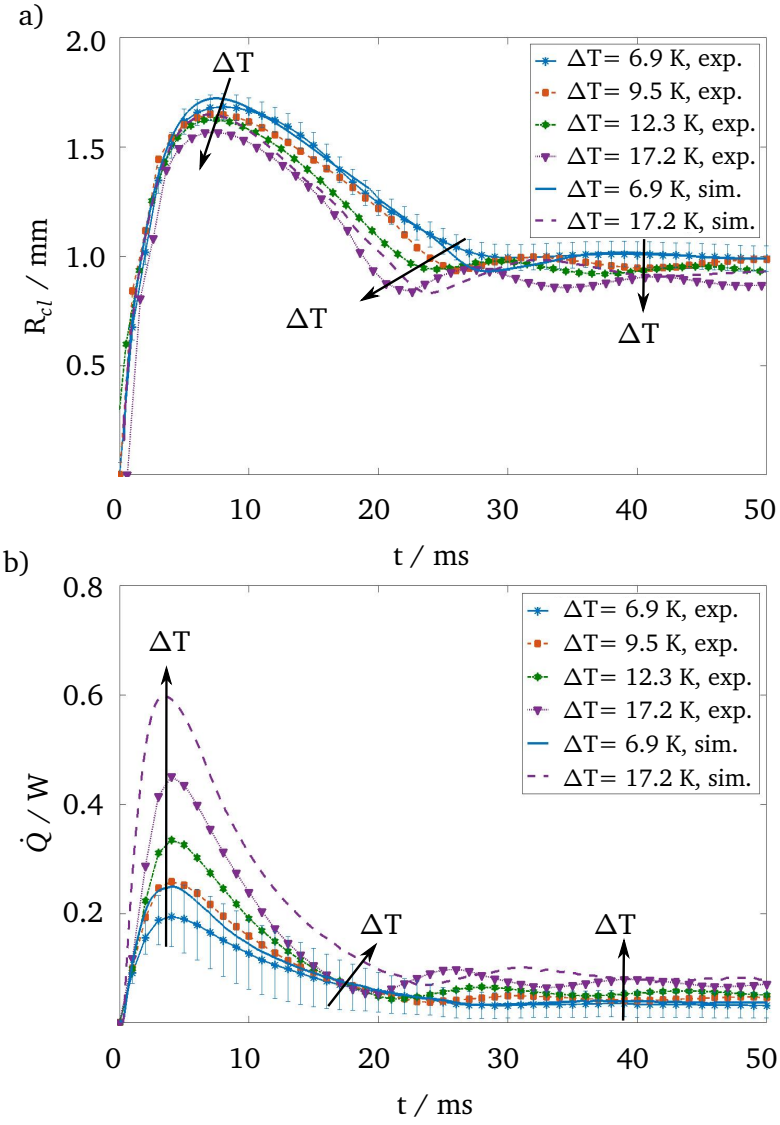

Figure 5.3.: Temporal evolution of the a) contact line radius and b) heat flow during the impingement of a single drop onto a bare heater for various wall superheats ($D_0 = 0.93$ mm, $u_0 = 0.44$ m s^{-1}, and p= 0.9 bar).

As depicted in Fig. 5.3b, an increase in the wall superheat enhances the heat flow. However, this enhancement is weaker than linear due to the decrease of liquid–solid contact area when increasing the wall superheat. Similar to the contact line radius, an oscillation in global heat flow at the end of the receding phase is observed. During the sessile drop evaporation phase, the larger wall superheat induces a higher heat flow. Since the temperature difference between the heater surface and the liquid drop is larger at higher wall superheats, the evaporation rate is predicted to be larger, as well. To improve the readability of the graphs, the error bars of only one measurement ($\Delta T = 6.3$ K) is indicated.

As depicted in Figs. 5.3a and b, a good qualitative agreement between the experimental and simulation data is observed. The deviation between the measured and numerically predicted heat flux can be attributed to the lower spatial resolution of the IR camera compared to the three-phase contact line. The size of the three-phase contact line is approximately one micrometer [2].

However, the spatial resolution of the IR camera, as already mentioned, is 29.27 μm/pixel. This hinders the precise detection of the expected high-temperature gradient in this region.

Figures 5.4a and b represent the spreading ratio and dimensionless heat flow versus dimensionless time for various Ja numbers. The spreading ratio is independent of the wall superheat at the initial stages of the impact. The maximum spreading ratio decreases, while the maximum dimensionless heat flow rises at larger wall superheats. The demonstrated behavior of the spreading ratio and dimensionless heat flow dependent upon the Ja number is in line with the numerical work of Batzdorf [2].

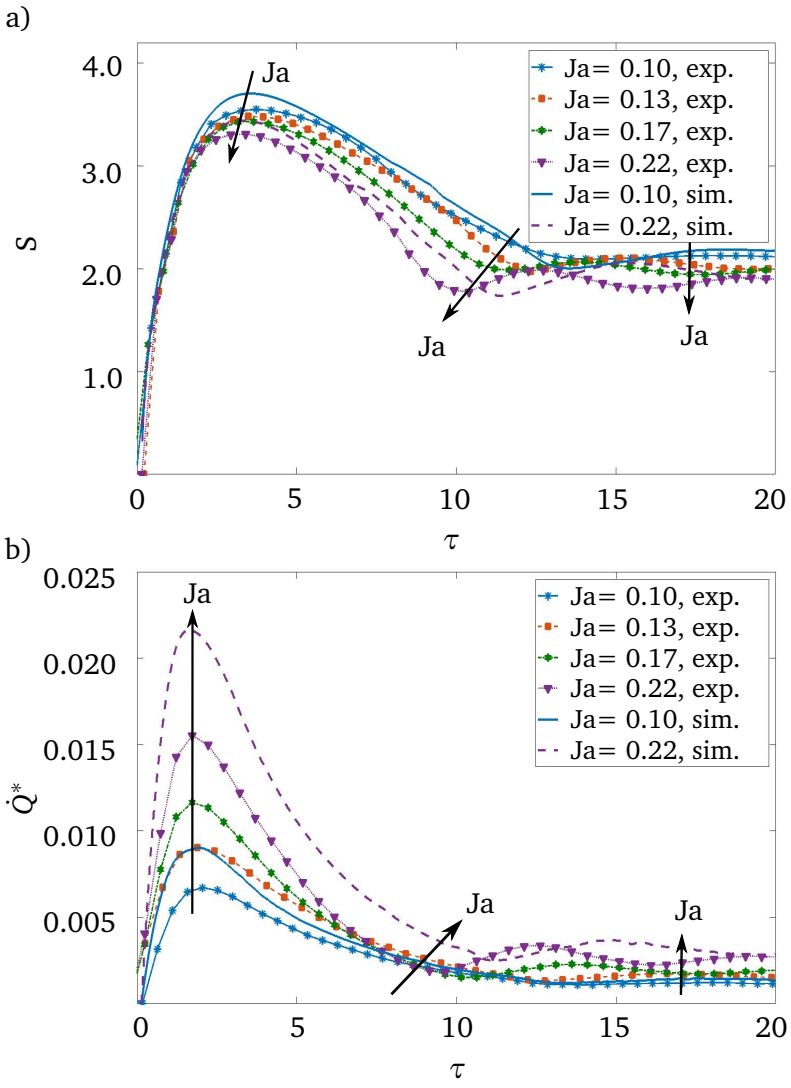

Figure 5.4.: a) Spreading ratio and b) dimensionless heat flow versus dimensionless time during the impingement of a single drop onto a bare heater for various Ja numbers (Re= 1450, We= 34, Bo= 0.4, Pr= 9.7, and $p_R = 0.05$).

The corresponding dimensional and dimensionless cumulative heat flow for the aforementioned measurements are depicted in Figs. 5.5a and b. Both dimensional and dimensionless cumulative heat flow rise sharply during the spreading and receding phases since high heat is transported to the liquid. A moderate increase in cumulative heat flow during the sessile drop evaporation phase is measured since the heat flow is lower than in the first two phases.

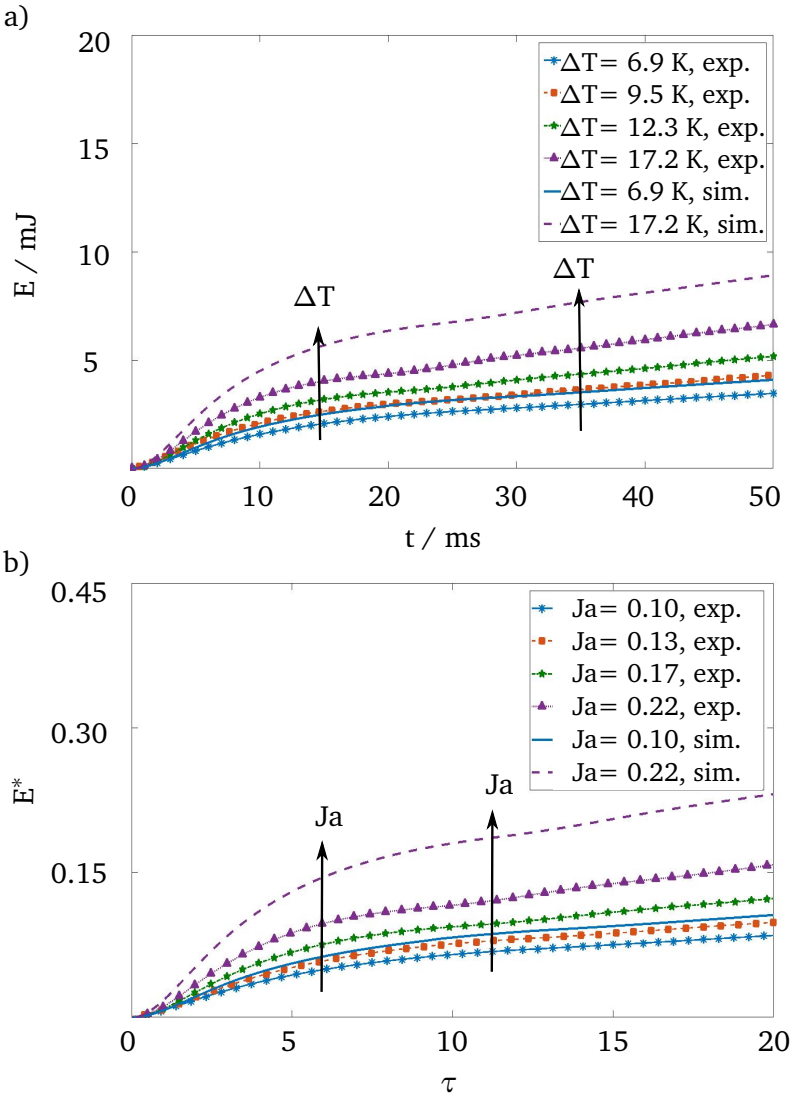

Figure 5.5.: Temporal evolution of the cumulative heat flow in a) dimensional and b) dimensionless forms during the impingement of a single drop onto a bare heater for various wall superheats ($D_0 = 0.93$ mm, $u_0 = 0.44$ m s^{-1}, p= 0.9 bar, Re= 1450, We= 34, Bo= 0.4, Pr= 9.7, and $p_R = 0.05$).

5.1.2 Influence of impact velocity

Figures 5.6a and b depict the experimental data and the results of numerical simulations of the contact line radius and heat flow for various impact velocities ranging from 0.33 to 0.57 m s^{-1}, respectively. It is observed that larger impact velocities and consequently spreading velocities and kinetic energies lead to a shorter duration of spreading phase and a larger maximum contact line radius (see Fig. 5.6a). The maximum contact line radius is larger for faster drop impacts because of higher kinetic energy.

According to the work of Herbert et al. [24], the maximum contact line radius increases with impact velocity not linearly ($R_{\mathrm{cl,max}} \propto u_0^{0.2}$). This is in good agreement with these experimental results, where $R_{\mathrm{cl,max}} \propto u_0^{0.208}$. The increase of the impact velocity prolongs the receding phase. During the sessile drop evaporation phase, the contact line radii reach almost the same equilibrium state independently from the impact velocity, since the alteration in impact velocity

only influences the inertia forces dominating during the spreading phase. However, the drop is in a stationary condition during the sessile drop evaporation phase, and inertia forces do not play any role, resulting in a similar drop footprint independent of the impact velocity.

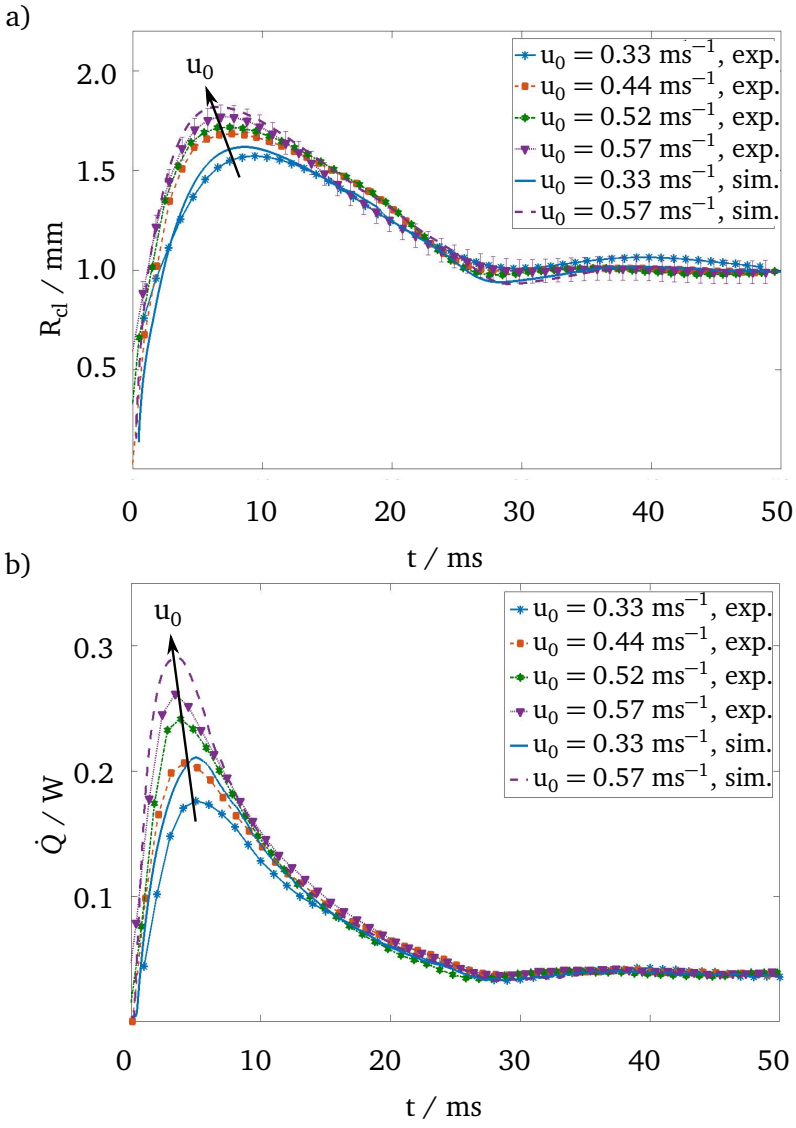

Figure 5.6.: Temporal evolution of the a) contact line radius and b) heat flow during the impingement of a single drop onto a bare heater for various impact velocities ($D_0 = 0.93$ mm, $\Delta T = 6.3$ K, and p$= 0.9$ bar).

During the advancing phase, the global heat flow follows the hydrodynamic trend and reaches its maximum earlier with increasing impact velocity (see Fig. 5.6b). Higher impact velocity leads to higher heat flow during both advancing and receding phases. Moreover, the influence of impact velocity on heat flow is stronger than maximal contact line radius. Finally, after almost 28 ms, the drop reaches its equilibrium, leading to identical heat flows for various impact velocities. Experimental and simulation data are in good qualitative and quantitative agreement. The drop evaporation is predicted to be independent of the impact velocity. This is attributed to the almost similar contact line radii during the receding and sessile drop evaporation phases.

Figures 5.7a and b depict the influence of impact velocity on hydrodynamics and heat transfer in dimensionless form. Variation in impact velocity leads to simultaneous alteration of Re and We

numbers. It is clearly visible that an increase of both Re and We numbers shift the maximum contact line radius and the maximum dimensionless heat flow to the higher dimensionless time. The maximum spreading ratio expands while the maximum dimensionless heat flow reduces. These trends for the spreading ratio and dimensionless heat flow are in line with the numerical work of Herbert et al. [24]. They have shown that the Reynolds number exerts a much stronger influence on the maximum spreading ratio; however, the We number affects mainly the receding phase. It is, in addition, very important to note that the final spreading ratio is approximately equal to two, independent of the impact velocity. On the one hand, this is because the apparent contact angle does not depend on the impact velocity. On the other hand, the volume change of the drop is small due to the evaporation in this short time. As depicted in Fig. 5.7a, the spreading ratio is independent of the impact velocity at the initial stages of impact.

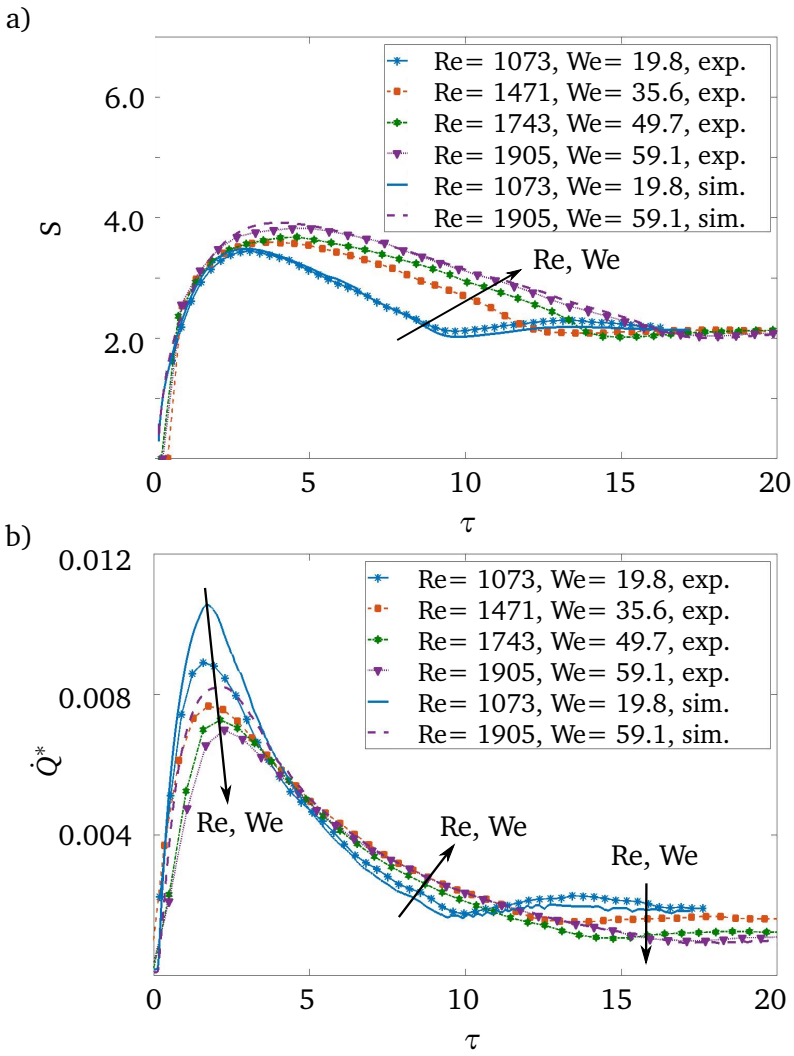

Figure 5.7.: a) Spreading ratio and b) dimensionless heat flow versus dimensionless time during the impingement of a single drop onto a bare heater for simultaneous variations of Re and We numbers (Ja= 0.08, Bo= 0.4, and Pr= 9.7 and $p_R = 0.05$).

In Annex A.4.1, the corresponding dimensional and dimensionless cumulative heat flow for the above measurements are depicted.

5.1.3 Influence of drop size

The experimental results and numerical simulations of the contact line radius and heat flow for different drop sizes ranging from 0.97 to 1.60 mm are depicted in Figs. 5.8a and b, respectively. In order to fit the largest drop in the field of view of the IR camera, the spatial resolution of the IR camera is set to a low resolution of 40.82 μm/pixel. This reduces the accuracy of the measurements and leads to the deviation between experimental and simulated curves. The measurement accuracy near the maximum contact line radius is even lower in the case of the largest drop ($D_0 = 1.60$ mm). It is attributed to the defective pixels of the camera chip near the corners of the IR camera's FOV. This resulted in the discrepancy between measured and simulated contact line radius and heat flow in case of $D_0 = 1.60$ mm.

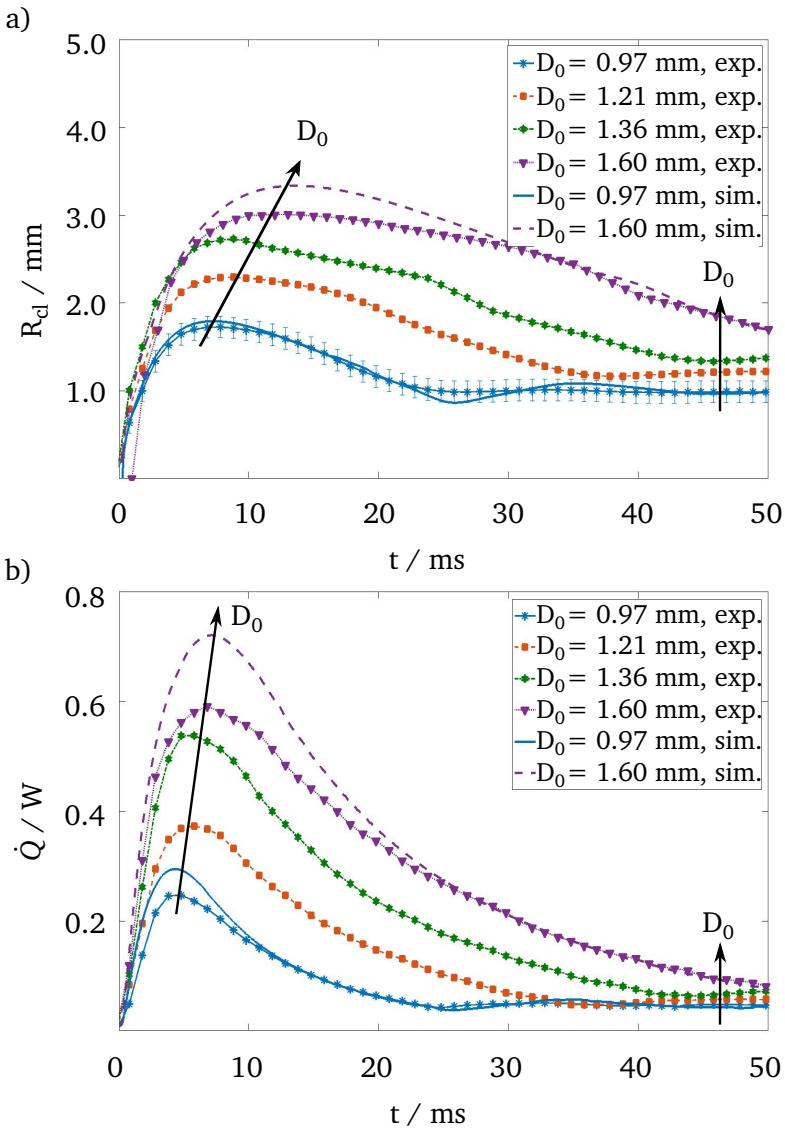

Figure 5.8.: Temporal evolution of the a) contact line radius and b) heat flow during the impingement of a single drop onto a bare heater for various impact diameters ($u_0 = 0.44$ m s^{-1}, $\Delta T = 6.9$ K, and p= 0.9 bar).

It can be observed that the impact of larger drops is accompanied by the prolongation of the drop spreading and receding phases (see Fig. 5.8a). Furthermore, the maximum contact line

radius increases with increasing the drop diameter. As intuitively expected, bigger drops deliver larger heat flow, since the wetted surface becomes larger (see Fig. 5.8b). The heat flow follows the identical trend as the contact line radius. Additionally, higher drop evaporation due to larger drop footprints can be observed for bigger drops.

Figures 5.9a and b show the influence of drop size on hydrodynamics and heat transfer in dimensionless form. Drop size alteration causes simultaneous variation in Re, We, and Bo numbers. In the range of measurement drop sizes, if Re, We, and Bo increase, the maximum spreading ratio slightly increases and shifts to larger dimensionless time. It can be noticed that the final spreading ratio is independent of the drop size and is approximately equal to two. It can be concluded that the spreading ratio during the sessile drop evaporation is independent of the impact parameters while marginally depending on the Ja number. This is an important result that allows modeling the sessile drop evaporation starting from this moment. The maximum of dimensionless heat flow reduces and occurs at a constant dimensionless time of approximately 2. In Annex A.4.1, the corresponding dimensional and dimensionless cumulative heat flow for the aforementioned measurements are presented.

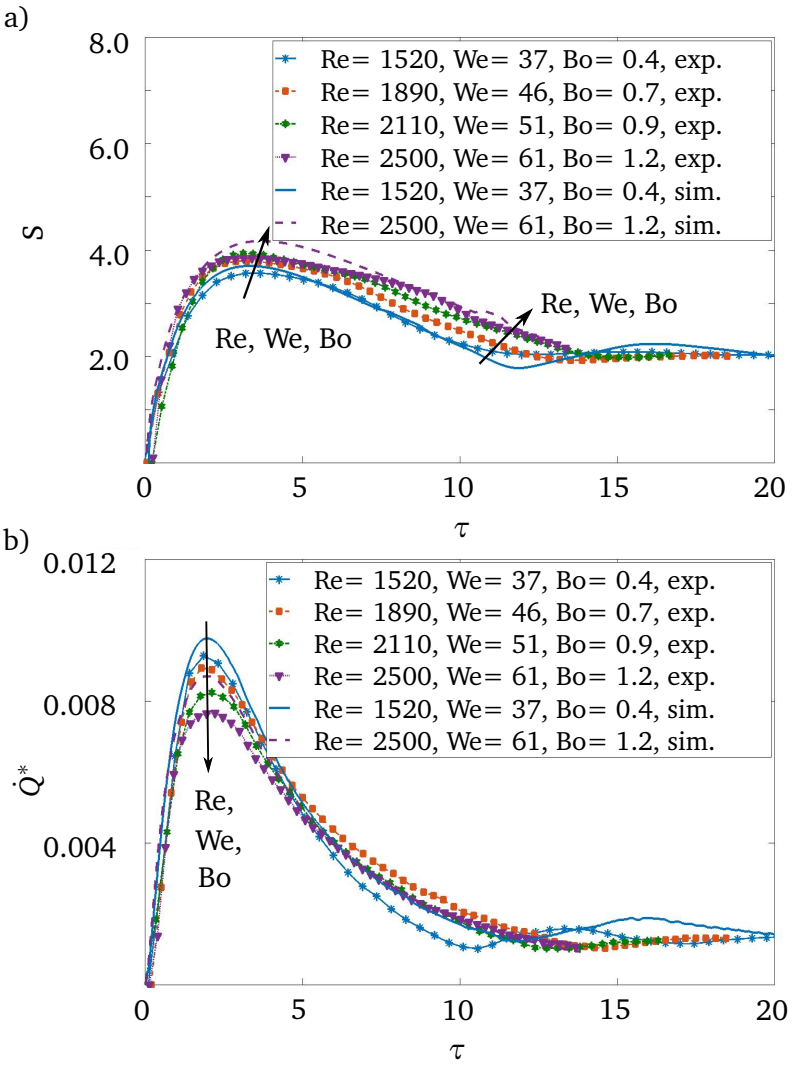

Figure 5.9.: a) Spreading ratio and b) dimensionless heat flow versus dimensionless time during the impingement of a single drop onto a bare heater for simultaneous variations of Re, We, and Bo numbers (Ja= 0.08, Pr= 9.7, and $p_R = 0.05$).

5.1.4 Influence of system pressure

Figures 5.10a and b present the temporal evolution of the contact line radius and heat flow for various reduced pressures ranging from 0.05 to 0.5, respectively. In systems with pressure variations reduced pressure, p_R, is normally used, which is defined as the ratio of actual pressure, p, and critical pressure, p_{crit},

$$p_R = \frac{p}{p_{crit}} . \tag{5.1}$$

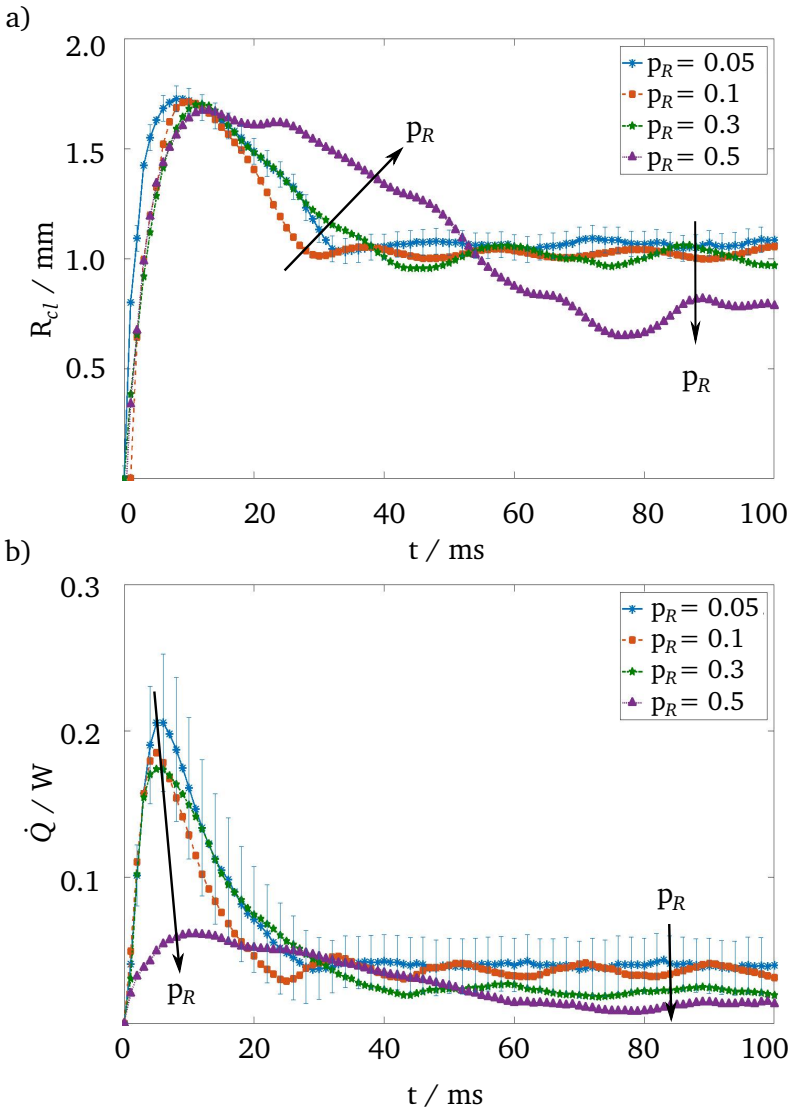

Figure 5.10.: Temporal evolution of the a) contact line radius and b) heat flow during the impingement of a single drop onto a bare heater for various system pressures ($D_0 = 0.94$ mm, $u_0 = 0.34$ m s^{-1}, and $\Delta T = 6.5$ K).

As depicted in Fig. 5.10a, the maximum of the contact line radius is approximately similar in all four pressures. However, the duration of the spreading and particularly receding phases is increased at elevated pressures. This is attributed to the slight decline of kinetic energy due to the lower liquid density, to the a significant decrease of liquid surface tension by increasing the cell pressure. The minimum contact line radius at the end of the receding phase appears at a

later time and becomes smaller at higher cell pressures. Moreover, the drop footprint during the sessile drop evaporation phase becomes smaller at elevated pressures. This behavior of the contact line radius agrees qualitatively with the results of the numerical work of Schlawitschek [68].

According to Fig. 5.10b, the heat flow is reduced at elevated pressures mainly due to the reduction in heat flux caused by low liquid thermal effusivity. The thermal effusivity of a material is a measure of its ability to exchange thermal energy with its surroundings and is defined as the square root of the product of the material's thermal conductivity and its volumetric heat capacity. The thermal effusivity of FC-72 reduces from 305 W $s^{0.5}$ m^{-2} K^{-1} at $p_R = 0.05$ to 250 W $s^{0.5}$ m^{-2} K^{-1} at $p_R = 0.5$. This strongly reduces the maximum heat flow at high pressures. Besides, an increase in system pressure is accompanied by lower heat flow during the sessile drop evaporation phase, in which evaporation is the main heat transport mechanism. This can be explained by a decrease in latent heat of vaporization at elevated pressures. This behavior of heat flow at elevated pressures are in line with the results addressed in the work of Schlawitschek [68].

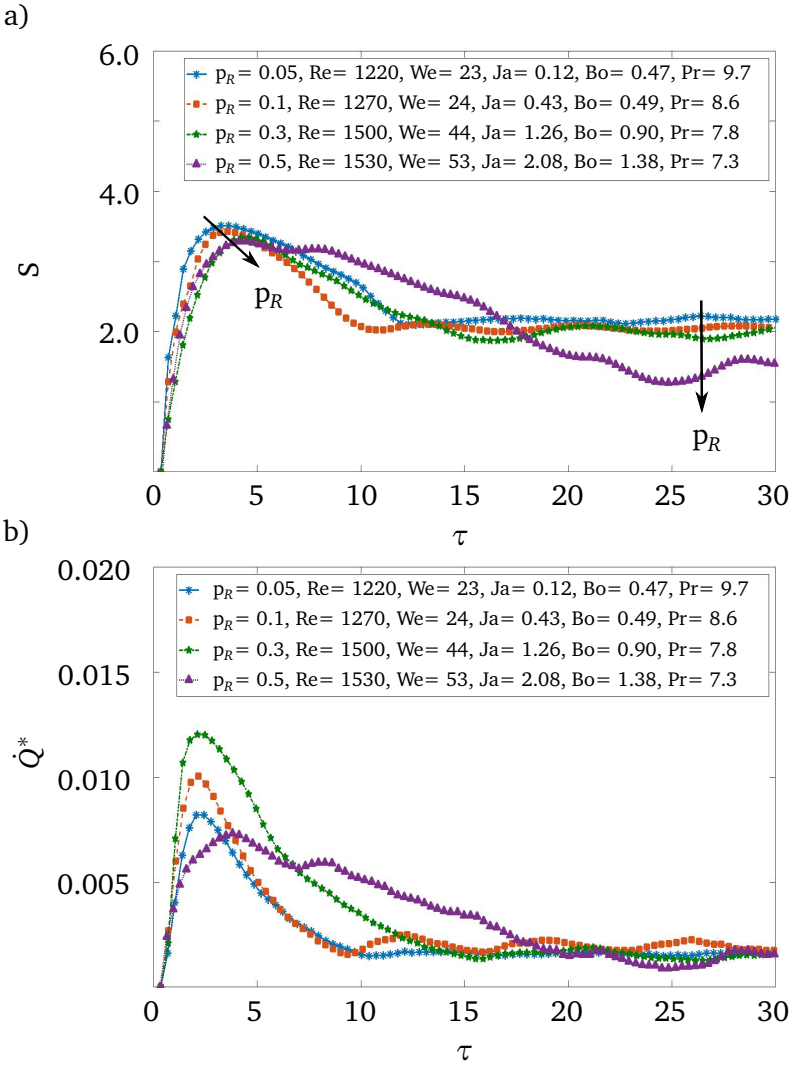

Figure 5.11.: a) Spreading ratio and b) dimensionless heat flow versus dimensionless time during the impingement of a single drop onto a bare heater for simultaneous variations of Re, We, Bo, Ja, Pr, and p_R.

Figures 5.11a and b show the influence of system pressure on hydrodynamics and heat transfer in dimensionless form. If the system pressure rises, the Re, We, Ja, and Bo numbers become larger, while the Pr number declines. In the range of studied system pressures, the spreading ratio follows the same trend as the contact line radius. However, a consistent behavior cannot be recognized during the spreading and receding phases. But the dimensionless heat flow during the sessile drop evaporation phase reaches a constant value of 0.002, which is independent of the system pressure. As already explained, evaporation is the primary heat transport mechanism during the sessile drop evaporation phase. Therefore, constant value of dimensionless heat flow in this phase suggests a proportional relationship between the evaporation and the product of latent heat and density for this parameter range (see equation 2.11).

The corresponding dimensional and dimensionless cumulative heat flow for the aforementioned measurements are depicted in Annex A.4.1.

5.1.5 Influence of surface structure

This section is devoted to the influence of the porous coating on hydrodynamics and heat transport during single drop impact. To create a porous coating, the heater substrate was coated with a nanofiber mat consisting of randomly oriented nanofibers generated through electrospinning of 5 wt% polyacrylonitrile solution (PAN; M_w = 150 kDa) in N,N-dimethylformamide (DMF). In this section, the influence of wall superheat and drop impact velocity in the presence of nanofiber mat, as well as the influence of mat thickness on the hydrodynamics and heat transport during single drop impact, are addressed.

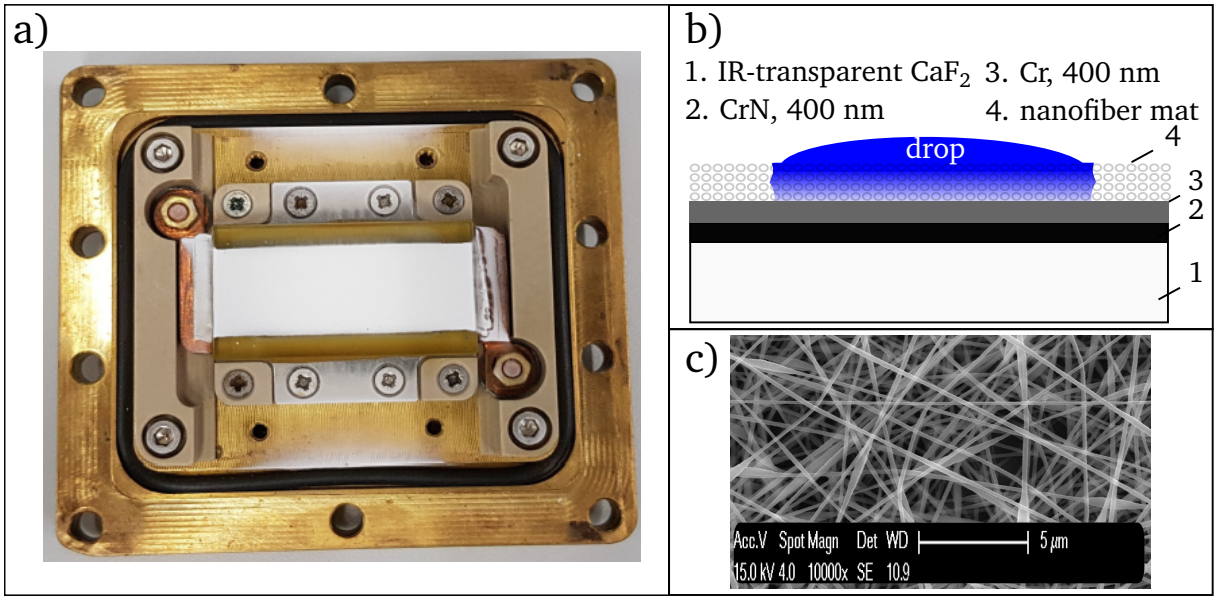

Figure 5.12.: a) Image of the heater flange consisting of the heater substrate coated with nanofiber mat, b) schematic of the heater coated with nanofiber mat, and c) SEM image of the nanofiber mat.

The electrospinning setup from Avectas Spraybase is used in this study. More details of electrospinning setup and process are given in the work of Heinz et al. [114]. To generate fibers, a polymer solution is subjected to an electric field by pumping the solution through an emitter.

A Taylor cone at the tip of the emitter is formed due to the electric field. The electric field leads to the acceleration of a jet of polymer solution towards the collector. The simultaneous occurrence of hydrodynamic and electrostatic instabilities perturbs and deforms the polymer jet. It influences the final morphology of the fibers. The emitter is typically a stainless steel needle connected to a high voltage potential, while the collector is grounded. In this study, the heater described in Section 3.4 is used as the collector.

Figure 5.12a and b show the captured image from the heater flange consisting of the heater substrate coated with nanofiber mat, and the schematic of the coated heater. The SEM image of the generated nanofibers is depicted in Fig. 5.12c. The nanofibers are electrospun onto the heater substrate in particular time durations to achieve distinct mat thicknesses. Within this study, the mat thicknesses, measured using a confocal microscope, are 18, 22, 51, and 80 μm. The fiber diameters ranged from 200 to 300 nm.

The side-view of the drop shape evolution captured by the B/W camera, and the temporal evolution of heat flux distribution evaluated from the IR images in the presence and absence of nanofiber mat, are presented in Fig. 5.13. The thickness of the nanofiber mat is $h_{mat} = 22$ μm. As can be seen in this figure and already shown in Fig. 5.1, the drop impingement onto the uncovered (bare) heater is subdivided into spreading, receding, and sessile drop evaporation phases.

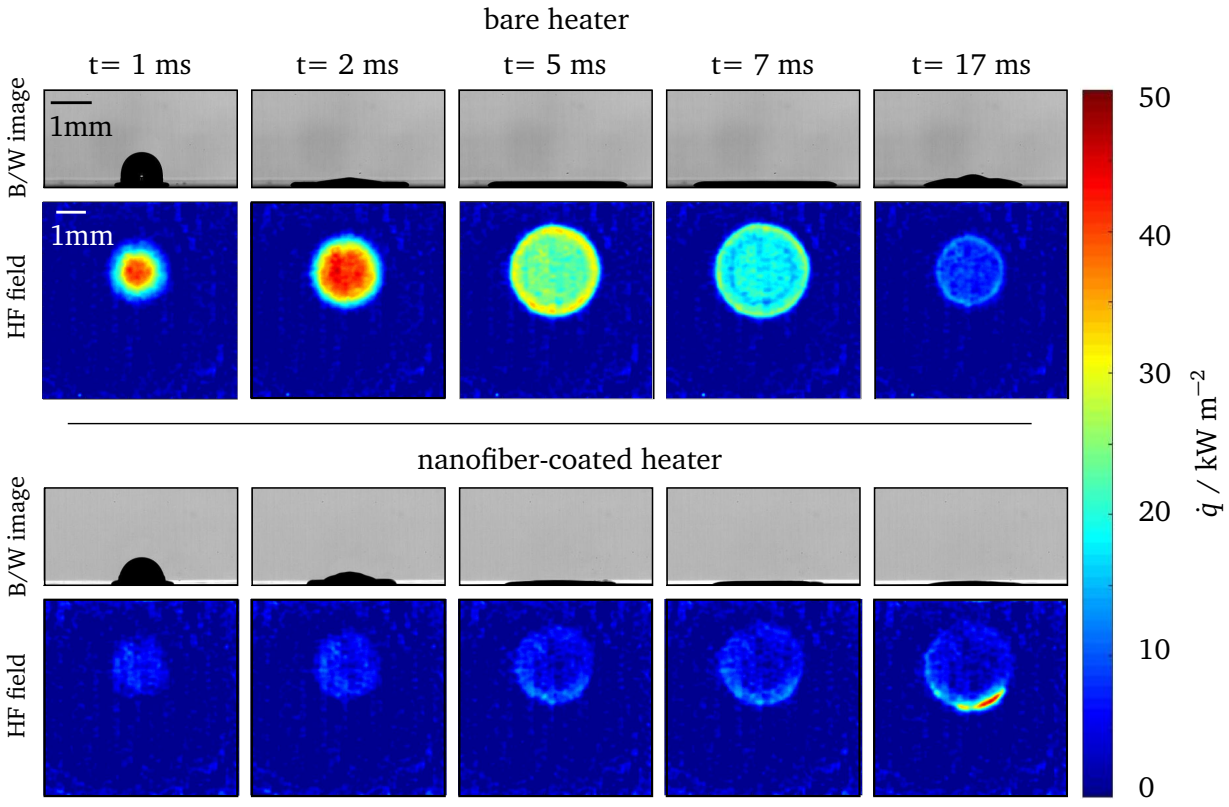

Figure 5.13.: B/W images and heat flux fields for 17 ms after the impingement of a single drop onto a bare (top), and nanofiber-coated (bottom) heater surface ($D_0 = 0.95$ mm, $u_0 = 0.45$ m s^{-1}, and $\Delta T = 14.6$ K).

Similar to the bare surfaces, the inertial force leads to drop spreading over the nanofiber mat at the initial stages of impact. However, the spreading velocity is slower than that on the uncovered

heater. Thereafter, drop spreading is impeded, the contact line is pinned, and liquid penetrates the porous nanofiber mat, which leads to the suppression of the drop receding phase for the coated heater. Finally, the liquid drop slightly shrinks, and its spreading radius moderately declines because of the phase transition from liquid to vapor.

In contrary to drop impact onto a bare heater, the presence of nanofiber mat prevents direct contact between the liquid and the heater surface at the early stage of impact. It is suggested that the cold liquid first impacts the top surface of the hot nanofiber mat and evaporates quickly. The generated vapor is trapped inside the pores between the Cr surface and bulk liquid. This phenomenon, which is attributed to the "skeletal" Leidenfrost effect, significantly weakens the heat flux because of the low thermal conductivity of the vapor [74]. In such a case, the drop first cools down the nanofibers, and heat is removed from the heater mainly through the nanofiber skeleton ($\lambda_{\text{FC-72,v}} = 0.008$ W m^{-1} K^{-1} and $\lambda_{\text{fiber}} = 0.02 - 0.05$ W m^{-1} K^{-1} [116]).

After several milliseconds, two scenarios may occur depending on the wall superheat and impact velocity. Scenario (I): the liquid drop completely penetrates the nanofiber pores and reaches the solid heater surface. This phenomenon occurs at low wall superheat or high impact velocity and results in a significant heat flux transfer through the liquid–solid interface. Scenario (II): the wall superheat is sufficiently large; hence, a significant amount of vapor is generated and trapped inside the pores, which hinders the liquid drop from reaching the heater surface. If at the same time the impact velocity is low, the low inertial force hinder the liquid drop, expelling the vapor produced inside the pores of the nanofiber mat radially outward to reach the solid surface. Therefore, the heat transport in this scenario is lower than that in scenario (I).

Figures 5.14a and b compare the heat flux field and corresponding heat flux distribution along a line passing through the center of the drop footprint at t= 50, 90, and 150 ms for the impact velocities $u_0 = 0.45$ and 0.58 m s^{-1}, where scenario (I) and (II) are realized, respectively. The comparison was made during the sessile drop evaporation phase when the effect of convection is negligible (that could affect the heat transfer at different impact velocities).

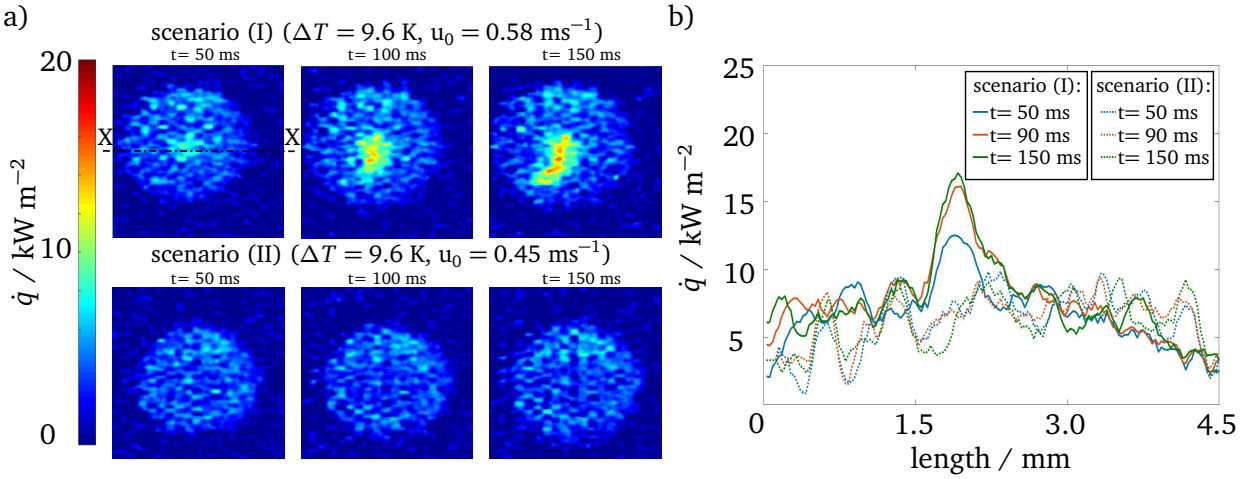

Figure 5.14.: a) Heat flux fields at t= 50, 90, and 150 ms for two scenarios: (I) (top) and (II) (bottom); b) heat flux distribution along the centreline X-X.

The measured heat fluxes depicted in the heat flux field and line suggest the penetration of liquid into the porous nanofiber mat in scenario (I), resulting in high heat flux through the liquid–solid

interface in scenario (I) compared to scenario (II). In this example, the high heat flux region in scenario (I) occurs in the middle of the impacted area; however, the position of the high heat flux can be different in other measurements and vary over time.

Figures 5.15a1, b1, and c compare the spreading radius, heat flow, and cumulative heat flow for scenario (I) and (II) for heater coated with nanofiber mat. Figures 5.15a2 and b2 are similar to a1 and b1but plotted for a shorter time period to enhance the readability of the curves. The corresponding parameters are listed in Table 5.1. For comparison, the data for drop impact on an uncovered heater surface at the same impact parameters and wall superheats are shown in the same figures. In the case of an uncovered heater, the drop spreading phase lasts a few milliseconds with a relatively large spreading velocity. Then drop receding occurs until t= 30 ms. Finally, the drop oscillates several times until it reaches its equilibrium stage.

Table 5.1.: Impact parameters and wall superheat as well as mat thickness for two exemplary drop impact experiments corresponding to scenario (I) and (II).

parameters	scenario (I)	scenario (II)
D_0 / mm	0.95	0.95
u_0 / m s^{-1}	0.58	0.45
ΔT / K	9.6	7.0
h_{mat} / μm	22	22
Re	1920	1550
We	60	39
Ja	0.12	0.09

If the heater is coated with a nanofiber mat, then the drop spreading phase can be further divided into two phases regardless of whether scenario (I) or (II) occurs: i) drop spreading with a high spreading velocity at the initial stages of impact, and ii) drop spreading with low spreading velocity thereafter. The inertial force is the governing force for the high spreading velocity phase at the initial stages of impact. In scenario (I), the spreading velocity at the early stage of impact is approximately equal to the spreading velocity on the uncovered heater. Afterward (second spreading phase), the spreading slows down compared with the uncovered heater substrate. In scenario (II), the spreading velocity is significantly lower than the spreading velocity on the uncovered heater from the very beginning. At t= 14 ms, the velocity decreases abruptly, and the second spreading phase begins but is not completed after 250 ms. The drop spreading with low spreading velocity is due to the imbibition of the drop through the pores of nanofiber mat [117].

If scenario (I) occurs, then the spreading radius reaches a larger maximum compared with the case with the uncovered heater. This means that the liquid imbibes through the mat radially outward even after the kinetic energy has completely dissipated. In this scenario, very high heat flux is transferred to the liquid owing to the contact between the liquid and the hot surface. The liquid drop evaporates quickly, and marginal shrinkage of the spreading radius owing to the transition of the liquid to the vapor phase is observed.

However, the maximum spreading radius for scenario (II) is smaller than that for the uncovered heater. In this scenario, the high spreading velocity phase lasts approximately 20 ms. During the

low spreading velocity phase, the liquid is imbibed into the pores of the nanofiber mat, leading to a decrease in the temperature difference between the heater and liquid over time. Therefore, the imbibition of the liquid through the nanofiber mat leads to the gradual spreading of the liquid over the surface.

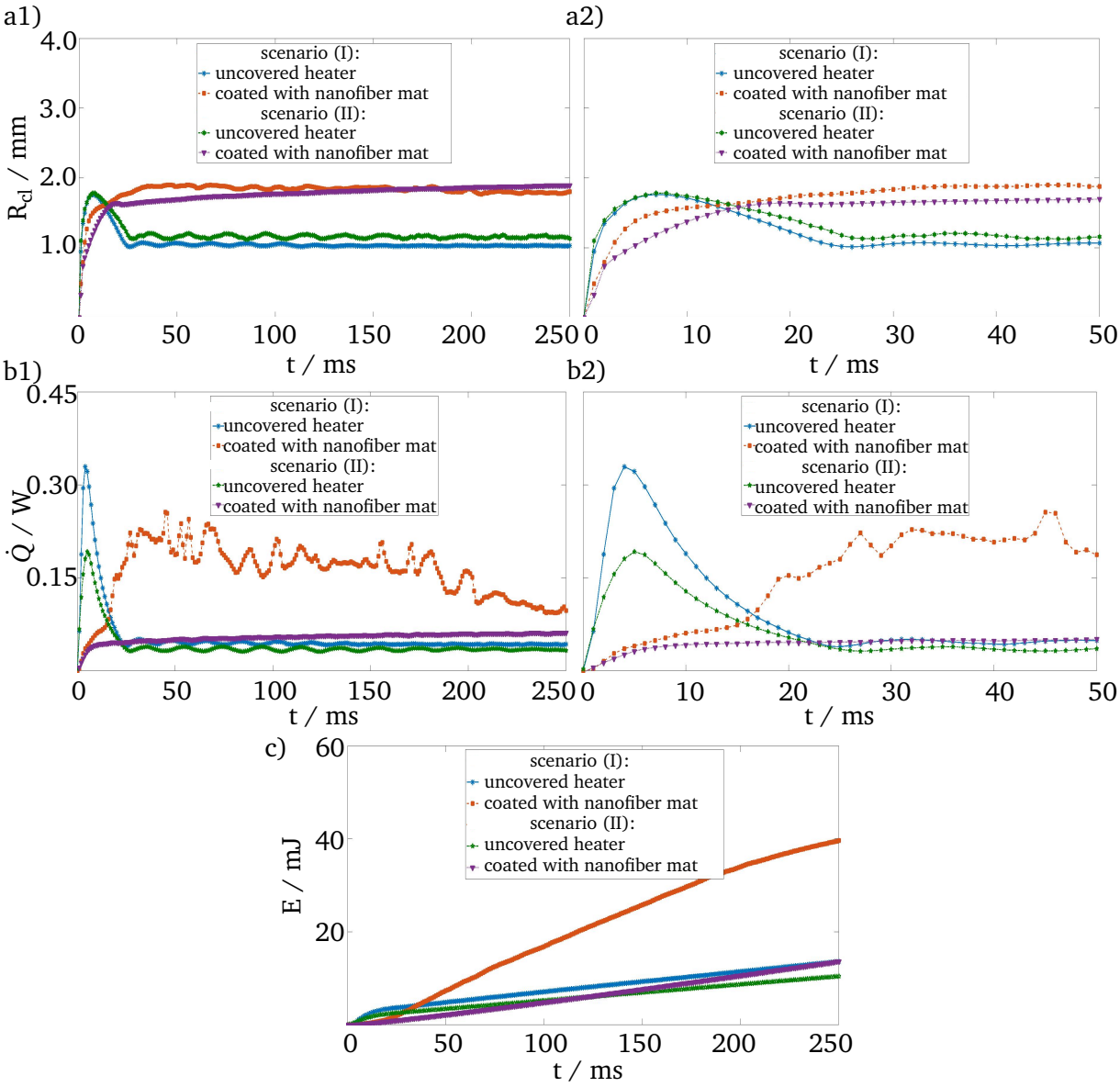

Figure 5.15.: Temporal evolution of the a1, a2) contact line radius, b1, b2) heat flow, and c) cumulative heat flow during the impingement of a single drop onto a bare and a nanofiber-coated heater for the parameters listed in Table 5.1 (a2 and b2 are similar to a1 and b1 but for a shorter time period).

A drastic difference between the two scenarios is evident in the transferred heat flow. As depicted in Figs. 5.15b1 or b2, a high heat flow is transferred to the liquid drop at the initial stages of the impact in the case of an uncovered heater, at which the cold liquid drop contacts directly onto the heater surface. If the heater is coated with the nanofiber mat and scenario (I) occurs, then a large heat flux and a corresponding heat flow comparable to but lower than the maximum heat flow transferred from uncovered heater for a much longer time period is measured. This scenario is characterized by the fluctuation of the heat flow, since the liquid touched the heater

substrate frequently. If scenario (II) occurs, then the heat flow follows the same trend as the spreading radius, and no maximum heat flow is identified. In this scenario, the maximal heat flow is much lower (almost a quarter) than the maximum heat flow measured in the case of the uncovered heater. Starting at t= 22 ms, the heat flow in scenario (II) exceeds the heat flow on the uncovered heater (during the sessile drop evaporation phase).

According to Fig. 5.15c, the drop impact on the uncovered heater is accompanied by a sharp slope of the cumulative heat flow at the early stage of impact owing to the high heat flux in this time period. Afterward, the cumulative heat flow increased almost linearly as the transferred heat flow remains roughly constant during the sessile drop evaporation phase. In the case where the heater is coated with the nanofiber mat and scenario (I) occurs, the cumulative heat flow rapidly rises apart from the initial phase (until t= 17 ms), which is attributed to the high heat flow transferred through the large drop footprint at each time step. If scenario (II) occurs, then the cumulative heat flow still rises, but not as steep as in scenario (I). Regardless of whether scenario (I) or (II) occurs, the cumulative heat flow or the energy transferred from the coated heater exceeds that of the uncovered heater after a specific time (t= 30 ms for scenario (I) and t= 125 ms for scenario (II)). This is associated with a larger drop footprint owing to the presence of the nanofiber mat and suppression of the drop receding phase. It can be generally stated that the presence of the nanofiber mat enhances the energy transferred to the liquid despite the lower local heat flux at the initial stage of impact. The dimensionless form of presented graphs in this Section are given in Annex A.4.1.

Influence of wall superheat

Figures 5.16a, b, and c show the temporal evolution of the spreading radius, heat flow, and cumulative heat flow during drop impact on a surface coated with the nanofiber mat at the wall superheats ranging from 2.2 to 16.3 K. Scenario (II) occurs in all wall superheats except for $\Delta T = 2.2$ K.

As can be suggested based on the data presented in Fig. 5.16b, the liquid drop makes contact with the solid surface several times for $\Delta T = 2.2$ K (scenario (I)). Besides the oscillation of the heat flow in scenario (I), the spreading radius in this scenario is larger than that in scenario (II). Based on the heat flow data depicted in Fig. 5.16b, it can be concluded that scenario (I) is realized at $\Delta T = 2.2$ K compared with $\Delta T = 3.4$ and 7.0 K. This is attributed to the higher local heat flux at different spots of drop footprint. Therefore, the particular behavior of the spreading radius, heat flow, and cumulative heat flow at $\Delta T = 2.2$ K can be explained by the transition from scenario (I) to (II).

For wall superheats equal to or greater than 3.4 K, the spreading radius decreases. An increase in wall superheat leads to a larger spreading radius at the early stage of impact. However, this decreases with time owing to the higher evaporation rate at larger wall superheats. As expected, heat flow and cumulative heat flow rise with increasing wall superheat. In Annex A.4.1, the corresponding dimensionless graphs for various wall superheats are presented.

The time required for complete drop evaporation according to the wall superheat is presented in Fig. 5.16d. In the case of low wall superheat at which scenario (I) occurs, the drop completely evaporates at t = 673 ms, which is slightly quicker than the evaporation time at $\Delta T = 16.3$ K

(t = 680 ms). If the wall superheat increases to 3.4 K but the impact parameters stay constant, then scenario (II) occurs, and the duration of complete drop evaporation increases to 1505 ms. At constant impact parameters, the transition from scenario (I) to (II) during the observation time is accompanied by not only a smaller spreading radius, lower heat flow, and cumulative heat flow but also a longer duration of drop evaporation. If the wall superheat increases further, then the evaporation time for the entire drop is shorter.

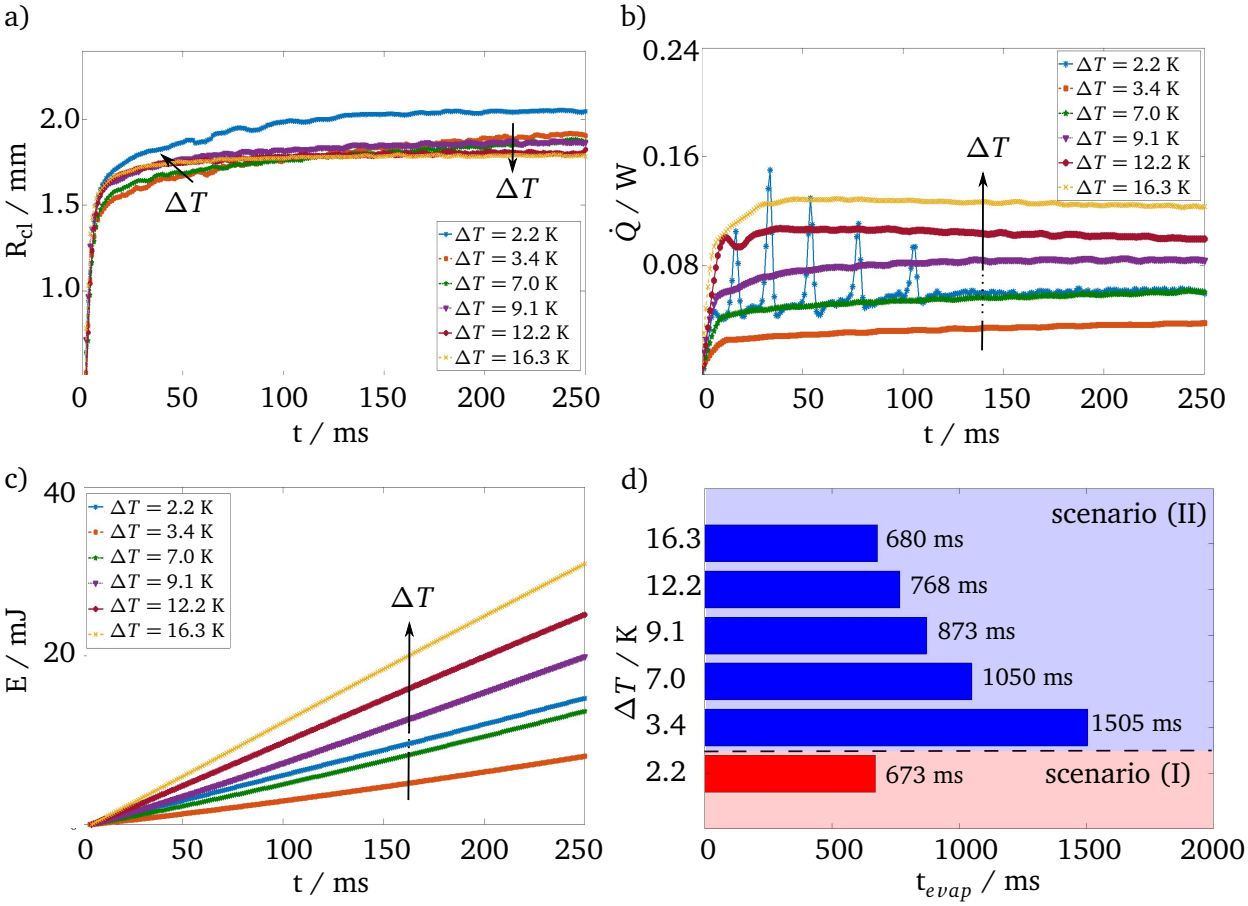

Figure 5.16.: Temporal evolution of the a) contact line radius, b) heat flow, c) cumulative heat flow; and d) the corresponding time duration for entire drop evaporation during the impingement of a single drop onto a nanofiber-coated heater for various wall superheats; ($D_0 = 0.95$ mm, $u_0 = 0.45$ m s^{-1}, p= 0.9 bar, and $h_{mat} = 22$ μm).

Figure 5.17 represents the B/W and IR images during drop impact on an uncovered (left) and a nanofiber-coated (right) heater, kept at a high surface temperature ($\Delta T = 26.6$ K). Nucleate boiling can be clearly observed in the case of the uncovered heater. However, the nucleate boiling is suppressed if the heater is coated with the nanofiber mat. Therefore, the nanofiber-coated surface shifts the onset of nucleate boiling toward larger wall superheats. This behavior is in agreement with the work of Sahu et al. [118], who used nanotextured surfaces during pool boiling.

Figure 5.17 middle-up and middle-bottom compare the heat flow and cumulative heat flow during drop impact on an uncovered heater with nucleate boiling and a nanofiber-coated heater without nucleate boiling, respectively. The second and third maxima in Fig. 5.17b during nucleate boiling arise from the bubble nucleation. It can be observed that despite the high heat flow and corresponding sharp increase in cumulative heat flow during nucleate boiling at the

early stage of impact, the cumulative heat flow for the nanofiber-coated heater exceeds that of the uncovered heater at t= 277 ms owing to the large liquid–solid interface. During the observation time period, more energy is removed from the nanofiber-coated surface compared with the uncovered surface on which nucleate boiling occurs.

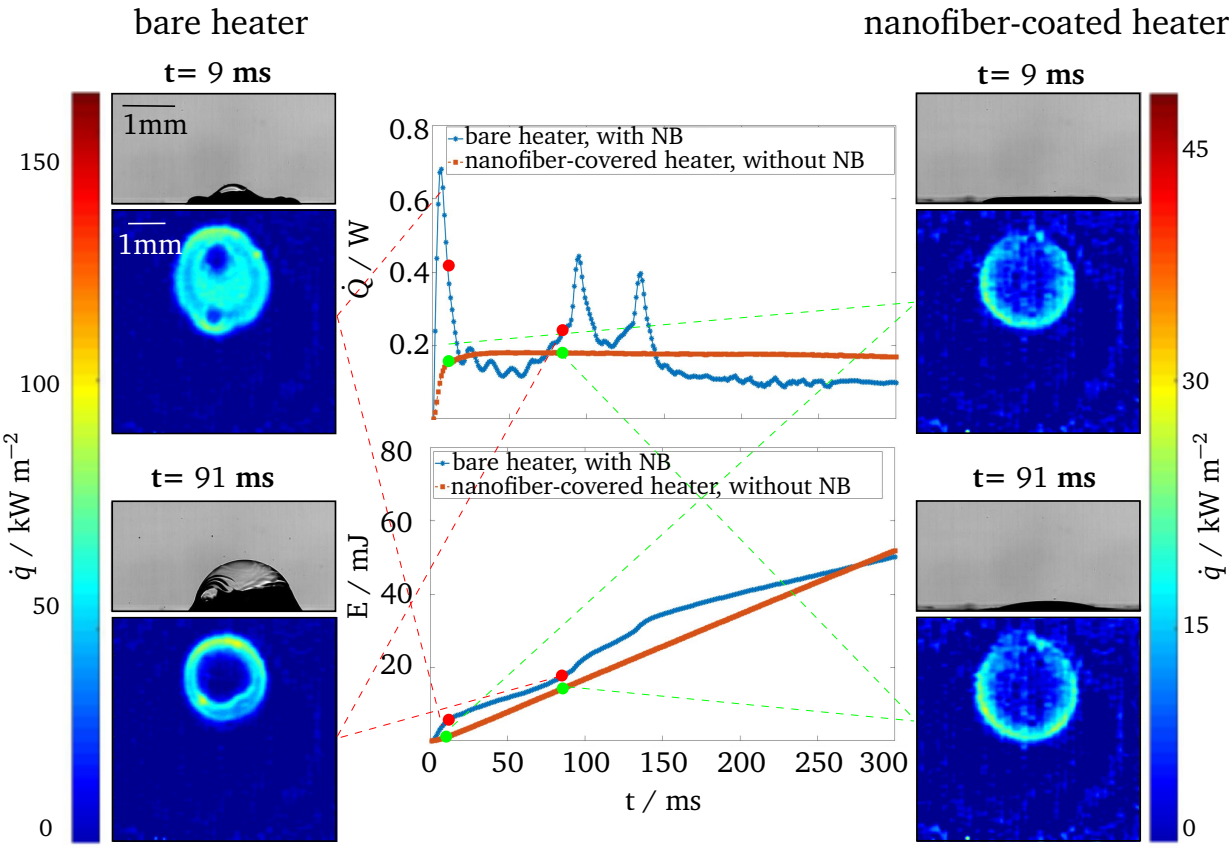

Figure 5.17.: B/W images and heat flux fields at t= 9 and 91 ms during the impingement of a single drop onto a bare heater (left) and a nanofiber-coated heater (right), and the corresponding temporal evolution of the heat flow (middle-up), and cumulative heat flow (middle-bottom) at $\Delta T = 26.6$ K ($D_0 = 0.95$ mm, $u_0 = 0.45$ m s^{-1}, and p= 0.9 bar).

Influence of impact velocity

The temporal evolution of the spreading radius, heat flow, and cumulative heat flow at distinct impact velocities are shown in Figs. 5.18a, b, and c, respectively. The impact velocities are 0.45, 0.54, and 0.58 m s^{-1}, while the other parameters kept constant. As already shown, a higher impact velocity is associated with larger kinetic energy and spreading radius (see Section 5.1.2). This effect also increases the heat flow and cumulative heat flow transferred to the liquid. If the impact velocity is sufficiently high, then the liquid drop expels the vapor trapped between the pores of the nanofiber mat radially outward, is imbibed entirely to the pores and makes contact with the hot heater surface (scenario (I)). As explained earlier, this phenomenon slightly increases the spreading radius and leads to a drastic increase in the heat flow and cumulative heat flow. The corresponding dimensionless graphs for various impact velocities are depicted in Annex A.4.1.

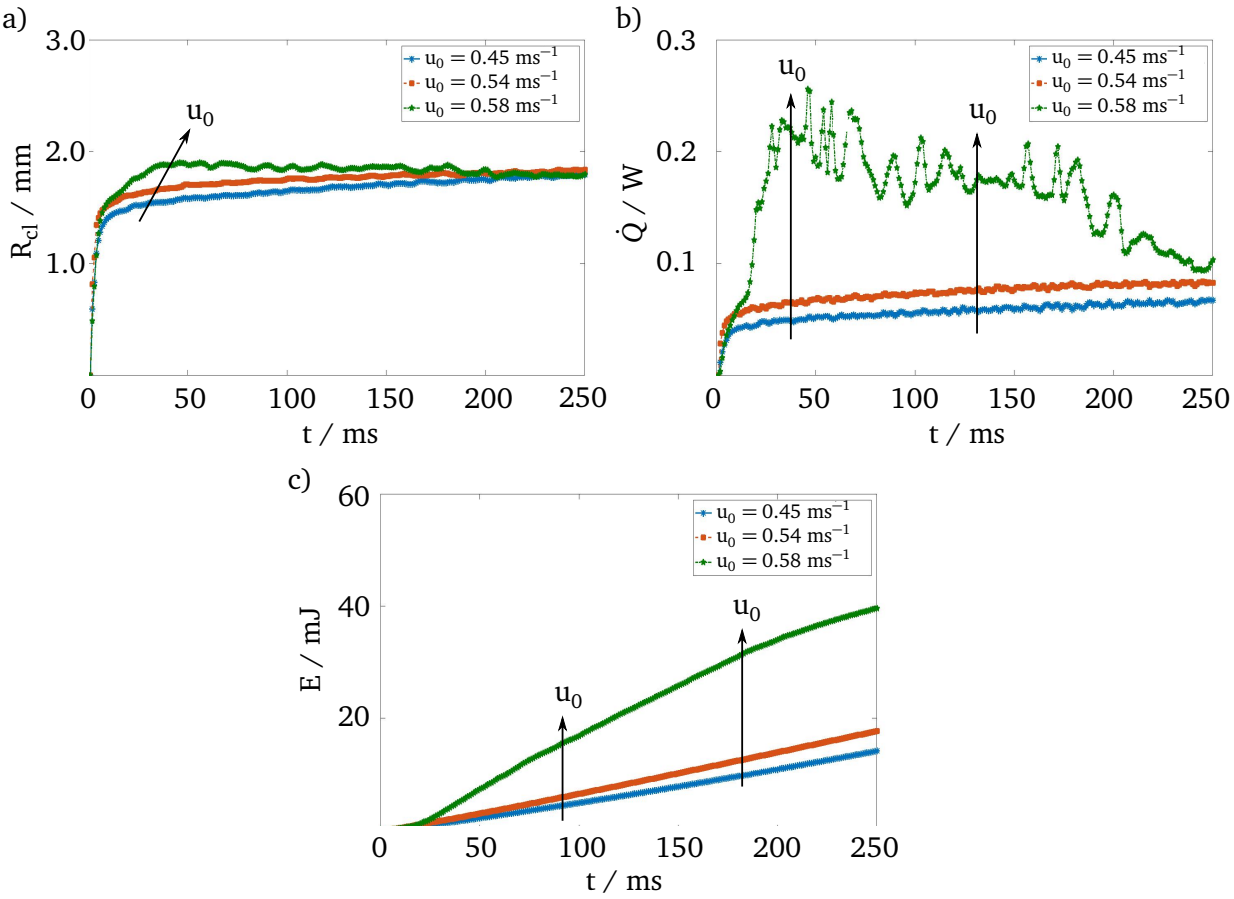

Figure 5.18.: Temporal evolution of the a) contact line radius, b) heat flow, and c) cumulative heat flow during the impingement of a single drop onto a nanofiber-coated heater for various impact velocities ($D_0 = 0.95$ mm, $\Delta T = 9.6$ K, p= 0.9 bar, and $h_{mat} = 22$ μm).

Figure 5.19 depicts the map of scenarios that depend on the wall superheat and impact velocity presented in dimensionless form using the Ja and We numbers. Within the experimental range, it can be observed that at high wall superheats or Ja numbers, scenario (II) occurs independently of the impact velocity or We number. This is mainly attributed to the high evaporation rate at large wall superheats, which prevents the liquid drop from making contact with the heater surface. This scenario also occurs at the lowest Ja and We numbers, at which the inertial force of the drop is not high enough to expel the vapor inside the pores radially outward. Then, the increasing Ja number leads to a regime change from scenario (II) to (I) and then back from (I) to (II). The regime change from scenario (II) to (I) at a constant We number and low Ja numbers may be due to the local surface tension and viscosity changes. This behavior is in line with the results addressed in the work of Srikar et al. [74]. However, the regime change from scenario (I) to (II) at high Ja numbers is due to the high evaporation rate of the liquid inside the pores of nanofiber mat.

Scenario (I) is mostly observed at low Ja and large We numbers, at which the liquid drop penetrates the nanofiber mat. According to the report given in [119] on the impact of liquid drops on different electrospun nanofiber membranes, a threshold impact velocity exists above which the liquid penetrates the membrane. This explains the emergence of scenario (I) at higher We numbers, while the Ja number remains constant.

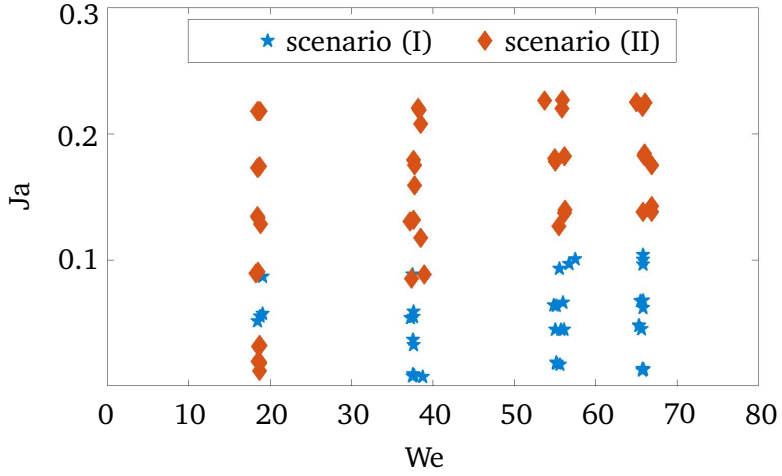

Figure 5.19.: Map of scenarios with dependence upon Ja and We numbers ($D_0 = 0.95$ mm, p= 0.9 bar, $h_{mat} = 18\ \mu$m, 1.2 K $\leqslant \Delta T \leqslant$ 17 K, and 0.32 m s$^{-1} \leqslant u_0 \leqslant$ 0.58 m s^{-1}).

Influence of mat thickness

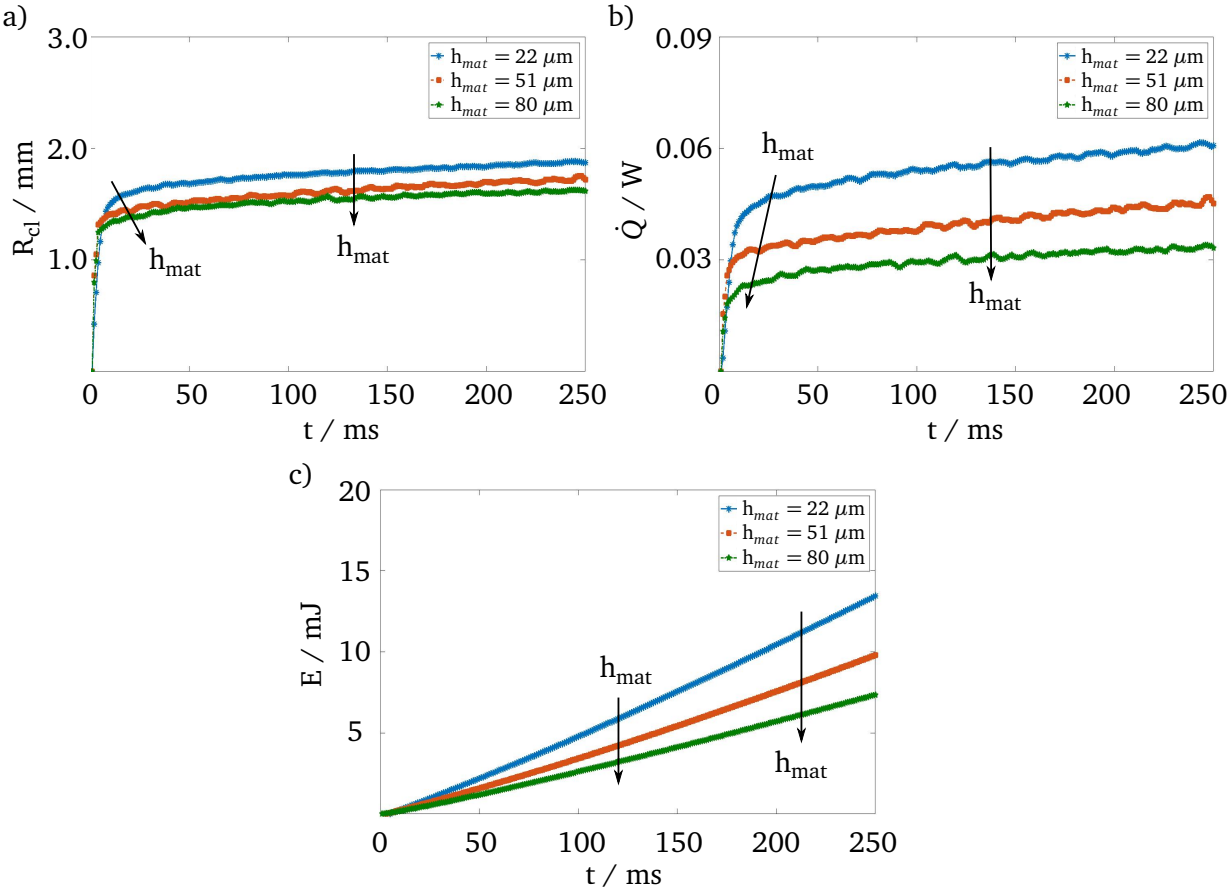

Figure 5.20.: Temporal evolution of the a) contact line radius, b) heat flow, and c) cumulative heat flow during the impingement of a single drop onto a nanofiber-coated heater for various mat thicknesses ($D_0 = 0.95$ mm, $u_0 = 0.45$ m s^{-1}, $\Delta T = 7.0$ K, p= 0.9 bar, and $h_{mat} = 22\ \mu$m).

Figures 5.20a, b, and c show the temporal evolution of the spreading radius, heat flow, and cumulative heat flow for nanofiber mat thicknesses of 22, 51, and 80 μm. At these thicknesses,

only scenario (II) occurs for the chosen impact parameters and wall superheat ($D_0 = 0.95$ mm, $u_0 = 0.45$ m s^{-1}, and $\Delta T = 7.0$ K). Thinner nanofiber mats lead to a larger spreading radius due to a lower dissipation of kinetic energy. If the mat is thinner, then larger heat flow and cumulative heat flow are transferred to the drop. This is mainly attributed to the bigger spreading radius. The corresponding dimensionless graphs for various mat thicknesses are shown in Annex A.4.1.

5.1.6 Summary of the main findings during single drop impingement experiments

The following is a summary of the main results concerning the hydrodynamics and heat transfer behavior with respect to the various influencing parameters during single drop impingement:

- Higher **wall superheats** lead to
  i) smaller maximum spreading radii mainly due to the increase of the apparent contact angle caused by increased evaporation rate in the vicinity of the three-phase contact line, and
  ii) higher heat flow within the first two phases owing to the higher temperature difference between heater surface and liquid drop.

- Higher **impact velocities** and **drop sizes** result in
  i) higher maximum spreading radii mainly due to larger kinetic energy of the liquid drop, and
  ii) higher heat flow within the first two phases owing to the larger drop footprint.

- Higher **system pressures** lead to
  i) almost similar maximum spreading radii but longer duration of the spreading and receding phases due to the slight decline of kinetic energy and a significant decrease of liquid surface tension, and
  ii) a strong decrease in the maximum heat flow mainly due to the reduction in heat flux caused by low liquid thermal effusivity, and a lower heat flow during the sessile drop evaporation phase due to the decrease in latent heat of vaporization.

- Drop impact onto a **nanofiber coated surface** is accompanied by
  i) a slower spreading velocity, suppression of the drop receding phase, and liquid drop imbibition, and
  ii) a decrease in the maximum heat flow but a sharp increase in the cumulative heat flow due to larger drop footprint compared to the drop impact onto an uncoated surface.

- Two scenarios dependent on the wall superheat and impact velocity in case of the drop impact onto a **nanofiber coated surface** are identified; namely,
  i) scenario (I), in which the liquid drop completely penetrates the pores of the nanofiber and reaches the solid heater surface due to the low wall superheats and high impact velocities, and
  ii) scenario (II), in which a large amount of vapor is trapped inside the nanofiber pores preventing the liquid drop from reaching the solid surface, and finally leading to a lower heat flux.

5.2 Multiple drop impingement

The present section addresses the next step in understanding of the spray cooling processes, which is the cumulative effect of the impact of multiple drops onto a solid dry wall. With this objective, the hydrodynamic and heat transport behavior during the vertical coalescence of drops is first demonstrated. Subsequently, the heat transport behavior during the horizontal coalescence of two drops is presented. The reported results in this section are published in [120, 121].

5.2.1 Vertical coalescence

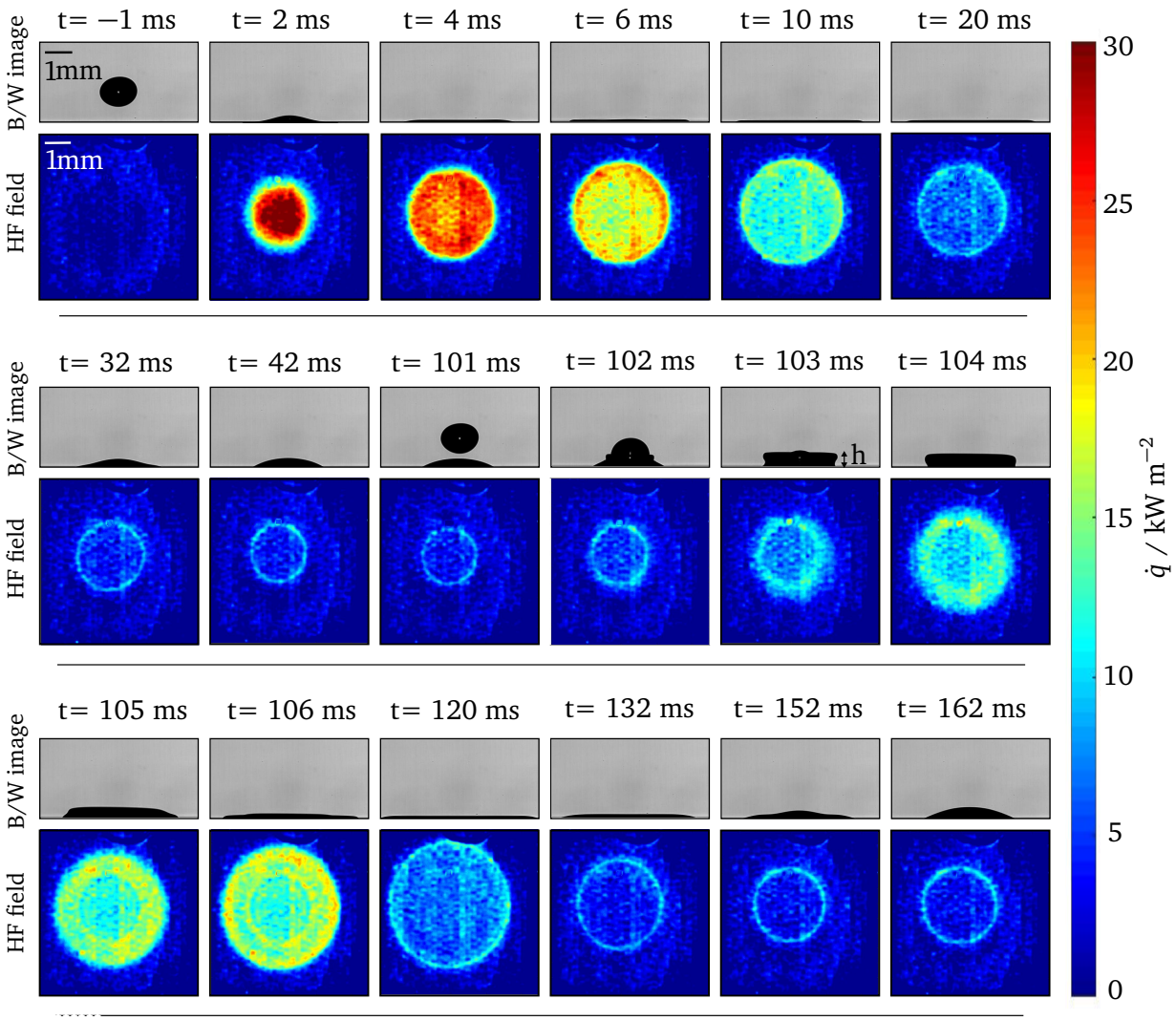

Figure 5.21.: B/W images and heat flux fields for vertical coalescence of two successive drops impinging onto a bare heater ($D_0 = 1.14$ mm, $u_0 = 0.54$ m s^{-1}, $\Delta T = 7.6$ K, p= 0.9 bar, f= 10 Hz, Re= 2160, We= 64, Bo= 0.6, Ja= 0.10, Pr= 9.7, and $p_R = 0.05$).

The side-view of the drop shape evolution captured by the B/W camera, and the temporal evolution of the heat flux distribution determined from the IR images for the first 162 ms after the first impact, are presented in Fig. 5.21. As already demonstrated in Section 5.1 and shown during the first drop impact of Fig. 5.21, the drop impact onto a bare and dry surface is

accompanied by three phases; namely, spreading, receding and sessile drop evaporation phases. The maximum heat flux near the apparent three-phase contact line is observed for the experiment starting from t= 6 ms.

The drop impact frequency is moderate so that each subsequent drop impinges onto a previous drop in the sessile drop evaporation phase. The second drop impacts vertically onto the first drop at t = 102 ms. The B/W images show that, similar to the works of Fujimoto et al. [84–86] and Minamikawa et al. [88], the bottom part of the second drop swells up to a specific height, and the three-phase contact line moves radially outward (t = 102 and 103 ms). The heat flux around the impact location increases after the impact of the second drop (from t = 102 to 106 ms), but it does not reach the maximum heat flux observed immediately after the first impact. At t = 105 and 106 ms, two thin ring-shaped regions of high heat flux can be identified: one corresponding approximately to the position of the contact line of the first drop prior to the second impact, and the other corresponding to the contact line of the combined drop. The appearance of the inner ring with a high heat flux might be attributed to the small local thickness of the liquid film, and, accordingly, the low local thermal resistance of the liquid layer, or to the high microscale flow velocity in this region. The exact reason for the formation of the heat flux distribution at t = 105 ms and 106 ms depicted in Fig. 5.21 can be elucidated by analyzing the drop shape and velocity distribution, which can be predicted via numerical simulations. Similar to the first impact, the contact line radius reaches its maximum and then begins to decrease (starting from t = 120 ms). The footprint of the sessile drop after the second impact is slightly larger than that after the first impact.

i. Hydrodynamic behavior

The temporal evolution of the contact line radius during the impact of four successive drops with the frequency of 10 Hz onto the same impact location is depicted in Fig. 5.22a. For better comparability of the results, the time is set to zero at the instant of each impact. The durations of the spreading phase, and especially, the receding phase increase after each impact. Moreover, the maximum contact line radius increases after each impact. This is attributed to the larger mass of the liquid wetting the heater surface. This behavior of the contact line radius is qualitatively consistent with the results of Guggilla et al. [71]. The rate of the increase of the maximum contact line radius decreases during the third and fourth impacts. The drop oscillates with various frequencies and amplitudes at the end of the receding phase after each impact. The oscillation frequency of the contact line radius after the receding phase decreases with the increasing drop sequential number; however, its amplitude increases.

The maximum heights of the merged drops that swell after each impact (see Fig. 5.21 at t= 103 ms), post-processed from the B/W images, are listed in Table 5.2. The results show a non-linear growth of the maximum height after each impact so that the early impacts are accompanied by a larger rate of increase in the maximum height.

Table 5.2.: Maximum height of the combined drop after individual impacts.

Impact Nr.	1	2	3	4
Height / μm	380	511	598	652

ii. Heat transfer behavior

Figure 5.22b shows the temporal evolution of the heat flow from the heater to the liquid drop. Despite a low heat flux after the second impact caused by the pre-cooling effect of the first drop and the lack of direct contact between the cold liquid drop and the hot substrate, a higher maximum heat flow after the second impact is observed. This is attributed to the larger footprint of the drop, as illustrated in Fig. 5.22a. The value of the maximum heat flow is determined by the level of heat flux (which is lower for the impact of the second drop than for the first drop) and the maximum size of the footprint of the drop (which is higher for the second drop). A small increase in the maximum heat flow is observed after the third and fourth impacts. This agrees with the behavior of the maximal spreading radius. The oscillations in the heat flow at the end of the receding phase are due to the oscillations of the contact line radius.

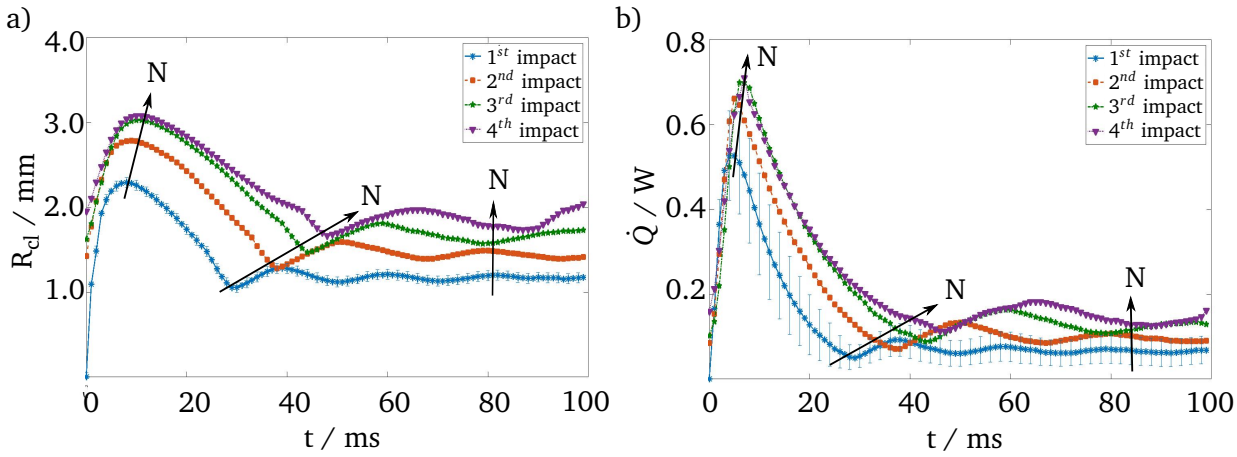

Figure 5.22.: Temporal evolution of the a) contact line radius and b) heat flow during the vertical coalescence of four successive drops impinging onto a bare heater ($D_0 = 1.14$ mm, $u_0 = 0.54$ m s^{-1}, $\Delta T = 12.4$ K, p= 0.9 bar, and f= 10 Hz).

Figure 5.23a and b present the spreading ratio and dimensionless heat flow versus dimensionless time for the impact of four successive drops. The dimensionless parameters follow the same trend as the dimensional ones, since the impact parameters and fluid properties remain constant. As already observed from the single drop impact experiments presented in Section 5.1, the spreading ratio during the sessile drop evaporation phase reaches a constant value of approximately 2. This value has been observed to be independent of the Re and We numbers in the respective ranges $1000 < Re < 2500$ and $20 < We < 60$, and marginally dependent on the Ja number. Assuming that i) the merged sessile drops formed after each impact have the shape of a spherical cap, ii) the apparent contact angle remains the same after each impact, and iii) the evaporation mass loss is negligible, the below equation can be approximated for the spreading ratio in the sessile drop phase after the N^{th} impact:

$$S_N = 2\,(N)^{\frac{1}{3}}\,, \tag{5.2}$$

which yields $S_2 = 2.5$, $S_3 = 2.9$, and $S_4 = 3.2$ (see the black lines in Fig. 5.23a). It can be observed that the measured spreading ratios in the sessile drop evaporation phase are consistent with the computed values.

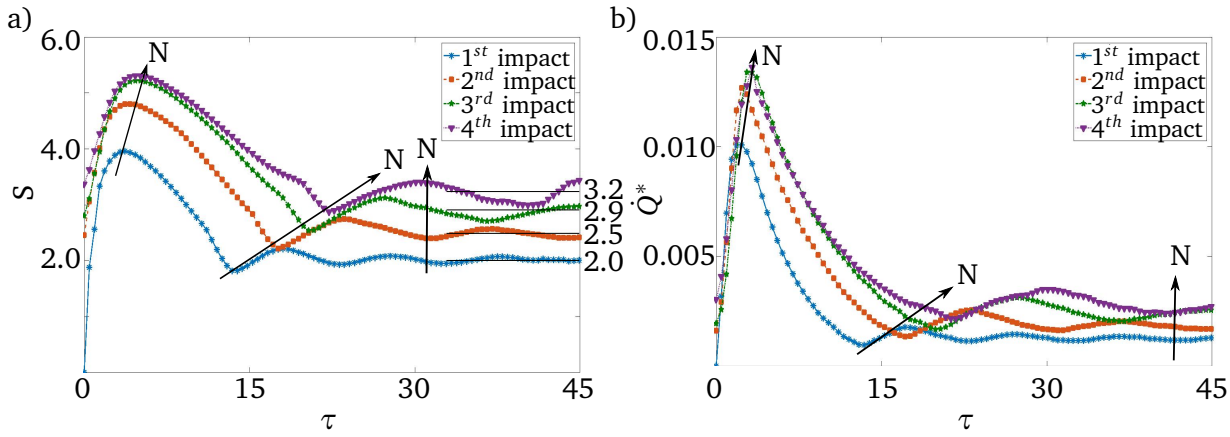

Figure 5.23.: a) Spreading ratio and b) dimensionless heat flow versus dimensionless time during the vertical coalescence of four successive drops impinging onto a bare heater (f= 10 Hz, Re= 2160, We= 64, Bo= 0.6, Ja= 0.16, Pr= 9.7, and $p_R = 0.05$).

Table 5.3 shows the heat transferred during each individual drop impact, E_N, and the same heat flow non-dimensionalized by the latent heat of vaporization of one drop, E_N^*. The results show that both aforementioned parameters increase with increasing drop sequential number, mainly due to the growth of the drop footprint and consequently increasing of the heat flow.

Table 5.3.: The transferred heat for the time period starting from the impact of each individual drop until the next impact, E_N, non-dimensionalized by the latent heat of vaporization, E_N^*.

Impact number	E_N / mJ	E_N^*
1^{st} impact (N= 1)	12.1	0.108
2^{nd} impact (N= 2)	17.6	0.156
3^{rd} impact (N= 3)	21.6	0.192
4^{th} impact (N= 4)	23.9	0.212

The corresponding dimensional and dimensionless cumulative heat flow for the aforementioned measurements are depicted in Annex A.4.2.

Influence of wall superheat

The temporal evolution of the contact line radius and heat flow during the successive impact of two drops onto a bare heater at different wall superheats are presented in Fig. 5.24a and b, respectively. Similar to the single drop impact, higher values of the wall superheat lead to a lower maximum contact line radius, a quicker receding phase, and stronger oscillations at the end of the receding phase, after both first and second impacts (see Section 5.1.1). Additionally, an increase in the wall superheat leads to an increase in the heat flow transferred to the liquid–solid interface after the first and second impacts.

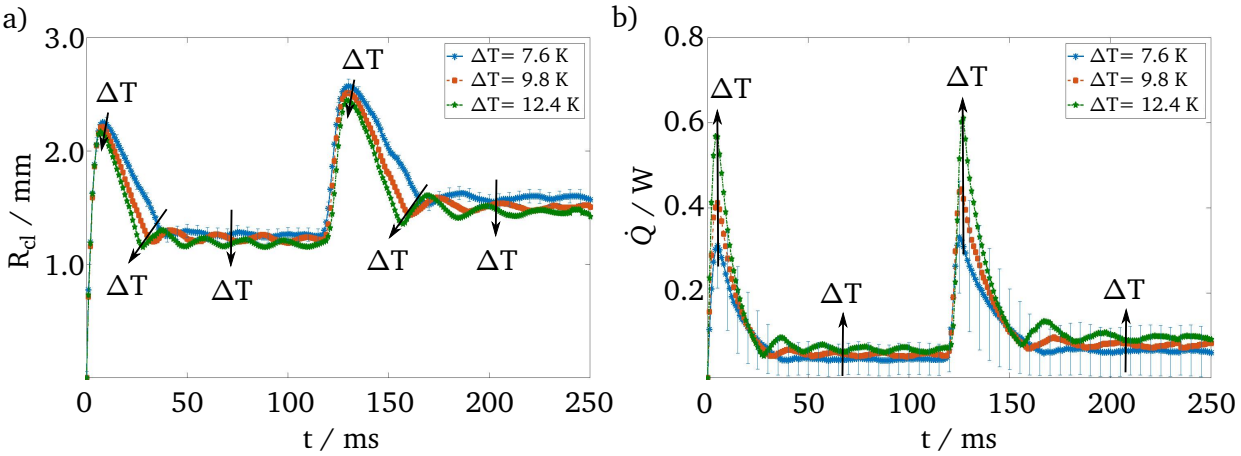

Figure 5.24.: Temporal evolution of the a) contact line radius and b) heat flow during the vertical coalescence of two successive drops impinging onto a bare heater for various wall superheats ($D_0 = 1.14$ mm, $u_0 = 0.54$ m s^{-1}, p= 0.9 bar, and f= 10 Hz).

Annex A.4.2 provides the spreading ratio, dimensionless heat flow, and dimensionless cumulative heat flow for the above-mentioned measurements.

Influence of drop generation frequency

The temporal evolution of the contact line radius and heat flow during the successive impact of two drops onto a bare heater at different frequencies are presented in Fig. 5.25a and b, respectively. A change in the drop generation frequency only shifts the curves horizontally to an earlier time due to the different time intervals between the first and second impacts. The maximum contact line radii remain approximately constant because for all frequencies in the studied range, the second drop impacts during the sessile drop evaporation phase of the first drop. The shape of the drop in this phase changes very slowly due to the low evaporative mass loss. Therefore, the difference in the evolution of the contact line radius between different frequencies is marginal.

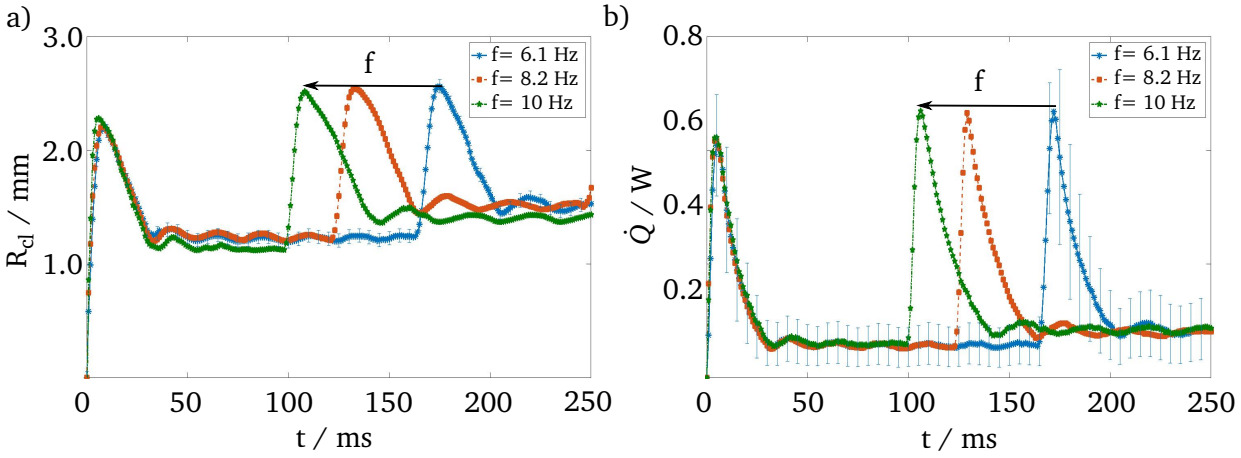

Figure 5.25.: Temporal evolution of the a) contact line radius and b) heat flow during the vertical coalescence of two successive drops impinging onto a bare heater for various drop generation frequencies ($D_0 = 1.14$ mm, $u_0 = 0.54$ m s^{-1}, $\Delta T = 9.8$ K, and p= 0.9 bar).

An increase in the drop generation frequency only shifts the heat flow curves of the second impact to an earlier time. However, the maximum heat flow during the impact of the second drop is nearly independent of the drop generation frequency in the studied range. The spreading ratio, dimensionless heat flow, and dimensionless cumulative heat flow for above-mentioned measurements are given in Annex A.4.2.

5.2.2 Horizontal coalescence

The side-view of the drop shape evolution captured by the B/W camera, and the temporal evolution of the heat flux distribution determined from the IR images for the first 60 ms after the impact, are presented in Fig. 5.26. During this experiment, the wall superheat and the distance between the impact locations are set to 7.3 K and 2 mm, respectively. As already mentioned in Section 3.6, simultaneous drop impact in this work corresponds to the impact of two drops with a time difference of about 1 ms.

The interaction between the drops is characterized by the spacing parameter

$$e = \frac{d}{D_0}, \tag{5.3}$$

which is defined as the ratio of the distance between two drops, d, and their initial diameter, D_0.

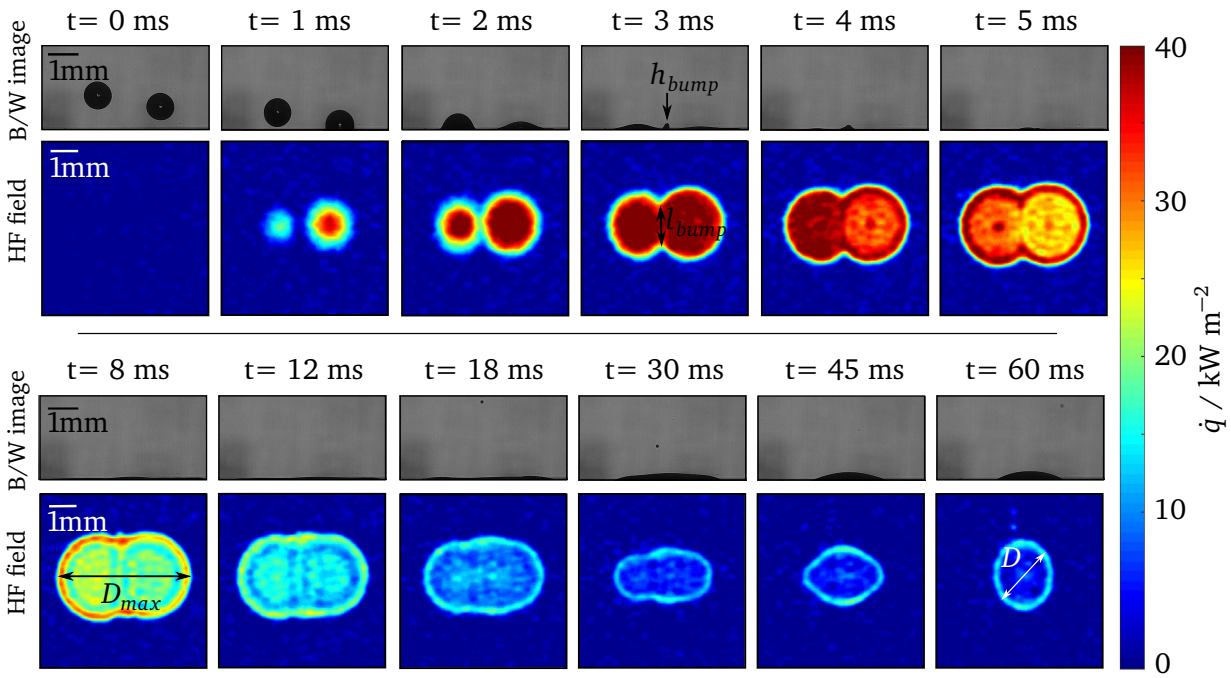

Figure 5.26.: B/W images and heat flux fields for 60 ms after simultaneous impact of two drops onto a bare heater (D_0 = 0.93 mm, u_0 = 0.53 m s^{-1}, ΔT = 7.3 K, p= 0.9 bar, e= 2.15, Re= 1700, We= 49, Bo= 0.4, Ja= 0.09, Pr= 9.7, and p_R = 0.05).

Similar to single drop impact, high local and overall heat fluxes are transferred to the liquid in the first few milliseconds when both drops wet the heater surface. One can notice that the heat

flux is not influenced by the presence of a nearby drop as long as the drops do not touch each other.

At the time interval between 2 and 3 ms, the rims of both drops touch each other, and the drops start to coalesce. The liquid within the spreading lamella of each individual drop still has considerable kinetic energy at this early stage of the impingement. A stagnation point occurs at the position where the two contact lines touch each other due to the interaction of the drops. This leads to a redirection of the liquid flow towards the side and upwards, and, accordingly, to the formation of a bump between the drops (see Fig. 5.26, t= 3 ms). This bump is similar to the bumps and liquid sheets observed in [89–91]. The spreading process in terms of hydrodynamics and heat flux far from the interaction region is not influenced by the drop coalescence. Similar to the single drop impact presented in Fig. 5.1, a region with high heat fluxes in the proximity of the three-phase contact line of the combined drop can be observed. The spreading process of the combined drop ends due to the dissipation of kinetic energy (t= 8 ms). The combined drop then starts to shrink driven by the surface tension force, which tends to minimize the surface area of the liquid. From this point on, low heat flux at the liquid–solid interface is observed everywhere, apart from the apparent three-phase contact line. After some time (t= 60 ms), the combined drop reaches the equilibrium state, forming a single sessile drop with a circular footprint.

Influence of spacing parameter

Figure 5.27 compares the temporal evolution of the drop shape and heat flux for various spacing parameters during the simultaneous impingement of two drops onto a heated surface. The height and length of the established bump are dependent upon the spacing parameter. In this study, the spacing parameters are 1.18, 2.15, and 3.33.

If the spacing parameters is large, the hydrodynamic interactions and first contact between the two drops occur later. At this stage of coalescence, the initial kinetic energy of the drops has almost completely been dissipated, leading to the appearance of a bump with thinner height and shorter length in this hydrodynamic interaction zone (see Fig. 5.27 at t= 12 ms for the entire spacing parameters). The maximum height and length of the bumps ($h_{\mathrm{bump,max}}$, $l_{\mathrm{bump,max}}$) for the investigated spacing parameters are listed in Table 5.4.

Moreover, the large distance between the drops might induce a temporary coalescence of drops. This phenomenon is depicted in Fig. 5.27 at $e = 3.33$, showing both drops initially coalesce during the advancing phase. Afterward, they shrink during the receding phase, and the length of the bump becomes extremely narrow. The bump becomes unstable and finally ruptures, leading to the formation of two individual sessile drops.

Table 5.4.: Maximum height and length of the bump for various spacing parameters.

e	$h_{\mathrm{bump,max}}$ / mm	$l_{\mathrm{bump,max}}$ / mm
1.18	0.293	4.9
2.15	0.185	3.06
3.33	0.044	1.76

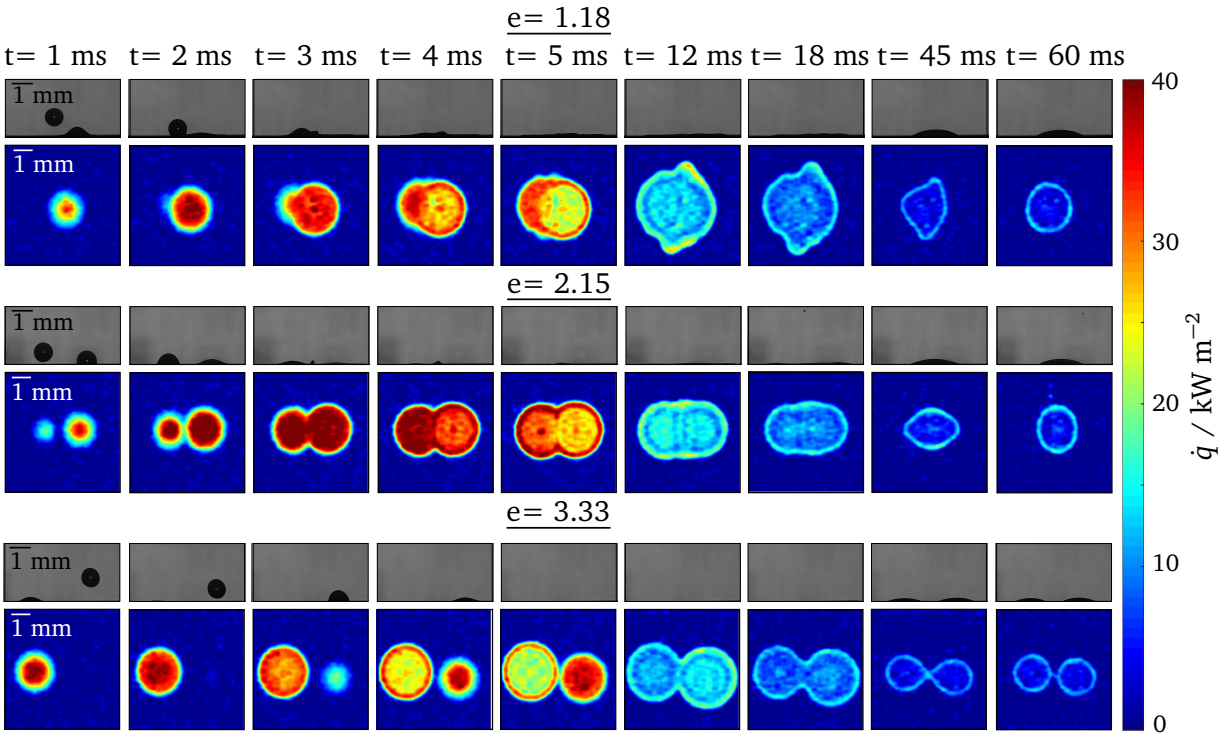

Figure 5.27.: B/W images and heat flux fields for 60 ms after simultaneous impact of two drops onto a bare heater for various spacing parameters ($D_0 = 0.93$ mm, $u_0 = 0.53$ m s^{-1}, $\Delta T = 7.3$ K, p= 0.9 bar, Re= 1700, We= 49, Bo= 0.4, Ja= 0.09, Pr= 9.7, and $p_R = 0.05$).

Figure 5.28a and b present the temporal evolution of the heat flow and cumulative heat flow during the simultaneous impingement of two drops onto a heated surface for different spacing parameters. The spacing parameters of 1.18, 2.15, and 3.33 lead to horizontal drop coalescence. The spacing parameter of ∞ represents the simultaneous impingement of two drops without any interactions, and the corresponding heat flow is equivalent to twice the heat flow of a single drop impact. The experimental results show that the heat flow is not influenced by the presence of a second drop as long as the drops do not touch each other. Once the drops start to coalesce, the heat flow during the spreading and receding phases for $e = 2.15$ is close to the case of two independent drops ($e = \infty$). At $e = 3.33$, the heat flow during the spreading and receding phases are almost equal to those of $e = 2.15$, and ∞, except for the time period between 22 and 35 ms (end of the receding phase), when the drops are still bonded together with a thin liquid bridge. High heat flow in this time period is attributed to the high heat transport due to the small thermal resistance at this thin intersection region of two drops preceding the separation.

If the distance between the impact locations reduces to $e = 1.18$, the heat flow gradient during the receding process declines, since the receding phase takes longer. This could be due to outward flow from the region of contact, which leads to a temporary increasing of the area and contact line length in between 10 and 40 ms.

The maximum heat flow for $e = 1.18$ is lower than that of $e = 2.15, 3.33$, and ∞. The decline of heat flow is attributed to the early drop coalescence leading to the decrease of the cumulative solid–liquid contact area compared with the area, which can be occupied by two independent drops. This is in agreement with the numerical simulations presented in [91].

At the later stages of impact in which a single sessile drop is formed, the heat flow through the liquid–solid interface transferred to the combined drop is independent of the spacing parameter and is lower compared to the case of two independent drops. The lower heat flow of the combined drop during the sessile drop evaporation phase is attributed to the shorter cumulative liquid–solid contact area and shorter cumulative length of the three-phase contact line due to coalescence. As already shown in Fig. 5.2, the heat flow in the proximity of the three-phase contact line during the sessile drop evaporation phase comprises almost half of the overall heat flow.

The drop coalescence is accompanied by lower cumulative heat flow in comparison with the case of non-coalescence. This is mainly due to the greater cumulative liquid–solid contact area and the larger cumulative length of the three-phase contact line during two separate drop impacts. Decreasing the distance between the impact locations reduces the cumulative heat flow during the spreading phase. However, the longer receding process (for $e = 1.18$) enhances the cumulative heat flow if two drops come closer. Annex A.4.2 presents the temporal evolution of the heat flow and cumulative heat flow for various spacing parameters in dimensionless forms.

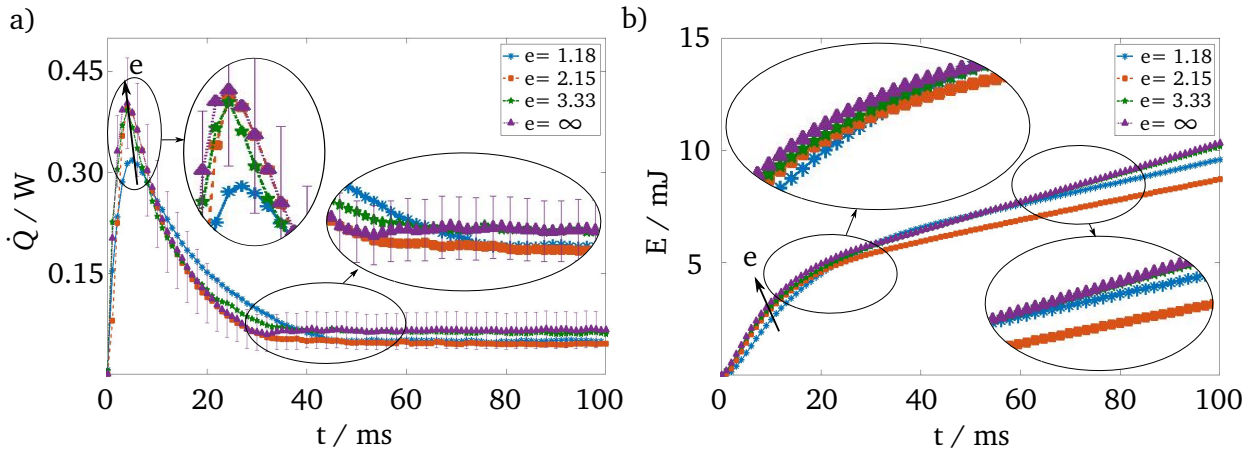

Figure 5.28.: Temporal evolution of the a) heat flow and b) cumulative heat flow during the simultaneous impact of two drops onto a bare heater for various spacing parameters; e= ∞ represents the non-coalescence case ($D_0 = 0.93$ mm, $u_0 = 0.53$ m s^{-1}, $\Delta T = 7.3$ K, and p= 0.9 bar).

Influence of wall superheat

Table 5.5 compares the maximum wetted area (A_{max}) and the wetted area corresponding to the sessile drop ($A_{sessile}$) during the simultaneous impingement of two drops for various wall superheats of 4.6, 7.3, and 12.4 K. The areas are assessed from post-processing of the IR images. As can be seen, both parameters decline with increasing wall superheat. This is attributed to the higher evaporation rate near the three-phase contact line at higher wall superheats, in particular during the sessile drop evaporation phase. High evaporation rate near the three-phase contact line leads to a microscale flow of liquid from the bulk into the contact line region, leading to an increase in the apparent contact angle, and, accordingly, a smaller liquid–solid contact area.

Table 5.5.: Maximum wetted area (A_{max}) and the wetted area corresponding to the sessile drop ($A_{sessile}$) during the simultaneous impingement of two drops for various wall superheats at e= 2.15.

ΔT / K	A_{max} / mm^2	$A_{sessile}$ / mm^2
4.6	1490	566
7.3	1418	495
12.4	1352	431

Figures 5.29a and b show the temporal evolution of the heat flow and cumulative heat flow during the simultaneous impingement of two drops onto a heated surface with various wall superheats. An increase in wall superheat enhances both heat flow, and, accordingly, cumulative heat flow. Both contact area and heat transport behavior are in line with the results addressing the influence of wall superheat during the impingement of a single drop and successive drops onto a heated surface presented in Sections 5.1.1 and 5.2.1, respectively.

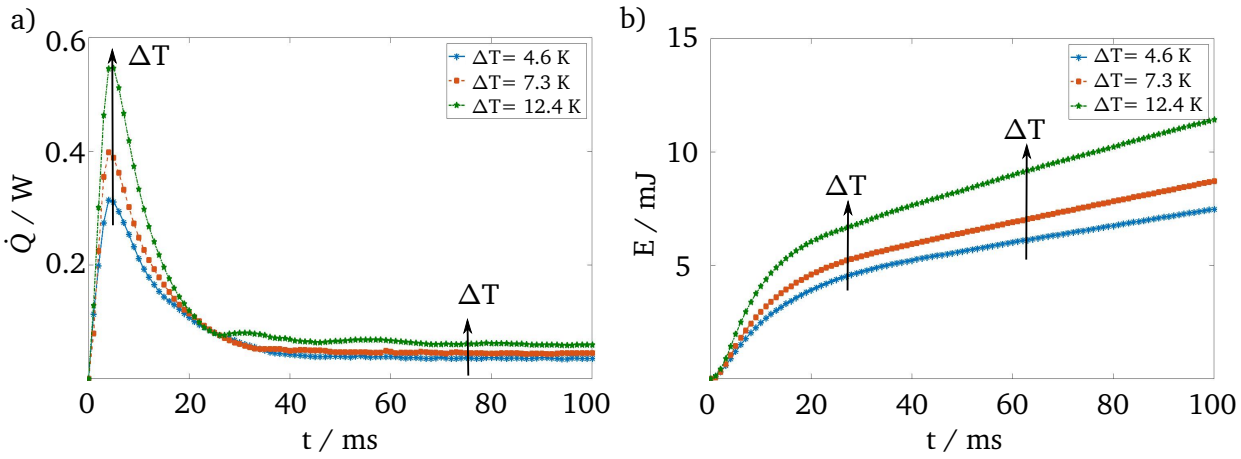

Figure 5.29.: Temporal evolution of the a) heat flow and b) cumulative heat flow during the simultaneous impact of two drops onto a bare heater for various wall superheats ($D_0 = 0.93$ mm, $u_0 = 0.53$ m s^{-1}, p= 0.9 bar, and e= 2.15).

Influence of time interval

The temporal evolution of the drop shape and heat flux during the horizontal coalescence of two drops for one exemplary time interval of $\Delta t = 15$ ms is depicted in Fig. 5.30. In terms of hydrodynamics, when there is a delay between the impacts, the bump is thinner and inclined from the vertical towards the earlier drop (see Fig. 5.30 at $t = 17$ ms). This leads to the formation of a liquid flow on the upper side and towards the opposite side of the earlier drop. This behavior can be attributed to the differences in the kinetic energy for individual drops preceding horizontal coalescence. However, the heat flow transferred through the earlier drop is not affected by the developed liquid flow. This confirms that the heat transport process far from the interaction region is not influenced by the drop coalescence. During the sessile drop evaporation phase, the center of the sessile drop stays in the same location and is independent of the time interval between drop impacts.

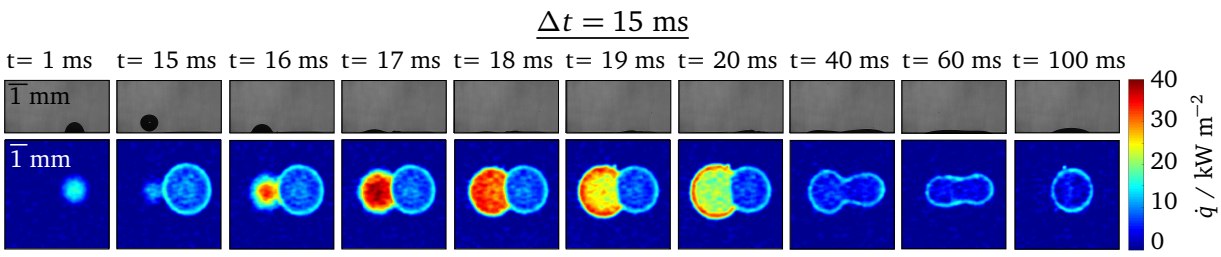

Figure 5.30.: B/W images and heat flux fields during the horizontal coalescence of two non-simultaneous drops over a bare heater ($D_0 = 0.93$ mm, $u_0 = 0.53$ m s^{-1}, $\Delta T = 7.3$ K, $\Delta t = 15$ ms, e= 2.15, Re= 1700, We= 49, Bo= 0.4, Ja= 0.09, and Pr= 9.7).

The temporal evolution of the heat flow and cumulative heat flow during the horizontal coalescence of two drops impacting with various time intervals onto a bare heater are presented in Figs. 5.31a and b, respectively. The time intervals are chosen so that the later drop impinges during the spreading (Δt= 4 ms), receding (Δt= 15 ms), and sessile drop evaporation (Δt= 45 ms) phases of the earlier drop. As can be seen, the maximum heat flow during the simultaneous impact is larger in comparison with non-simultaneous impact. If the later drop impacts during the spreading phase of the earlier drop, the maximum heat flow reduces and shifts to a later time instance. Once the later impact occurs during either receding or sessile drop evaporation phases of the earlier impact, two identical heat flow maximums can be observed; the first maximum corresponds to the impact of the earlier drop, and the second maximum to the impact of the later drop. Besides, the heat flow during the sessile drop evaporation phase after the later impact is independent of the time interval between the impacts. As intuitively expected, the cumulative heat flow reduces by prolonging the time interval between the impacts. In Annex A.4.2, the temporal evolution of the heat flow and cumulative heat flow for various time intervals in dimensionless forms are presented.

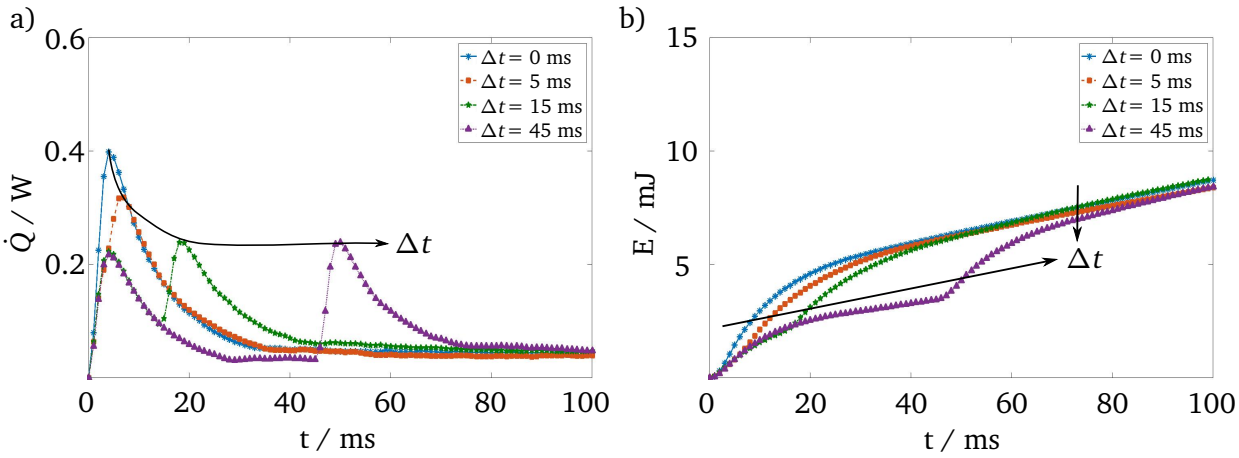

Figure 5.31.: Temporal evolution of the a) heat flow and b) cumulative heat flow during the horizontal coalescence of two drops impacting with various time intervals onto a bare heater ($D_0 = 0.93$ mm, $u_0 = 0.53$ m s^{-1}, $\Delta T = 7.3$ K, p= 0.9 bar, and e= 2.15).

5.2.3 Summary of the main findings during multiple drop impingement experiments

A summary of the significant observations concerning the vertical and horizontal coalescence of two drops are presented following:

- **Vertical coalescence** of two drops is accompanied by
  i) larger maximum contact line radius and maximum heat flow after each impact compared with those after the previous impact mainly due to larger footprint of the drop,
  ii) smaller maximal local heat flux after the second impact than that of the first impact due to the pre-cooling effect by the first drop, and
  iii) the appearance of two thin ring-shaped zones of high heat flux; one corresponding approximately to the position of the contact line of the first drop prior to the second impact, and the other corresponding to the contact line of the combined drop.

- **Horizontal coalescence** of two drops is accompanied by
  i) the emergence of an uprising central sheet (bump) at the intersection region,
  ii) a decrease in the overall heat flow due to the smaller liquid–solid interface and shorter cumulative length of the contact line,
  iii) a strong decrease in maximum heat flow when the distance between the impact locations decreases, and
  iv) inclination of the bump towards the earlier drop which induces liquid flow from the later drop on the upper side and towards the opposite side of the earlier drop when the time intervals between impacts increases.

6 Summary, Conclusion and Outlook

6.1 Summary and Conclusion

In this study, the non-isothermal drop impingement by the presence of evaporation has been investigated for various impact parameters, system, and surface conditions. High resolution temperature measurement technique is employed to obtain a detailed knowledge of hydrodynamics and heat transfer mechanisms during the drop impingement. The research is motivated by a wide range of industrial applications, such as spray cooling. No generic model has been so far developed to predict the heat transfer and cooling effectiveness during non-isothermal spray impact for a wide range of operating conditions. Thus, understanding the single drop impact is an essential and preliminary step towards describing and modeling of spray cooling processes. Besides, the fundamental knowledge obtained from simple configurations of drop–drop interactions such as vertical and horizontal coalescence of drops with equal impact parameters facilitate understanding in spray systems. The main objective of the present thesis is to enhance the understanding of non-isothermal drop–wall and drop–drop interactions in a pure vapor atmosphere at a moderate wall surface temperatures. These experimental results jointly with an appropriate model can contribute to better understanding the mechanisms of spray cooling and thus, improving the future spray systems.

To provide a pure atmosphere, the measurements have been performed inside a sealed temperature-controlled high-pressure test cell. Refrigerant FC-72 (perfluorohexane) is used as the working fluid. Having relatively low critical temperature and pressure makes this liquid suitable for high-pressure investigations. The pressure inside the cell is determined by the fluid temperature. A high-temperature thermostat is employed to control the fluid temperature, and, accordingly, the system pressure. A high-pressure syringe pump unit is used to generate reproducible drops under the desired conditions. The impact velocity and drop diameter have been varied by using different needle heights and diameters, respectively. With the employed syringe pump, it is possible to generate a single drop at high pressures, generate successive drops by variation of the dispensing volume flow rate, and generate two drops with short time differences (less than 1 ms) by connecting two units in parallel.

The IR transparent heater employed in this thesis has not only the thermal diffusivity in the same range as that of stainless steels, which are used to manufacture evaporation devices, but also due to its large thickness, its thermal capacity per surface area is much closer to technical applications than thin foil heaters commonly used in boiling and drop evaporation studies. Moreover, the cumulative thickness of the coating layers is less than 1 μm, leading to temperature measurements extremely close to the fluid–solid interface with high spatial and temporal resolution using IR-thermography. Variation of the input heat flux to the heater, and, accordingly, wall superheat has been realized by varying the electrical power.

The temperature distribution close to the fluid–solid interface has been measured with an in-situ calibrated high-speed IR thermography at a framerate of 1000 Hz with a spatial resolution of

29.27 μm/pixel. For the series of experiments, in which the influence of drop size has been investigated and horizontal coalescence of two drops has been studied the spatial resolution of 40.82 μm/pixel has been used to ensure that the whole wetted area stays within the field of view of the camera. The IR camera has been synchronized with a high-speed black and white camera to visualize the drop hydrodynamics and evaluate the impact parameters with a spatial resolution of 10.87 μm/pixel.

The local heat flux has been numerically calculated from the temperature distributions with a three-dimensional substrate discretization using the finite volume method within the CFD toolbox OpenFOAM.

To determine the drop diameter and impact velocity from the high speed black and white images, an algorithm has been developed and implemented in MATLAB. To minimize the effect of drop oscillation on the evaluation of the drop diameter, the equivalent diameter of the drop is evaluated by a three-dimensional volume integration method. The impact velocity has been obtained by tracking the drop centroid for several images before impact, evaluating the average drop velocity for each time period, fitting a curve to the calculated velocities and finally curve extrapolation.

Similar to previous drop impingement studies on impermeable and moderately superheated surfaces, the drop impingement event has been divided into three subsequent phases: i) the spreading phase, ii) the receding phase, and iii) the sessile drop evaporation phase. It has been concluded that the maximum spreading radii decrease with increasing wall superheat due to the increase of the apparent contact angle caused by an increase of evaporation rate in the proximity of the three-phase contact line. However, the larger drop impact velocities and impact diameters lead to a higher maximum spreading radii, mainly due to the larger kinetic energy of the liquid drop. The global heat flow within the spreading and the receding phases increases with increasing of the wall superheat, drop impact velocity and drop impact diameter. This is attributed to the higher temperature difference between the heater surface and the liquid drop in the case of higher wall superheats and larger drop footprint if the drop impact velocity and drop diameter increase. The experimental results are compared with the numerical model developed in the author's institute. A good qualitative and quantitative agreement between the experimental data and numerical simulations for both contact line radius and heat flow has been observed.

It has been found that an increase in the system pressure prolongs slightly the spreading and significantly the receding phases. Additionally, the drop footprint during the sessile drop evaporation phase becomes slightly smaller. In terms of heat transport, an increase in the system pressure leads to the decrease of the maximum heat flow during the drop spreading phase due to the decrease in the liquid thermal effusivity, and also leads to a significant decrease of the heat flow during the sessile drop evaporation phase due to the decrease of latent heat of vaporization.

It has been shown that the receding phase is suppressed during the drop impact onto a porous surface. Two scenarios depending upon the wall superheat and impact velocity have been identified. Scenario (I) emerges in the low wall superheats and high impact velocities at which the liquid drop penetrates entirely through the pores of the nanofiber mat and reaches the solid

heater surface. Scenario (II) appears at the large wall superheats in which a large amount of vapor is entrapped inside the pores of the nanofiber mat. This scenario occurs at the small impact velocities where the inertia force is not sufficient to expel the generated vapor radially outwards. The vapor inside the nanofiber pores prevents the liquid drop from reaching the solid surface and leads to lower heat flux in this scenario compared to scenario (I). The transition from the scenario (I) to (II) leads to a smaller spreading radius, a lower heat flow and cumulative heat flow, and longer drop evaporation. The results also have confirmed the shift of onset of nucleate boiling towards the higher wall superheats if the surface is covered with nanofiber mat. Thinner nanofiber mats have led to a larger spreading radius, heat flow, and cumulative heat flow transferred through the liquid–solid interface.

The maximum contact line radius and the maximum heat flow after each impact during successive drop impact have been measured to be larger compared to previous impacts. This is mainly due to the larger mass of liquid wetting the heater surface, and thus, the larger footprint of the drop. The second impact is accompanied by a smaller maximal local heat flux than the first impact. This can be explained by the thermal resistance of the liquid between the second drop and the wall, and considering that the heater surface is already pre-cooled by the first drop. The distribution of the wall heat flux during the spreading phase of the second drop has been characterized by the appearance of two thin ring-shaped zones of the high heat flux. The maximum contact line radius and the maximum heat flow for the second impact have been observed to be independent of the drop generation frequency within the studied range.

Concerning the horizontal coalescence of two drops on a smooth, dry, solid substrate, an uprising symmetric central sheet (bump) at the intersection region of the drops has been observed, whereas the untouched regions of the rim have continued to expand. It has been found that the smaller liquid–solid interface, and, accordingly, the shorter cumulative length of the contact line due to drop coalescence reduces the overall heat flow, especially during the sessile drop evaporation phase of the combined drop, in comparison to the non-coalescence case. The maximum heat flow strongly reduces if the distance between the impact locations is decreased. The longer distances between the drops could cause the temporary coalescence of the drops during the advancing and the receding phases, and finally, the formation of two individual sessile drops. It has been concluded that an increase in the time interval between the impacts inclines the bump from the vertical towards the earlier drop, inducing liquid flow on the upper side and towards the opposite side of the earlier drop. However, the transferred heat flow through the liquid–solid interface of the earlier drop is not influenced by the liquid flow.

In conclusion, this study presented detailed knowledge concerning drop–wall and drop–drop interactions, which is crucial for improving spray cooling systems. However, the presented information is not still enough to give recommendations for the spray cooling.

6.2 Outlook

The motivation of the present work is to understand the underlying physics of the spray cooling process. Within the scope of this work, the hydrodynamics and heat transport during the impact of a single drop as well as multiple drops onto a moderately superheated surface are studied. It is required to broaden the investigations to a wider range of wall temperatures, particularly

for multiple drop impingement, and also to develop more analytical and numerical resources to predict the process for all temperature ranges. One of the most challenging situations for which no adequate models are currently available is multiple drop impact under nucleate/transition boiling regimes. For these conditions, available correlations are still highly empirical in the literature.

Additional studies of drop impact can be conducted using more complex fluids such as heterogeneous mixtures and nanofluids.

Configurations such as combined successive and simultaneous drops impinging onto a heater surface provide greater scope for future work. This is considered to be an important contribution to the fundamental understanding of spray cooling processes. Besides, the impact of successive as well as simultaneous drops with various impact parameters onto a heated surface can be studied.

Experimental studies of multiple drop impact with variable surface wettabilities is a topic of interest for many industrial applications.

Bibliography

[1] S. K. Nayak, P. C. Mishra, and S. K. S. Parashar. Influence of spray characteristics on heat flux in dual phase spray impingement cooling of hot surface. *Alexandria Engineering Journal*, 55(3):1995–2004, 2016.

[2] S. Batzdorf. *Heat transfer and evaporation during single drop impingement onto a superheated wall*. PhD thesis, Technische Universität Darmstadt, Darmstadt, 2015. URL http://tuprints.ulb.tu-darmstadt.de/4542/.

[3] S. J. Chen and A. A. Tseng. Spray and jet cooling in steel rolling. *International Journal of Heat and Fluid Flow*, 13(4):358–369, 1992.

[4] M. E. Sawan and M. W. Carbon. A review of spray-cooling and bottom-flooding work for lwr cores. *Nuclear Engineering and Design*, 32(2):191–207, 1975.

[5] J. S. Nelson, T. E. Milner, B. Anvari, B. S. Tanenbaum, S. Kimel, L. O. Svaasand, and S. L. Jacques. Dynamic epidermal cooling during pulsed laser treatment of port-wine stain: A new methodology with preliminary clinical evaluation. *Archives of Dermatology*, 131(6): 695–700, 1995.

[6] D. E. Tilton, D. A. Kearns, and C. L. Tilton. Liquid nitrogen spray cooling of a simulated electronic chip. In *Advances in cryogenic engineering*, pages 1779–1786. Springer, 1994.

[7] A. Gholijani, C. Schlawitschek, T. Gambaryan-Roisman, and P. Stephan. Heat transfer during drop impingement onto a hot wall: The influence of wall superheat, impact velocity, and drop diameter. *International Journal of Heat and Mass Transfer*, 153:119661, 2020.

[8] M. Rein. Phenomena of liquid drop impact on solid and liquid surfaces. *Fluid Dynamics Research*, 12(2):61–93, aug 1993. doi: 10.1016/0169-5983(93)90106-k. URL https://doi.org/10.1016%2F0169-5983%2893%2990106-k.

[9] G. Liang, T. Zhang, Y. Chen, L. Chen, and S. Shen. Two-phase heat transfer of multi-droplet impact on liquid film. *International Journal of Heat and Mass Transfer*, 139:832 – 847, 2019. ISSN 0017-9310. doi: https://doi.org/10.1016/j.ijheatmasstransfer.2019.05.055. URL http://www.sciencedirect.com/science/article/pii/S0017931018361209.

[10] R. Rioboo, C. Tropea, and M. Marengo. Outcomes from a drop impact on solid surfaces. *Atomization and sprays*, 11(2), 2001.

[11] A. L. Yarin. Drop impact dynamics: splashing, spreading, receding, bouncingâ¦. *Annu. Rev. Fluid Mech.*, 38:159–192, 2006.

[12] C.H.R Mundo, M. Sommerfeld, and C. Tropea. Droplet-wall collisions: experimental studies of the deformation and breakup process. *International journal of multiphase flow*, 21(2):151–173, 1995.

[13] I. V. Roisman, A. Lembach, and C. Tropea. Drop splashing induced by target roughness and porosity: The size plays no role. *Advances in Colloid and Interface Science*, 222:615 – 621, 2015. ISSN 0001-8686. doi: https://doi.org/10.1016/j.cis.2015.02.004. URL http://www.sciencedirect.com/science/article/pii/S0001868615000317. Reinhard Miller, Honorary Issue.

[14] J. Breitenbach. *Drop and spray impact onto a hot substrate: Dynamics and heat transfer*. PhD thesis, Technische Universität Darmstadt, Darmstadt, 2018. URL http://tuprints.ulb.tu-darmstadt.de/8097/.

[15] I. V. Roisman, J. Breitenbach, and C. Tropea. Thermal atomisation of a liquid drop after impact onto a hot substrate. *Journal of Fluid Mechanics*, 842:87â101, 2018. doi: 10.1017/jfm.2018.123.

[16] J. Breitenbach, J. Kissing, I. V. Roisman, and C. Tropea. Characterization of secondary droplets during thermal atomization regime. *Experimental Thermal and Fluid Science*, 98:516 – 522, 2018. ISSN 0894-1777. doi: https://doi.org/10.1016/j.expthermflusci.2018.06.030. URL http://www.sciencedirect.com/science/article/pii/S0894177718310495.

[17] A. L. Yarin. Drop impact dynamics: Splashing, spreading, receding, bouncingâ¦. *Annual Review of Fluid Mechanics*, 38(1):159–192, 2006. doi: 10.1146/annurev.fluid.38.050304.092144. URL https://doi.org/10.1146/annurev.fluid.38.050304.092144.

[18] M. Marengo, C. Antonini, I. V. Roisman, and C. Tropea. Drop collisions with simple and complex surfaces. *Current Opinion in Colloid Interface Science*, 16(4):292 – 302, 2011. ISSN 1359-0294. doi: https://doi.org/10.1016/j.cocis.2011.06.009. URL http://www.sciencedirect.com/science/article/pii/S1359029411000859.

[19] A. L. Yarin, I. V. Roisman, and C. Tropea. *Collision phenomena in liquids and solids*. Cambridge University Press, 2017.

[20] J. Fukai, Z. Zhao, D. Poulikakos, C. M. Megaridis, and O. Miyatake. Modeling of the deformation of a liquid droplet impinging upon a flat surface. *Physics of Fluids A: Fluid Dynamics*, 5(11):2588–2599, 1993.

[21] Z. Zhao, D. Poulikakos, and J. Fukai. Heat transfer and fluid dynamics during the collision of a liquid droplet on a substrateâi. modeling. *International Journal of Heat and Mass Transfer*, 39(13):2771–2789, 1996.

[22] H. Y. Erbil. Evaporation of pure liquid sessile and spherical suspended drops: A review. *Advances in Colloid and Interface Science*, 170(1):67 – 86, 2012. ISSN 0001-8686. doi: https://doi.org/10.1016/j.cis.2011.12.006. URL http://www.sciencedirect.com/science/article/pii/S0001868612000036.

[23] C. Josserand and S.T. Thoroddsen. Drop impact on a solid surface. *Annual Review of Fluid Mechanics*, 48(1):365–391, 2016. doi: 10.1146/annurev-fluid-122414-034401. URL https://doi.org/10.1146/annurev-fluid-122414-034401.

[24] S. Herbert, S. Fischer, T. Gambaryan-Roisman, and P. Stephan. Local heat transfer and phase change phenomena during single drop impingement on a hot surface. *International Journal of Heat and Mass Transfer*, 61:605 – 614, 2013. ISSN 0017-9310. doi: https://doi.org/10.1016/j.ijheatmasstransfer.2013.01.081. URL http://www.sciencedirect.com/science/article/pii/S0017931013001129.

[25] S. Herbert, T. Gambaryan-Roisman, and P. Stephan. Influence of the governing dimensionless parameters on heat transfer during single drop impingement onto a hot wall. *Colloids and Surfaces A: Physicochemical and Engineering Aspects*, 432:57 – 63, 2013. ISSN 0927-7757. doi: https://doi.org/10.1016/j.colsurfa.2013.05.014. URL http://www.sciencedirect.com/science/article/pii/S0927775713003932. WETTING AND EVAPORATION: DROPLETS OF PURE AND COMPLEX FLUIDS.

[26] J. Lee, J. Kim, and K. T. Kiger. Time- and space-resolved heat transfer characteristics of single droplet cooling using microscale heater arrays. *International Journal of Heat and Fluid Flow*, 22(2):188 – 200, 2001. ISSN 0142-727X. doi: https://doi.org/10.1016/S0142-727X(00)00082-5. URL http://www.sciencedirect.com/science/article/pii/S0142727X00000825.

[27] C. Sodtke, V.S. Ajaev, and P. Stephan. Evaporation of thin liquid droplets on heated surfaces. *Heat and mass transfer*, 43(7):649–657, 2007.

[28] K. Ibrahem, M.F. Abd Rabbo, T. Gambaryan-Roisman, and P. Stephan. Experimental investigation of evaporative heat transfer characteristics at the 3-phase contact line. *Experimental Thermal and Fluid Science*, 34(8):1036 – 1041, 2010. ISSN 0894-1777. doi: https://doi.org/10.1016/j.expthermflusci.2010.02.014. URL http://www.sciencedirect.com/science/article/pii/S0894177710000622.

[29] C. Höhmann and P. Stephan. Microscale temperature measurement at an evaporating liquid meniscus. *Experimental Thermal and Fluid Science*, 26(2):157 – 162, 2002. ISSN 0894-1777. doi: https://doi.org/10.1016/S0894-1777(02)00122-X. URL http://www.sciencedirect.com/science/article/pii/S089417770200122X.

[30] S. Fischer. *Experimental Investigation of Heat Transfer during Evaporation in the Vicinity of Moving Three-Phase Contact Lines*. PhD thesis, Technische Universität Darmstadt, Darmstadt, March 2015. URL http://tuprints.ulb.tu-darmstadt.de/4396/.

[31] E. Wagner, C. Sodtke, N. Schweizer, and P. Stephan. Experimental study of nucleate boiling heat transfer under low gravity conditions using tlcs for high resolution temperature measurements. *Heat and mass transfer*, 42(10):875–883, 2006.

[32] C. Kunkelmann and P. Stephan. Cfd simulation of boiling flows using the volume-of-fluid method within openfoam. *Numerical Heat Transfer, Part A: Applications*, 56(8):631–646, 2009. doi: 10.1080/10407780903423908. URL https://doi.org/10.1080/10407780903423908.

[33] C. Kunkelmann and P. Stephan. Numerical simulation of the transient heat transfer during nucleate boiling of refrigerant hfe-7100. *International Journal of Refrigeration*, 33(7):1221

– 1228, 2010. ISSN 0140-7007. doi: https://doi.org/10.1016/j.ijrefrig.2010.07.013. URL http://www.sciencedirect.com/science/article/pii/S0140700710001593.

[34] C. Kunkelmann. *Numerical Modeling and Investigation of Boiling Phenomena*. PhD thesis, Technische Universität Darmstadt, Darmstadt, May 2011. URL http://tuprints.ulb.tu-darmstadt.de/2731/.

[35] I. Marchuk, A. Karchevsky, A. Surtaev, and O. Kabov. Heat flux at the surface of metal foil heater under evaporating sessile droplets. *International Journal of Aerospace Engineering*, 2015, 2015.

[36] V.V. Cheverda, A.L. Karchevsky, I.V. Marchuk, and O.A. Kabov. Heat flux density in the region of droplet contact line on a horizontal surface of a thin heated foil. *Thermophysics and Aeromechanics*, 24(5):803–806, 2017.

[37] A.L. Karchevsky, I.V. Marchuk, and O.A. Kabov. Calculation of the heat flux near the liquidâgasâsolid contact line. *Applied Mathematical Modelling*, 40(2):1029 – 1037, 2016. ISSN 0307-904X. doi: https://doi.org/10.1016/j.apm.2015.06.018. URL http://www.sciencedirect.com/science/article/pii/S0307904X15003972.

[38] R. Raj, C. Kunkelmann, P. Stephan, J. Plawsky, and J. Kim. Contact line behavior for a highly wetting fluid under superheated conditions. *International Journal of Heat and Mass Transfer*, 55(9):2664 – 2675, 2012. ISSN 0017-9310. doi: https://doi.org/10.1016/j.ijheatmasstransfer.2011.12.026. URL http://www.sciencedirect.com/science/article/pii/S0017931011007423.

[39] G. Liang, X. Mu, Y. Guo, S. Shen, S. Quan, and J. Zhang. Contact vaporization of an impacting drop on heated surfaces. *Experimental Thermal and Fluid Science*, 74:73 – 80, 2016. ISSN 0894-1777. doi: https://doi.org/10.1016/j.expthermflusci.2015.11.027. URL http://www.sciencedirect.com/science/article/pii/S0894177715003556.

[40] V.E. Nakoryakov, S.Ya. Misyura, and S.L. Elistratov. The behavior of water droplets on the heated surface. *International Journal of Heat and Mass Transfer*, 55(23):6609 – 6617, 2012. ISSN 0017-9310. doi: https://doi.org/10.1016/j.ijheatmasstransfer.2012.06.069. URL http://www.sciencedirect.com/science/article/pii/S0017931012005005.

[41] A.S. Moita and A.L.N. Moreira. Boiling morphology and heat removal of impinging coolant droplets. In *Proceedings of 22nd European conference on liquid atomization and spray systems, ILASS2008, Como Lake, Italy*, 2008.

[42] M. Itaru and M. Kunihide. Heat transfer characteristics of evaporation of a liquid droplet on heated surfaces. *International Journal of Heat and Mass Transfer*, 21(5):605 – 613, 1978. ISSN 0017-9310. doi: https://doi.org/10.1016/0017-9310(78)90057-1. URL http://www.sciencedirect.com/science/article/pii/0017931078900571.

[43] S. Chandra and C.T. Avedisian. On the collision of a droplet with a solid surface. *Proceedings of the Royal Society of London. Series A: Mathematical and Physical Sciences*, 432 (1884):13–41, 1991.

[44] P. Tartarini, G. Lorenzini, and M. R. Randi. Experimental study of water droplet boiling on hot, non-porous surfaces. *Heat and Mass Transfer*, 34(6):437–447, January 1999. doi: 10.1007/s002310050280.

[45] M. Abu-Zaid. An experimental study of the evaporation characteristics of emulsified liquid droplets. *Heat and mass transfer*, 40(9):737–741, 2004.

[46] I. Buchmüller. *Influence of pressure on Leidenfrost effect*. PhD thesis, Technische Universität Darmstadt, Darmstadt, May 2014. URL http://tuprints.ulb.tu-darmstadt.de/4072/.

[47] J. Breitenbach, I. V. Roisman, and C. Tropea. Drop collision with a hot, dry solid substrate: Heat transfer during nucleate boiling. *Physical Review Fluids*, 2(7):074301, 2017.

[48] S.W. Akhtar, G. G. Nasr, and A. J. Yule. Characteristics of water droplet impaction behavior on a polished steel heated surface: Part i. *Atomization and Sprays*, 17(8), 2007.

[49] N. Nikolopoulos, A. Theodorakakos, and G. Bergeles. A numerical investigation of the evaporation process of a liquid droplet impinging onto a hot substrate. *International Journal of Heat and Mass Transfer*, 50(1):303 – 319, 2007. ISSN 0017-9310. doi: https://doi.org/10.1016/j.ijheatmasstransfer.2006.06.012. URL http://www.sciencedirect.com/science/article/pii/S0017931006003644.

[50] J. G. Leidenfrost. On the fixation of water in diverse fire. *International Journal of Heat and Mass Transfer*, 9(11):1153 – 1166, 1966. ISSN 0017-9310. doi: https://doi.org/10.1016/0017-9310(66)90111-6. URL http://www.sciencedirect.com/science/article/pii/0017931066901116.

[51] B.S. Gottfried, C.J. Lee, and K.J. Bell. The leidenfrost phenomenon: film boiling of liquid droplets on a flat plate. *International Journal of Heat and Mass Transfer*, 9(11):1167 – 1188, 1966. ISSN 0017-9310. doi: https://doi.org/10.1016/0017-9310(66)90112-8. URL http://www.sciencedirect.com/science/article/pii/0017931066901128.

[52] J. D. Bernardin and I. Mudawar. The Leidenfrost Point: Experimental Study and Assessment of Existing Models. *Journal of Heat Transfer*, 121(4):894–903, 11 1999. ISSN 0022-1481. doi: 10.1115/1.2826080. URL https://doi.org/10.1115/1.2826080.

[53] P. Testa and L. Nicotra. Influence of Pressure on the Leidenfrost Temperature and on Extracted Heat Fluxes in the Transient Mode and Low Pressure. *Journal of Heat Transfer*, 108(4):916–921, 11 1986. ISSN 0022-1481. doi: 10.1115/1.3247034. URL https://doi.org/10.1115/1.3247034.

[54] F. Celestini, T. Frisch, and Y. Pomeau. Room temperature water leidenfrost droplets. *Soft Matter*, 9:9535–9538, 2013. doi: 10.1039/C3SM51608C. URL http://dx.doi.org/10.1039/C3SM51608C.

[55] D. Chatzikyriakou, S.P. Walker, C.P. Hale, and G.F. Hewitt. The measurement of heat transfer from hot surfaces to non-wetting droplets. *International Journal of Heat and Mass Transfer*, 54(7):1432 – 1440, 2011. ISSN 0017-9310. doi: https:

//doi.org/10.1016/j.ijheatmasstransfer.2010.11.051. URL http://www.sciencedirect.com/science/article/pii/S0017931010006769.

[56] J. B. Schmidt, J. Breitenbach, I. V. Roisman, and C. Tropea. Measurement of the heat flux during a drop impact onto a hot dry solid surface using infrared thermal imaging. In *Symposium der Deutsche Gesellschaft für Luft-und Raumfahrt*, pages 553–562. Springer, 2018.

[57] J. Breitenbach, I. V. Roisman, and C. Tropea. Heat transfer in the film boiling regime: Single drop impact and spray cooling. *International Journal of Heat and Mass Transfer*, 110:34 – 42, 2017. ISSN 0017-9310. doi: https://doi.org/10.1016/j.ijheatmasstransfer.2017.03.004. URL http://www.sciencedirect.com/science/article/pii/S0017931016338352.

[58] M. Pasandideh-Fard, Y.M. Qiao, S. Chandra, and J. Mostaghimi. Capillary effects during droplet impact on a solid surface. *Physics of fluids*, 8(3):650–659, 1996.

[59] Y. Guo, S. Shen, and S. Quan. Numerical simulation of dynamics of droplet impact on heated flat solid surface. *International Journal of Low-Carbon Technologies*, 8(2):134–139, 04 2012. ISSN 1748-1317. doi: 10.1093/ijlct/cts010. URL https://doi.org/10.1093/ijlct/cts010.

[60] R.G. Picknett and R. Bexon. The evaporation of sessile or pendant drops in still air. *Journal of Colloid and Interface Science*, 61(2):336 – 350, 1977. ISSN 0021-9797. doi: https://doi.org/10.1016/0021-9797(77)90396-4. URL http://www.sciencedirect.com/science/article/pii/0021979777903964.

[61] S. Cioulachtjian, S. Launay, S. Boddaert, and M. Lallemand. Experimental investigation of water drop evaporation under moist air or saturated vapour conditions. *International Journal of Thermal Sciences*, 49(6):859 – 866, 2010. ISSN 1290-0729. doi: https://doi.org/10.1016/j.ijthermalsci.2009.12.014. URL http://www.sciencedirect.com/science/article/pii/S1290072910000050.

[62] L. Xu, W. W. Zhang, and S. R. Nagel. Drop splashing on a dry smooth surface. *Physical review letters*, 94(18):184505, 2005.

[63] J. Liu, H. Vu, S. S. Yoon, R. A. Jepsen, and G. Aguilar. Splashing phenomena during liquid droplet impact. *Atomization and Sprays*, 20(4), 2010.

[64] B.R. Mitchell, T.E. Bate, J.C. Klewicki, Y.P. Korkolis, and B.L. Kinsey. Experimental investigation of droplet impact on metal surfaces in reduced ambient pressure. *Procedia Manufacturing*, 10:730–736, 2017.

[65] K.C. Hsieh, J.S. Shuen, and V. Yang. Droplet vaporization in high-pressure environments i: Near critical conditions. *Combustion Science and Technology*, 76(1-3):111–132, 1991.

[66] H. Ghassemi, S. Wook Baek, and Q. S. Khan. Experimental study on evaporation of kerosene droplets at elevated pressures and temperatures. *Combustion science and technology*, 178(9):1669–1684, 2006.

[67] H. Kim and N. Sung. The effect of ambient pressure on the evaporation of a single droplet and a spray. *Combustion and Flame*, 135(3):261–270, 2003.

[68] C. Schlawitschek. *Numerical simulation of drop impact and evaporation on superheated surfaces at low and high ambient pressures*. PhD thesis, Technische Universität Darmstadt, Darmstadt, 2020. URL http://tuprints.ulb.tu-darmstadt.de/11800/.

[69] N. Schweizer. *Multi-Scale Investigation of Nucleate Boiling Phenomena in Microgravity*. PhD thesis, Technische Universität Darmstadt, Darmstadt, December 2010. URL http://tuprints.ulb.tu-darmstadt.de/3261/.

[70] G. Guggilla, A. Pattamatta, and R. Narayanaswamy. Numerical investigation into the evaporation dynamics of drop-on-drop collisions over heated wetting surfaces. *International Journal of Heat and Mass Transfer*, 123:1050 – 1067, 2018. ISSN 0017-9310. doi: https://doi.org/10.1016/j.ijheatmasstransfer.2018.03.029. URL http://www.sciencedirect.com/science/article/pii/S0017931017351505.

[71] G. Guggilla, R. Narayanaswamy, and A. Pattamatta. An experimental investigation into the spread and heat transfer dynamics of a train of two concentric impinging droplets over a heated surface. *Experimental Thermal and Fluid Science*, 110:109916, 2020. ISSN 0894-1777. doi: https://doi.org/10.1016/j.expthermflusci.2019.109916. URL http://www.sciencedirect.com/science/article/pii/S0894177719304984.

[72] Azar Alizadeh, Vaibhav Bahadur, Sheng Zhong, Wen Shang, Ri Li, James Ruud, Masako Yamada, Liehui Ge, Ali Dhinojwala, and Manohar Sohal. Temperature dependent droplet impact dynamics on flat and textured surfaces. *Applied physics letters*, 100(11):111601, 2012.

[73] El-Sayed R. Negeed, S. Hidaka, M. Kohno, and Y. Takata. Effect of the surface roughness and oxidation layer on the dynamic behavior of micrometric single water droplets impacting onto heated surfaces. *International Journal of Thermal Sciences*, 70:65–82, 2013. ISSN 1290-0729. doi: https://doi.org/10.1016/j.ijthermalsci.2013.03.004. URL https://www.sciencedirect.com/science/article/pii/S1290072913000483.

[74] R. Srikar, T. Gambaryan-Roisman, C. Steffes, P. Stephan, C. Tropea, and A.L. Yarin. Nanofiber coating of surfaces for intensification of drop or spray impact cooling. *International Journal of Heat and Mass Transfer*, 52(25-26):5814–5826, 2009.

[75] C. M. Weickgenannt, Y. Zhang, A. N. Lembach, I. V. Roisman, T. Gambaryan-Roisman, A. L. Yarin, and C. Tropea. Nonisothermal drop impact and evaporation on polymer nanofiber mats. *Physical Review E*, 83(3):036305, 2011.

[76] C. M. Weickgenannt, Y. Zhang, S. Sinha-Ray, I. V. Roisman, T. Gambaryan-Roisman, C. Tropea, and A. L. Yarin. Inverse-leidenfrost phenomenon on nanofiber mats on hot surfaces. *Physical Review E*, 84(3):036310, 2011.

[77] S. Sinha-Ray, Y. Zhang, and A.L. Yarin. Thorny devil nanotextured fibers: the way to cooling rates on the order of 1 kw/cm2. *Langmuir*, 27(1):215–226, 2011.

[78] S. Sinha-Ray and A. L. Yarin. Drop impact cooling enhancement on nano-textured surfaces. part i: Theory and results of the ground (1 g) experiments. *International Journal of Heat and Mass Transfer*, 70:1095–1106, 2014.

[79] S. Sinha-Ray, S. Sinha-Ray, A. L. Yarin, C. M. Weickgenannt, J. Emmert, and C. Tropea. Drop impact cooling enhancement on nano-textured surfaces. part ii: Results of the parabolic flight experiments [zero gravity (0g) and supergravity (1.8 g)]. *International Journal of Heat and Mass Transfer*, 70:1107–1114, 2014.

[80] C.T. Avedisian and J. Koplik. Leidenfrost boiling of methanol droplets on hot porous/ceramic surfaces. *International Journal of Heat and Mass Transfer*, 30(2):379 – 393, 1987. ISSN 0017-9310. doi: https://doi.org/10.1016/0017-9310(87)90126-8. URL http://www.sciencedirect.com/science/article/pii/0017931087901268.

[81] G. Liang, T. Zhang, H. Yu, H. Chen, and S. Shen. Simultaneous impact of multiple droplets on liquid film. *Journal of industrial and engineering chemistry*, 65:51–61, 2018.

[82] G. Liang, T. Zhang, L. Chen, Y. Chen, and S. Shen. Single-phase heat transfer of multi-droplet impact on liquid film. *International Journal of Heat and Mass Transfer*, 132:288 – 292, 2019. ISSN 0017-9310. doi: https://doi.org/10.1016/j.ijheatmasstransfer.2018.11.145. URL http://www.sciencedirect.com/science/article/pii/S0017931018343783.

[83] G. Liang, T. Zhang, H. Chen, H. Yu, and S. Shen. Successive impact of multiple droplets on liquid film. *European Journal of Mechanics - B/Fluids*, 74:389 – 398, 2019. ISSN 0997-7546. doi: https://doi.org/10.1016/j.euromechflu.2018.09.011. URL http://www.sciencedirect.com/science/article/pii/S0997754618303790.

[84] H. Fujimoto, T. Ogino, H. Takuda, and N. Hatta. Collision of a droplet with a hemispherical static droplet on a solid. *International Journal of Multiphase Flow*, 27(7):1227 – 1245, 2001. ISSN 0301-9322. doi: https://doi.org/10.1016/S0301-9322(00)00075-6. URL http://www.sciencedirect.com/science/article/pii/S0301932200000756.

[85] H. Fujimoto, S. Ito, and I. Takezaki. Experimental study of successive collision of two water droplets with a solid. *Experiments in fluids*, 33(3):500–502, 2002.

[86] H. Fujimoto, I. Takezaki, Y. Shiotani, A. Tong, and H. Takuda. Collision dynamics of two droplets impinging successively onto a hot solid. *ISIJ International*, 44(6):1049–1056, 2004. doi: 10.2355/isijinternational.44.1049.

[87] H. Fujimoto, A. Y. Tong, and H. Takuda. Interaction phenomena of two water droplets successively impacting onto a solid surface. *International Journal of Thermal Sciences*, 47(3):229 – 236, 2008. ISSN 1290-0729. doi: https://doi.org/10.1016/j.ijthermalsci.2007.02.006. URL http://www.sciencedirect.com/science/article/pii/S1290072907000701.

[88] T. Minamikawa, H.i Fujimoto, T. Hama, and H. Takuda. Numerical simulation of two droplets impinging successively on a hot solid in the film boiling regime. *ISIJ International*, 48(5):611–615, 2008. doi: 10.2355/isijinternational.48.611.

[89] I. V. Roisman, B. Prunet-Foch, C. Tropea, and M. Vignes-Adler. Multiple drop impact onto a dry solid substrate. *Journal of colloid and interface science*, 256(2):396–410, 2002.

[90] K. A. Raman, R. K. Jaiman, T. S. Lee, and H. T. Low. Dynamics of simultaneously impinging drops on a dry surface: Role of impact velocity and air inertia. *Journal of colloid and interface science*, 486:265–276, 2017.

[91] S. Batzdorf, J. Breitenbach, C. Schlawitschek, I. V. Roisman, C. Tropea, P. Stephan, and T. Gambaryan-Roisman. Heat transfer during simultaneous impact of two drops onto a hot solid substrate. *International Journal of Heat and Mass Transfer*, 113:898 – 907, 2017. ISSN 0017-9310. doi: https://doi.org/10.1016/j.ijheatmasstransfer.2017.05.091. URL http://www.sciencedirect.com/science/article/pii/S0017931017304635.

[92] G. Liang and I. Mudawar. Review of drop impact on heated walls. *International Journal of Heat and Mass Transfer*, 106:103–126, 2017.

[93] S. Herbert, S. Fischer, T. Gambaryan-Roisman, and P. Stephan. Local heat transfer and phase change phenomena during single drop impingement on a hot surface. *International Journal of Heat and Mass Transfer*, 61:605–614, 2013.

[94] R. Nasarek. *Temperature Field Measurements with High Spatial and Temporal Resolution Using Liquid Crystal Thermography and Laser Induced Fluorescence*. PhD thesis, Technische Universität Darmstadt, Darmstadt, March 2010. URL http://tuprints.ulb.tu-darmstadt.de/2096/.

[95] JP Crimaldi. The effect of photobleaching and velocity fluctuations on single-point lif measurements. *Experiments in Fluids*, 23(4):325–330, 1997.

[96] LG Larsen and JP Crimaldi. The effect of photobleaching on plif. *Experiments in fluids*, 41 (5):803–812, 2006.

[97] Christoph Höhmann. *Temperaturmessverfahren zur räumlich hochauflösenden Untersuchung des Wärmetransports an einem verdampfenden Flüssigkeitsmeniskus*. PhD thesis, Technische Universität Darmstadt, Darmstadt, 2004.

[98] *Material data Calcium Fluoride*. Korth Kristalle GmbH, 2014.

[99] Liquid nitrogen spray cooling of a simulated electronic chip. In *Thermodynamic Properties of Pure Metals and Metal Alloys, VDI Heat Atlas*, pages 551–565. Springer, 2010.

[100] E. M. Slomski. *Funktionsorientierte Mikrostrukturierung von Chromnitrid-Beschichtungen mittels hybrider PVD-Technologie*. PhD thesis, TU Darmstadt, Aachen, 2013. URL http://tubiblio.ulb.tu-darmstadt.de/63086/. Zugl.: Darmstadt, Techn. Univ., Diss., 2013.

[101] N. Otsu. A threshold selection method from gray-level histograms. *IEEE transactions on systems, man, and cybernetics*, 9(1):62–66, 1979.

[102] Lisong Yang, Bethany K Kazmierski, Stephen D Hoath, Sungjune Jung, Wen-Kai Hsiao, Yi-wei Wang, Arganthaël Berson, Oliver Harlen, Nik Kapur, and Colin D Bain. Determination

of dynamic surface tension and viscosity of non-newtonian fluids from drop oscillations. *Physics of Fluids*, 26(11):113103, 2014.

[103] C. Tropea and A. L. Yarin. *Springer handbook of experimental fluid mechanics*. Springer Science & Business Media, 2007.

[104] AB FLIR. The ultimate infrared handbook for r&d professionals. *Boston: FLIR Systems*, 2010.

[105] H. C. Hottel and A. F. Sarofim. *Radiative transfer*. McGraw-Hill, 1967.

[106] M. Peralta. *Propagation Of Errors: How To Mathematically Predict Measurement Errors*. Createspace Independent Publishing Platform, United States, 2012.

[107] J. R. Taylor. *Fehleranalyse : eine EinfÃ¼hrung in die Untersuchung von Unsicherheiten in physikalischen Messungen*. Weinheim ; Basel (Schweiz) ; Cambridge ; New York, NY : VCH, 1988.

[108] M. Potash and P.C. Wayner. Evaporation from a two-dimensional extended meniscus. *International Journal of Heat and Mass Transfer*, 15(10):1851–1863, 1972.

[109] P.C. Stephan and C.A. Busse. Analysis of the heat transfer coefficient of grooved heat pipe evaporator walls. *International Journal of heat and mass transfer*, 35(2):383–391, 1992.

[110] F.J. Renk and P.C. Wayner. An evaporating ethanol meniscusâpart ii: Analytical studies. 1979.

[111] S. Moosman and G.M.. Homsy. Evaporating menisci of wetting fluids. *Journal of Colloid and Interface Science*, 73(1):212–223, 1980.

[112] F.W. Holm and S.P. Goplen. Heat transfer in the meniscus thin-film transition region. 1979.

[113] C. W. Hirt and B. D. Nichols. Volume of fluid (vof) method for the dynamics of free boundaries. *Journal of computational physics*, 39(1):201–225, 1981.

[114] M Heinz, P Stephan, and T Gambaryan-Roisman. Influence of nanofiber coating thickness and drop volume on spreading, imbibition, and evaporation. *Colloids and Surfaces A: Physicochemical and Engineering Aspects*, 631:127450, 2021.

[115] A. Gholijani, T. Gambaryan-Roisman, and P. Stephan. Experimental investigation of hydrodynamics and heat transport during drop impact onto a heated wall covered with an electrospun nanofiber mat: The influence of wall superheat, impact velocity, and mat thickness. *Experimental Thermal and Fluid Science*, 118:110145, 2020.

[116] N. Sabetzadeh, H. Bahrambeygi, A. Rabbi, and K. Nasouri. Thermal conductivity of polyacrylonitrile nanofibre web in various nanofibre diameters and surface densities. *Micro & Nano Letters*, 7(7):662–666, 2012.

[117] G Martic, TD Blake, and J De Coninck. Dynamics of imbibition into a pore with a heterogeneous surface. *Langmuir*, 21(24):11201–11207, 2005.

[118] R. P. Sahu, S. Sinha-Ray, S. Sinha-Ray, and A. L. Yarin. Pool boiling on nano-textured surfaces comprised of electrically-assisted supersonically solution-blown, copper-plated nanofibers: experiments and theory. *International Journal of Heat and Mass Transfer*, 87: 521–535, 2015.

[119] R. P. Sahu, S. Sinha-Ray, A.L. Yarin, and B. Pourdeyhimi. Drop impacts on electrospun nanofiber membranes. *Soft Matter*, 8(14):3957–3970, 2012.

[120] A. Gholijani, T. Gambaryan-Roisman, and P. Stephan. Experimental investigation of hydrodynamics and heat transport during vertical coalescence of multiple successive drops impacting a hot wall under saturated vapor atmosphere. *Experimental Thermal and Fluid Science*, 118:110145, 2020.

[121] A. Gholijani, T. Gambaryan-Roisman, and P. Stephan. Experimental investigation of hydrodynamics and heat transport during horizontal coalescence of two drops impinging a hot wal. *Experimental Thermal and Fluid Science*, 131:110520, 2022.

A Annex

A.1 Material properties

Table A.1.: Properties of CaF_2

property	value
ρ / kg m^{-3}	3180
c / J kg^{-1} K^{-1}	854
k / W m^{-1} K^{-1}	9.71

Table A.2.: General properties of FC-72

property	
coefficient of expansion / °C^{-1}	0.00156
averaged molecular weight / g mol^{-1}	338
refractive index	1.25
appearance	clear, colorless
flash point	none
toxicity	none
flammability	none

Table A.3.: Properties of FC-72 at various temperatures.

P	T	α	c_p	h_{fg}	k	μ	ν	Pr	ρ_f	ρ_g	σ
		$\cdot 10^{+8}$			$\cdot 10^{+2}$	$\cdot 10^{+4}$	$\cdot 10^{+7}$				$\cdot 10^{+2}$
atm	° C	m^2s^{-1}	$Jkg^{-1}K^{-1}$	Jkg^{-1}	W m^{-1} K^{-1}	Ns m^{-2}	m^2s^{-1}		kg m^{-3}	kg m^{-3}	N m^{-1}
	5	3.29	1019	98000	5.820	8.70	5.03	15.31	1738	1.80	1.29
0.14	10	3.26	1027	96818	5.760	8.00	4.65	14.26	1720	2.23	1.24
	15	3.23	1034	95593	5.700	7.40	4.36	13.48	1706	2.86	1.20
0.23	20	3.20	1042	94369	5.640	6.90	4.06	12.68	1692	3.48	1.15
	25	3.17	1050	93094	5.590	6.40	3.83	12.10	1680	4.36	1.10
0.36	30	3.13	1057	91820	5.530	6.00	3.60	11.50	1669	5.23	1.06
	35	3.09	1065	90497	5.470	5.70	3.42	11.06	1659	6.41	1.02
0.54	40	3.06	1073	89174	5.410	5.40	3.25	10.62	1650	7.59	0.97
	45	3.02	1081	87789	5.350	5.10	3.10	10.28	1641	9.14	0.93
0.79	50	2.98	1088	86404	5.290	4.80	2.96	9.93	1631	10.68	0.88
	55	2.94	1096	84970	5.230	4.60	2.84	9.65	1623	12.74	0.84
1	56.6	2.93	1098	84511	5.220	4.50	2.80	9.56	1620	13.40	0.83
1.11	60	2.91	1104	83536	5.180	4.40	2.72	9.36	1614	14.79	0.80
	65	2.87	1111	82046	5.120	4.20	2.61	9.09	1603	17.52	0.76
1.53	70	2.84	1119	80557	5.060	4.00	2.50	8.81	1593	20.24	0.72
	75	2.81	1127	79024	5.000	3.80	2.40	8.56	1581	23.72	0.67
2.06	80	2.78	1135	77492	4.940	3.60	2.31	8.31	1569	27.20	0.63
	85	2.75	1142	75928	4.880	3.40	2.21	8.03	1554	31.59	0.59
2.73	90	2.73	1150	74365	4.830	3.30	2.11	7.74	1539	35.98	0.55
	95	2.71	1158	72783	4.770	3.20	2.10	7.76	1520	41.49	0.51
3.54	100	2.69	1165	71201	4.710	3.10	2.09	7.77	1501	47.00	0.48
	105	2.68	1173	69447	4.650	3.10	2.09	7.78	1477	53.81	0.44
4.53	110	2.68	1181	67693	4.590	3.00	2.08	7.79	1453	60.63	0.40
	115	2.68	1189	65994	4.530	3.00	2.08	7.77	1424	69.06	0.37
5.71	120	2.68	1196	64295	4.480	2.90	2.08	7.75	1394	77.50	0.33
	125	2.70	1204	62215	4.420	2.80	2.08	7.69	1357	88.02	0.29
7.12	130	2.72	1212	60134	4.360	2.70	2.08	7.62	1321	98.55	0.26
	135	2.76	1220	57642	4.300	2.70	2.08	7.51	1277	112.07	0.23
8.77	140	2.80	1227	55149	4.240	2.60	2.07	7.40	1233	125.59	0.20
	145	2.87	1235	52059	4.180	2.50	2.07	7.22	1180	143.82	0.16
10.71	150	2.94	1243	48969	4.130	2.30	2.07	7.04	1128	162.04	0.13
	155	3.05	1250	45049	4.070	2.20	2.07	6.79	1065	188.63	0.11
12.96	160	3.18	1258	41128	4.010	2.10	2.07	6.52	1003	215.22	0.08
	165	3.35	1266	35693	3.950	1.90	2.07	6.17	930	259.18	0.05
15.58	170	3.56	1274	30258	3.890	1.80	2.07	5.81	858	303.14	0.03
	175	4.19	1281	12459	3.830	1.50	2.07	4.94	714	485.12	0.01
18.17	178.5	4.80	1287	0	3.790	1.30	2.07	4.31	614	612.50	0

A.2 Exploded and sectional views of the test cell

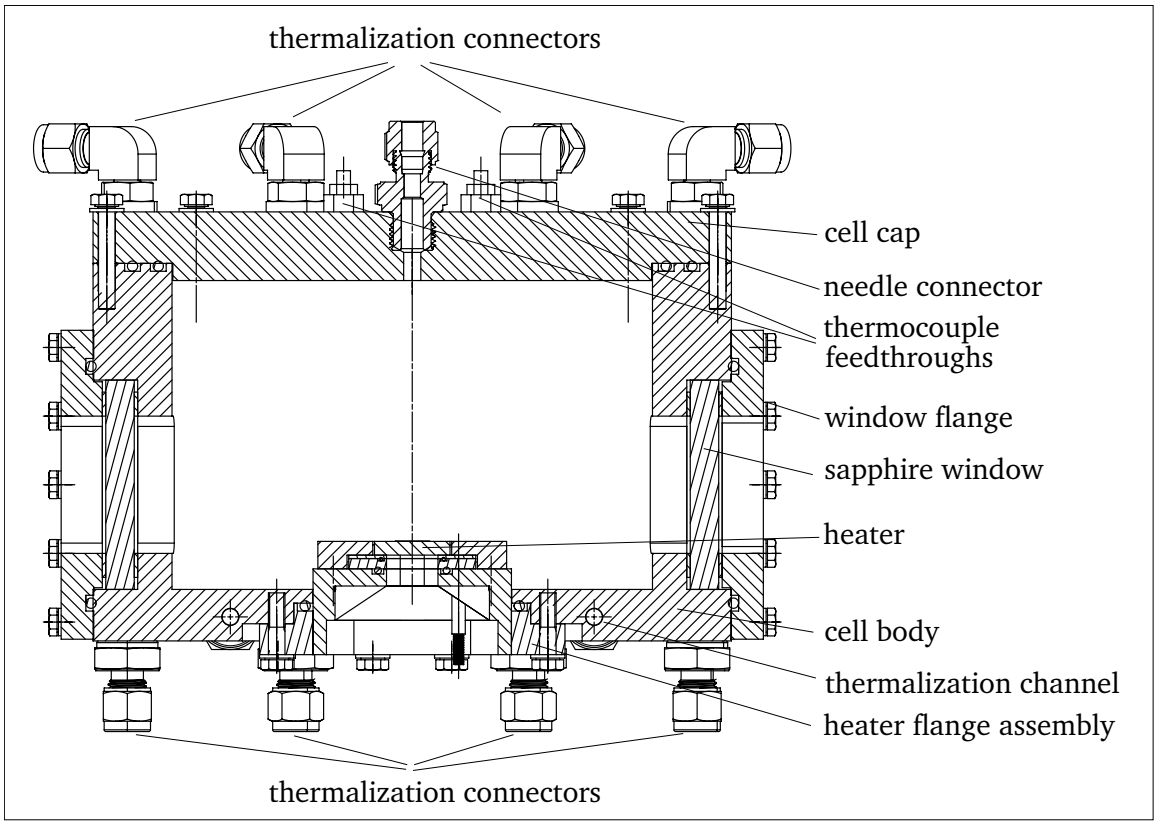

Figure A.1.: Sectional view of the experimental cell

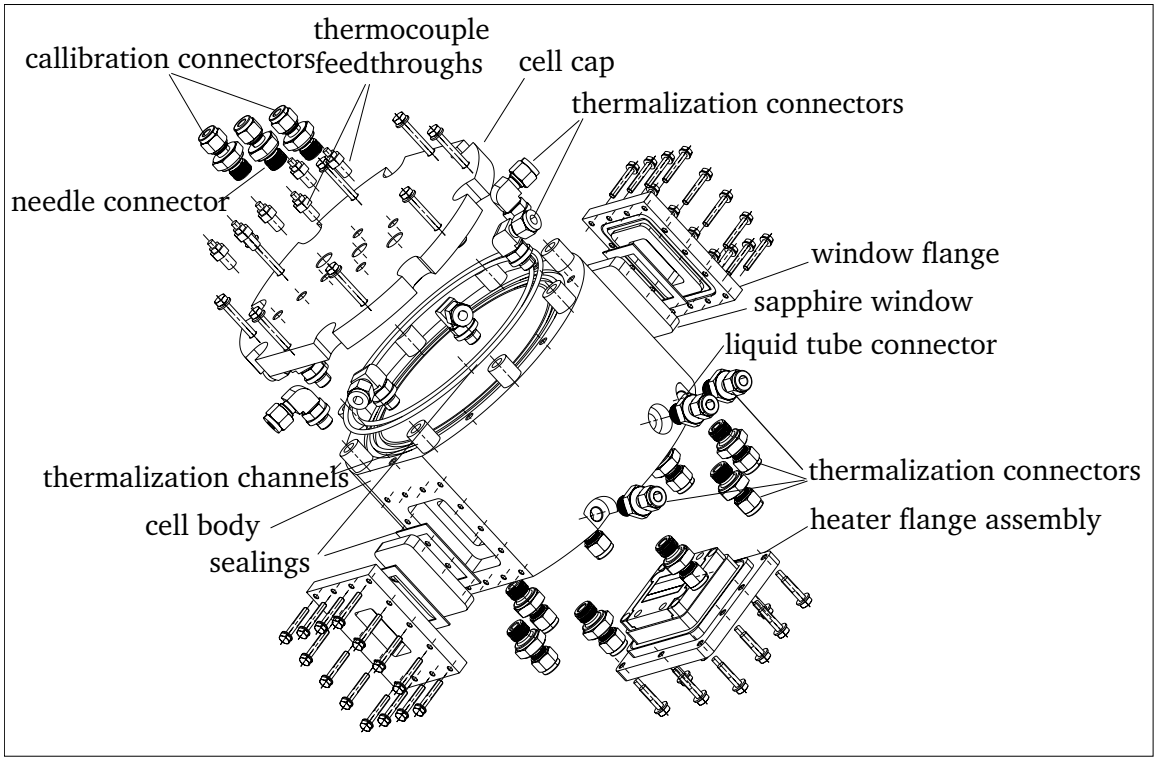

Figure A.2.: Exploaded view of the experimental cell

A.3 Full mass spectra of degassed and non-degassed FC-72

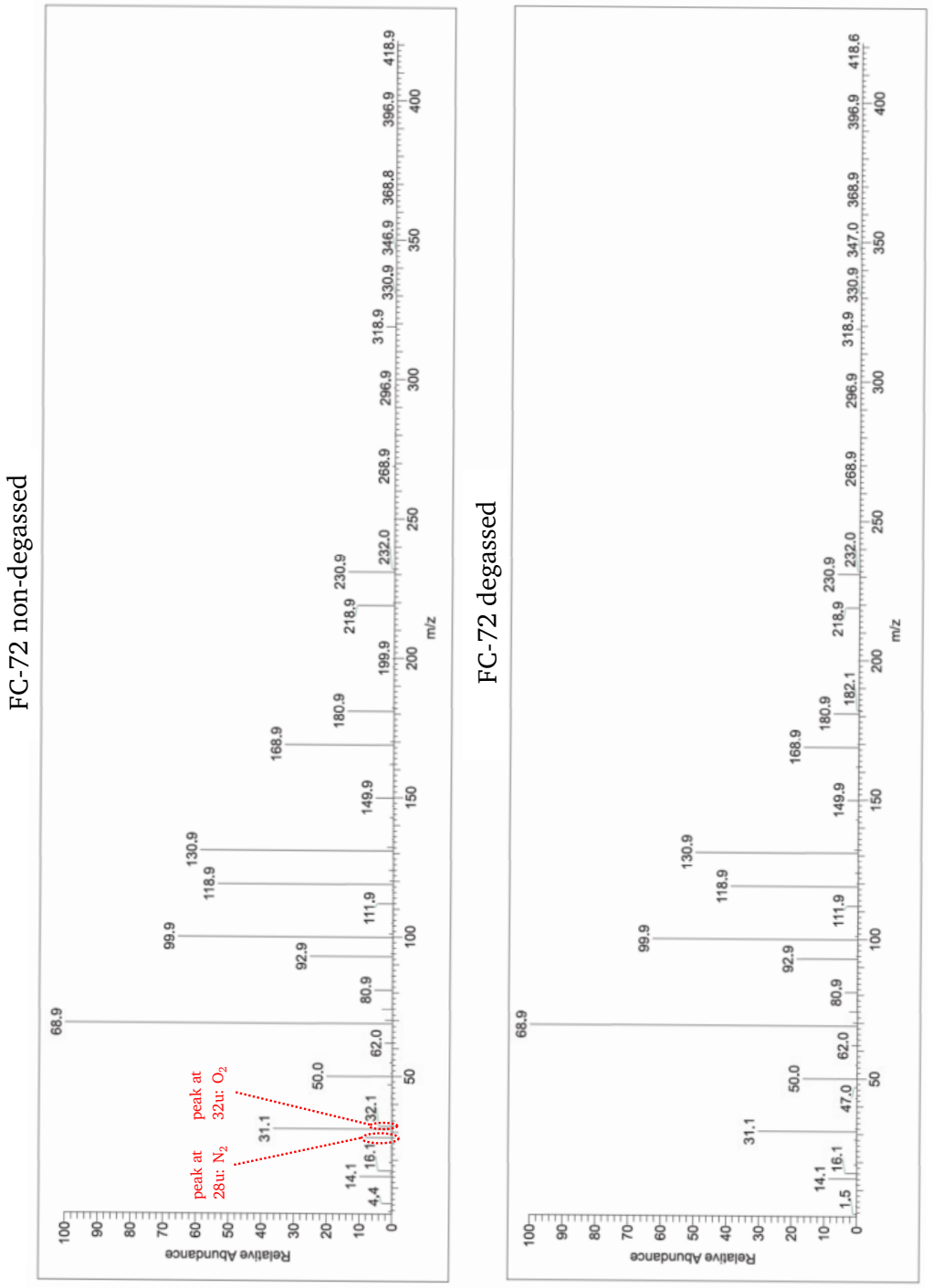

Figure A.3.: Mass spectra from the gas chromatography-mass spectrometry (GC-MS) of a non-degassed FC-72 sample (left) and a degassed FC-72 sample (right) [30].

In the spectrum of non-degassed sample (Fig. A.3, left) peaks are evident at a mass-to-charge ratio of 28u and 32u, indicating the presence of nitrogen (N_2) and oxygen (O_2), respectively. In the spectrum of the degassed sample (Fig. A.3, right), the corresponding peaks for N_2 and O_2 are extremely reduced, indicating a reduction of non-condensable gas content. This suggests a very high quality of the implemented degassing procedure.

A.4 Supplementary figures for each influencing parameter

A.4.1 Single drop impact

Influence of impact velocity during the impingement of a single drop onto a bare heater:

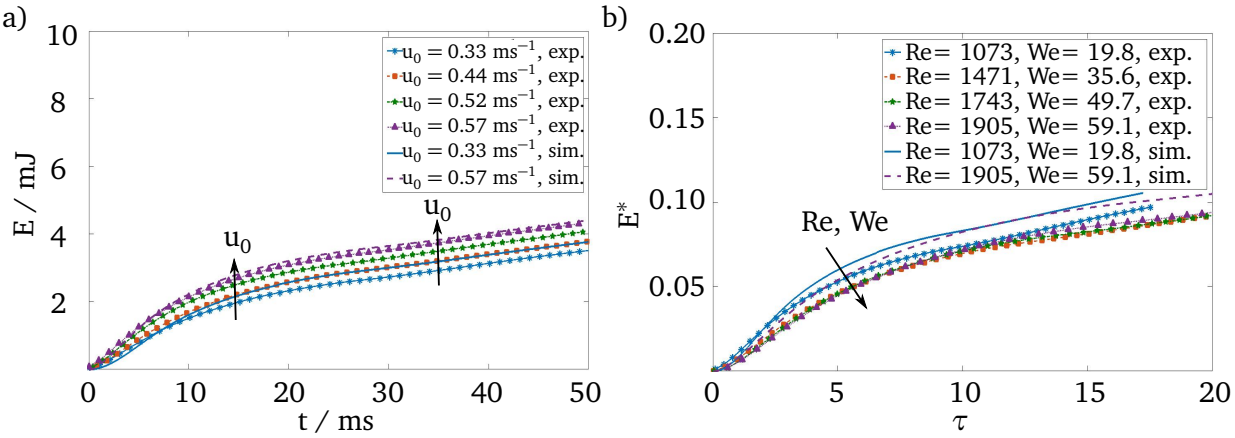

Figure A.4.: Temporal evolution of the cumulative heat flow in a) dimensiona and b) dimensionless forms during the impingement of a single drop onto a bare heater for various impact velocities (D_0 = 0.93 mm, ΔT = 6.3 K, p= 0.9 bar, Ja= 0.08, Bo= 0.4, Pr= 9.7, and $p_R = 0.05$).

Influence of drop size during the impingement of a single drop onto a bare heater:

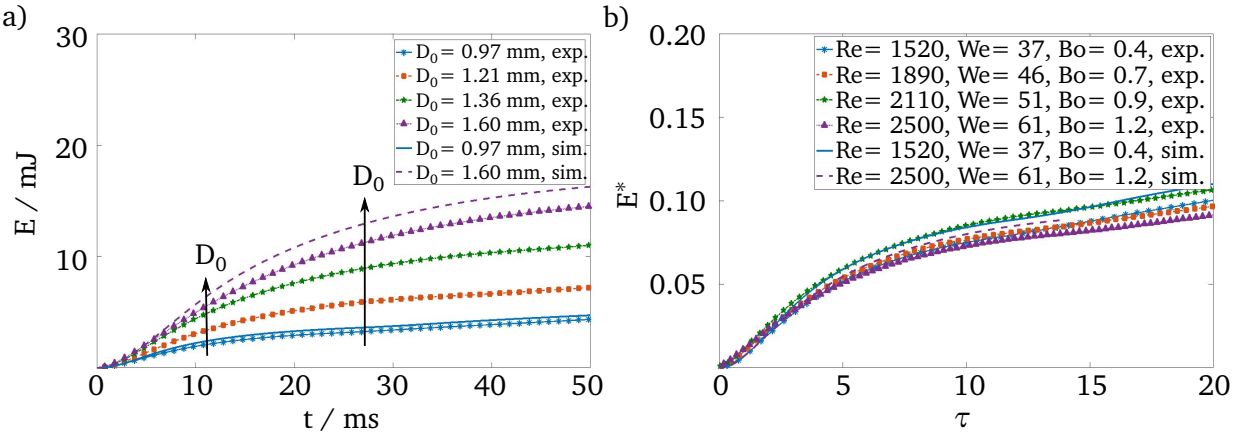

Figure A.5.: Temporal evolution of the cumulative heat flow in a) dimensional and b) dimensionless forms during the impingement of a single drop onto a bare heater for various impact diameters (u_0 = 0.44 m s^{-1}, ΔT = 6.9 K, p= 0.9, Ja= 0.08, Pr= 9.7, and $p_R = 0.05$).

Influence of system pressure during the impingement of a single drop onto a bare heater:

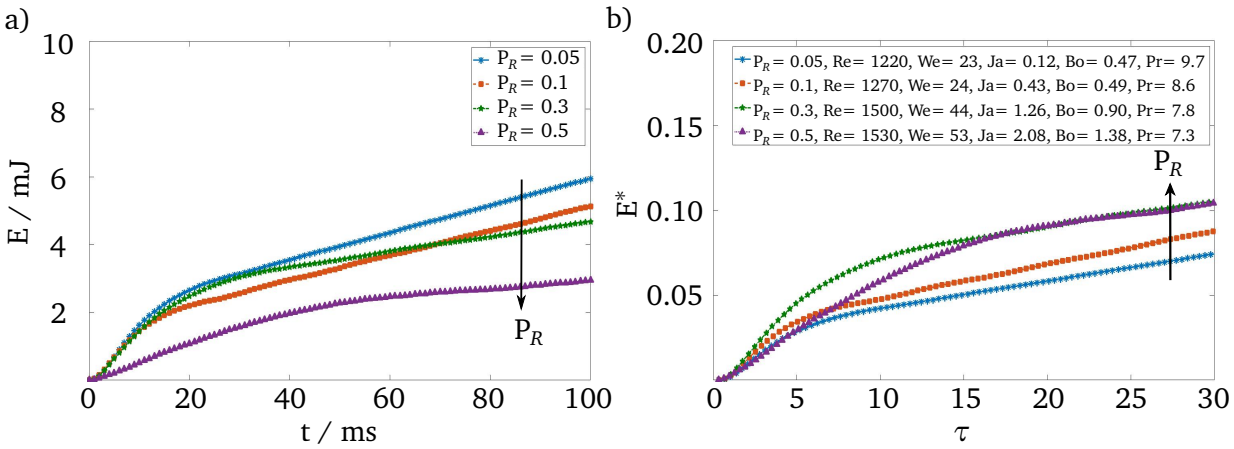

Figure A.6.: Temporal evolution of the cumulative heat flow in a) dimensional and b) dimensionless forms during the impingement of a single drop onto a bare heater for various system pressures ($D_0 = 0.94$ mm, $u_0 = 0.34$ m s^{-1}, and $\Delta T = 6.5$ K).

Influence of surface porosity during the impingement of a single drop onto a nanofiber-coated heater:

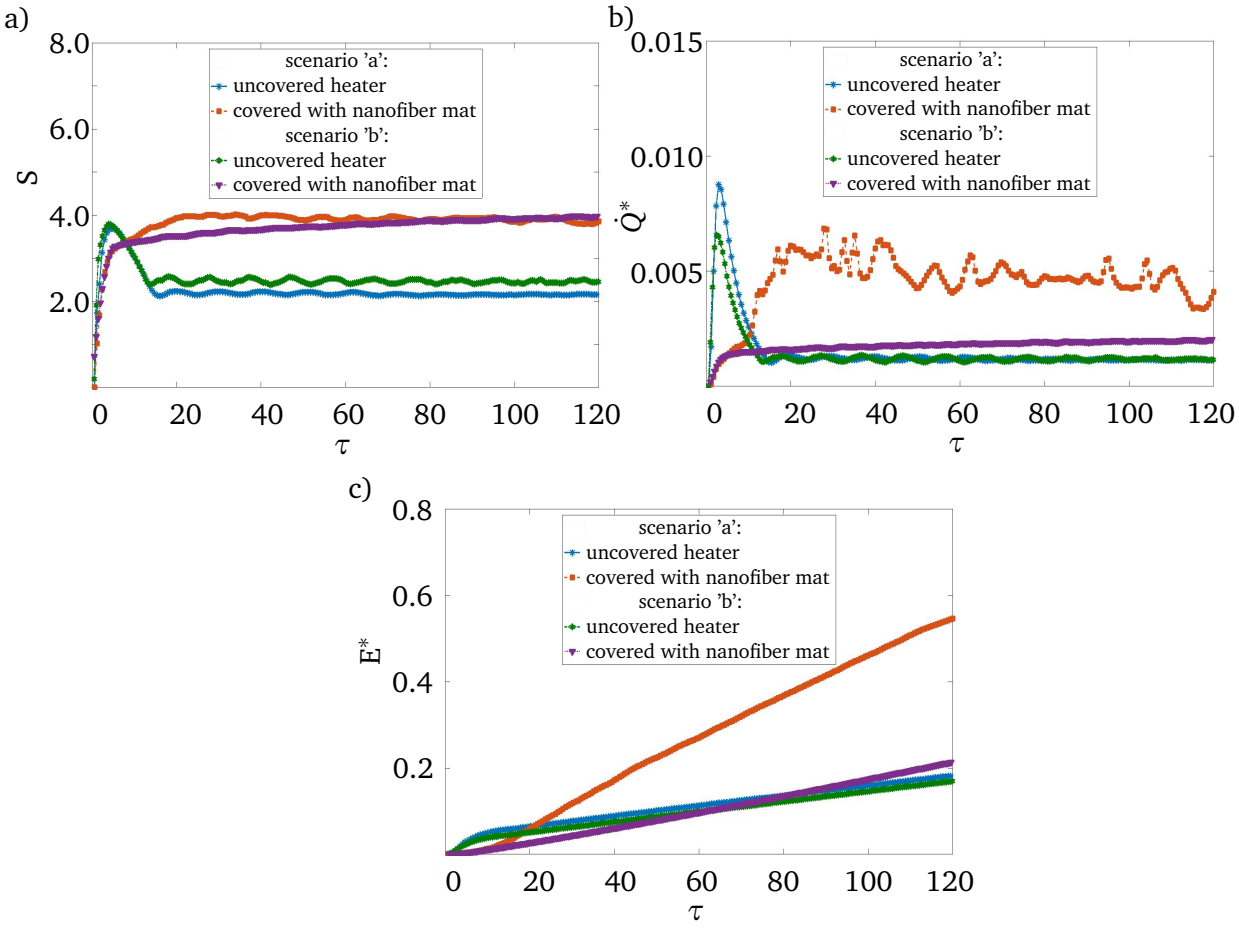

Figure A.7.: a) Spreading ratio, b) dimensionless heat flow, and c) dimensionless cumulative heat flow versus dimensionless time during the impingement of a single drop onto a bare and a nanofiber-coated heater for the parameters listed in Table 5.1.

Influence of wall superheat during the impingement of a single drop onto a nanofiber-coated heater:

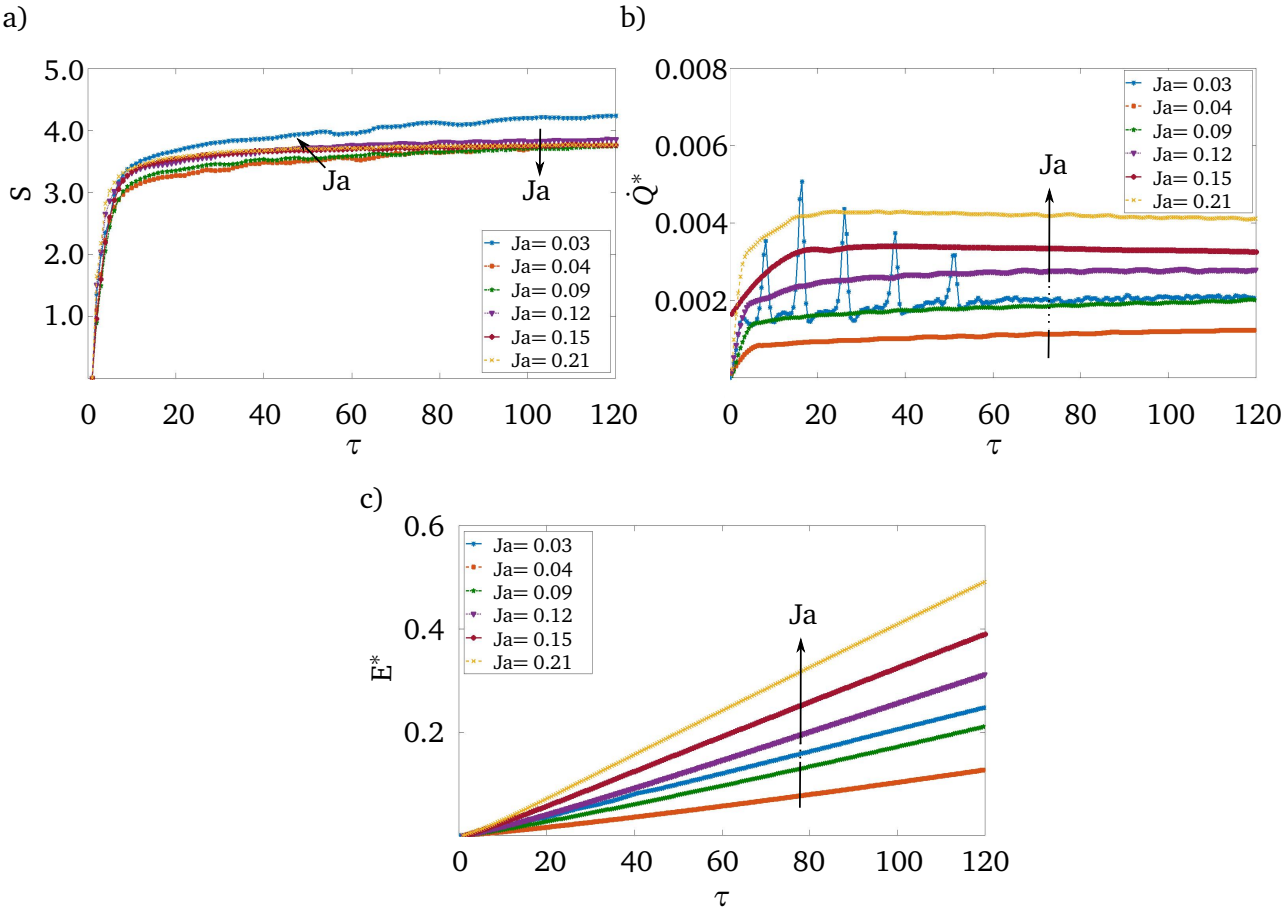

Figure A.8.: a) Spreading ratio, b) dimensionless heat flow, and c) dimensionless cumulative heat flow versus dimensionless time during the impingement of a single drop onto a nanofiber-coated heater for various Ja numbers ($h_{mat} = 22\ \mu$m, Re= 1550, We= 39, Bo= 0.4, Pr= 9.7, and $p_R = 0.05$).

Influence of impact velocity during the impingement of a single drop onto a nanofiber-coated heater:

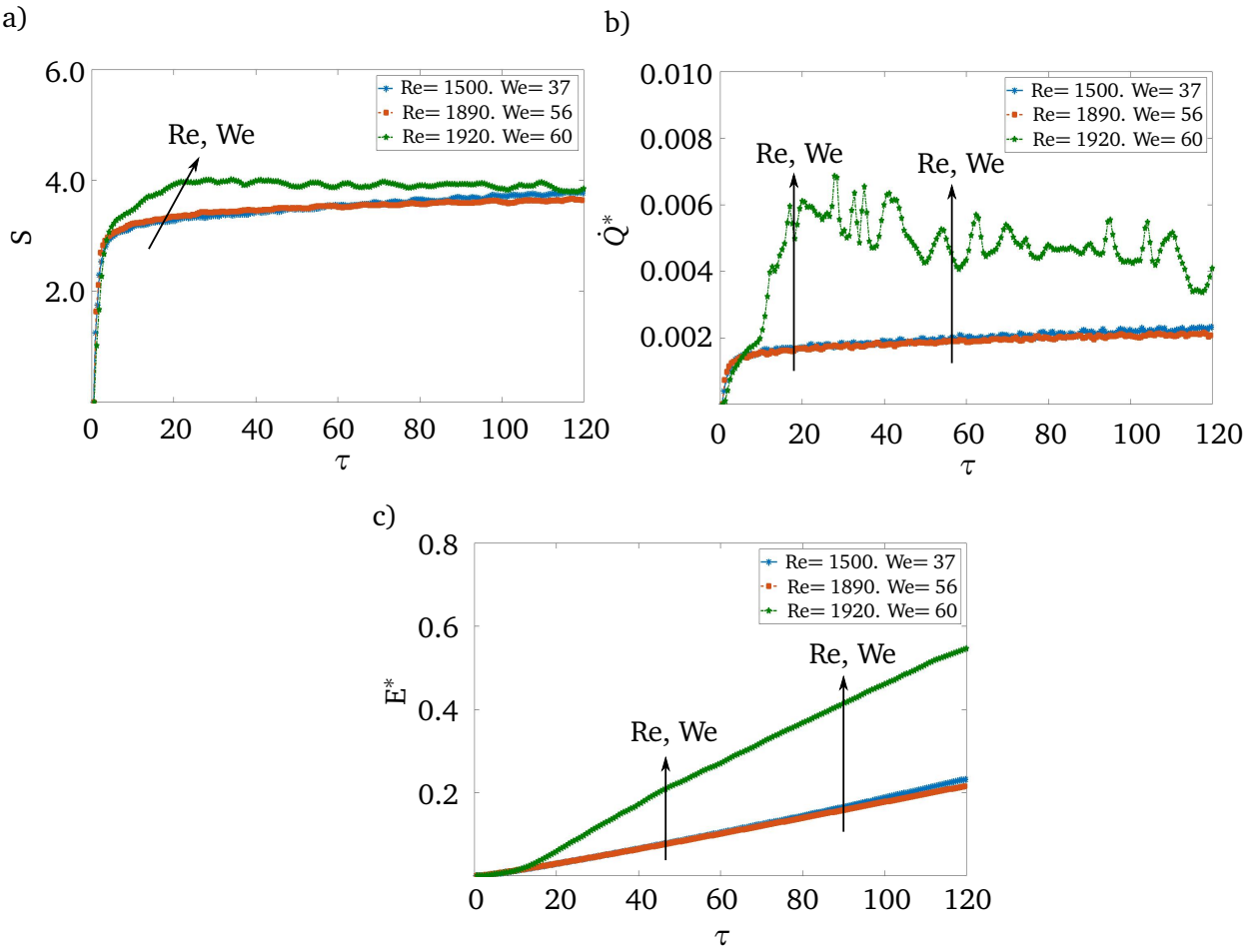

Figure A.9.: a) Spreading ratio, b) dimensionless heat flow, and c) dimensionless cumulative heat flow versus dimensionless time during the impingement of a single drop onto a nanofiber-coated heater for various Re and We numbers ($h_{mat} = 22\ \mu$m, Ja= 0.12, Bo= 0.42, Pr= 9.7, and $p_R = 0.05$).

Influence of nanofiber mat thickness during the impingement of a single drop onto a nanofiber-coated heater:

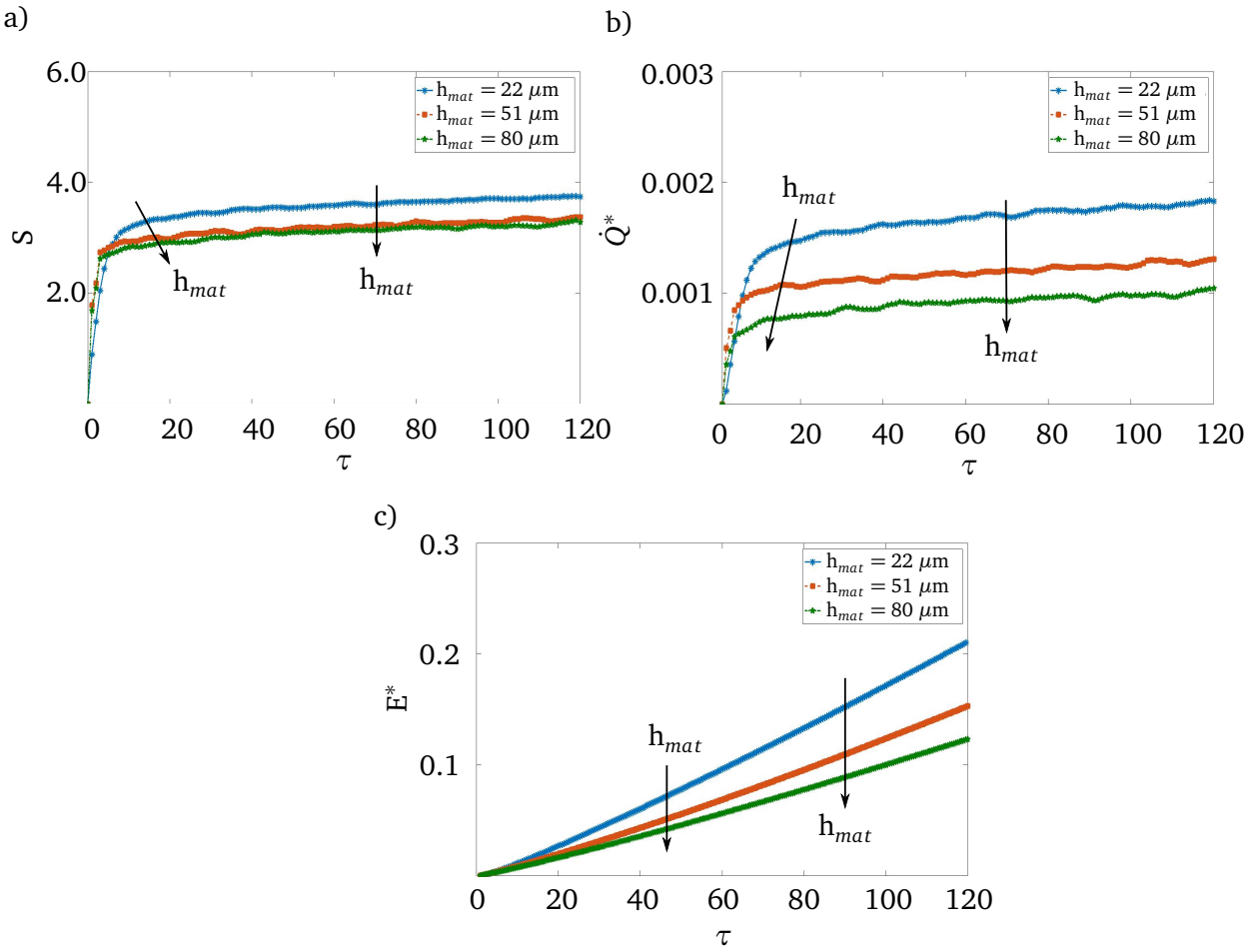

Figure A.10.: a) Spreading ratio, b) dimensionless heat flow, and c) dimensionless cumulative heat flow versus dimensionless time during the impingement of a single drop onto a nanofiber-coated heater for various mat thicknesses (Re= 1550, We= 39, Ja= 0.09, Bo= 0.4, Pr= 9.7, and $p_R = 0.05$).

A.4.2 Multiple drop impact

Influence of impact number during the vertical coalescence of multiple successive drops:

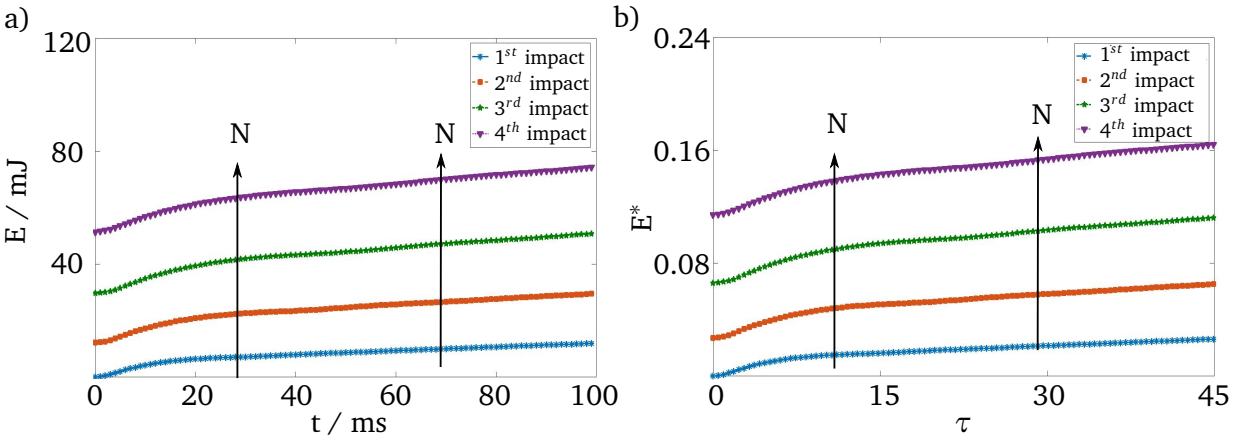

Figure A.11.: Temporal evolution of the cumulative heat flow in a) dimensional and b) dimensionless forms during the vertical coalescence of four successive drops impinging onto a bare heater ($D_0 = 1.14$ mm, $u_0 = 0.54$ m s^{-1}, $\Delta T = 12.4$ K, f= 10 Hz, Re = 2160, We = 64, Ja = 0.10, Bo = 0.6, Pr = 9.7, and $p_R = 0.05$)

Influence of wall superheat during the vertical coalescence of two successive drops impinging onto a bare heater:

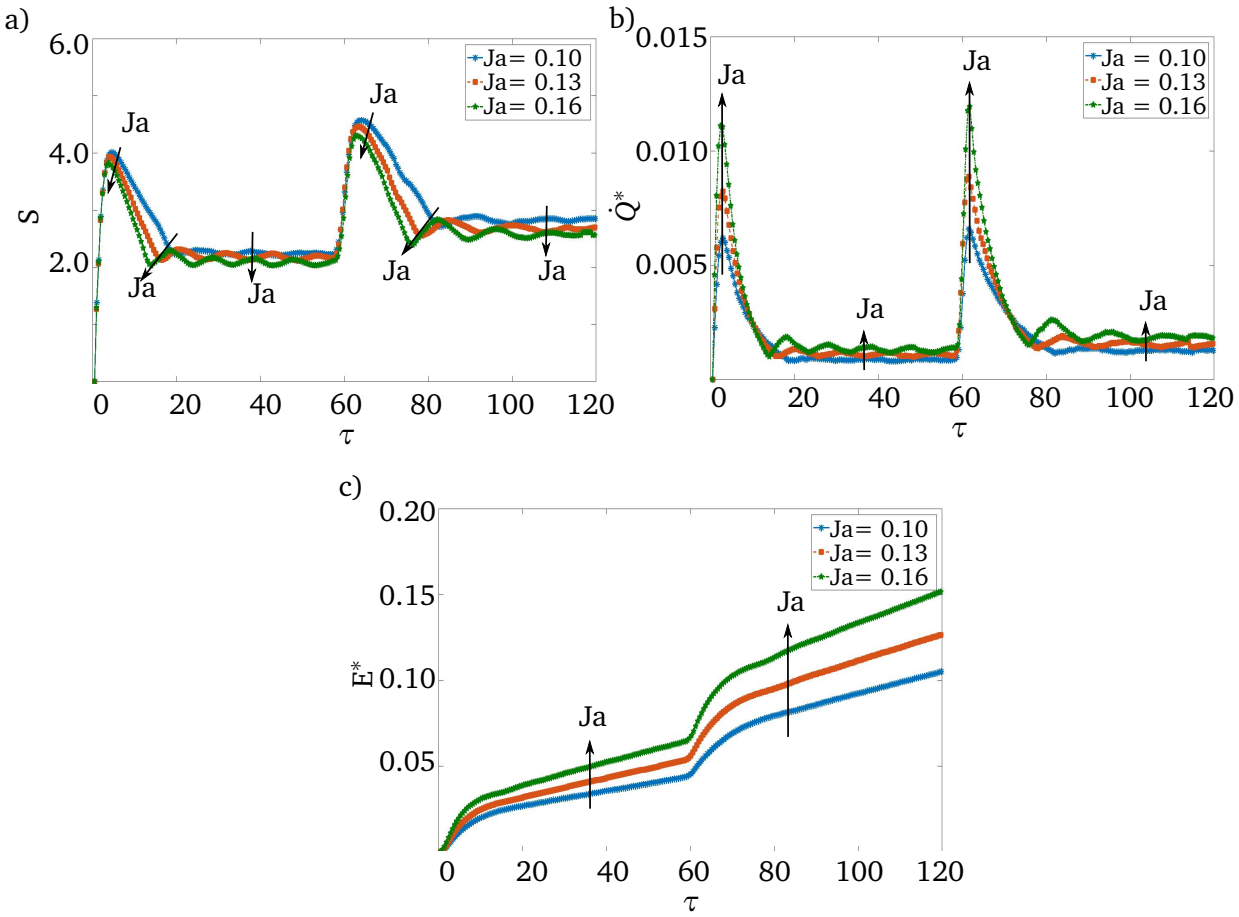

Figure A.12.: a) Spreading ratio, b) dimensionless heat flow, and c) dimensionless cumulative heat flow versus dimensionless time during the vertical coalescence of two successive drops impinging onto a bare heater for various Ja numbers (f= 10 Hz, Re = 2160, We = 64, Bo = 0.6, Pr = 9.7), and $p_R = 0.05$.

Influence of drop generation frequency during the vertical coalescence of two successive drops impinging onto a bare heater:

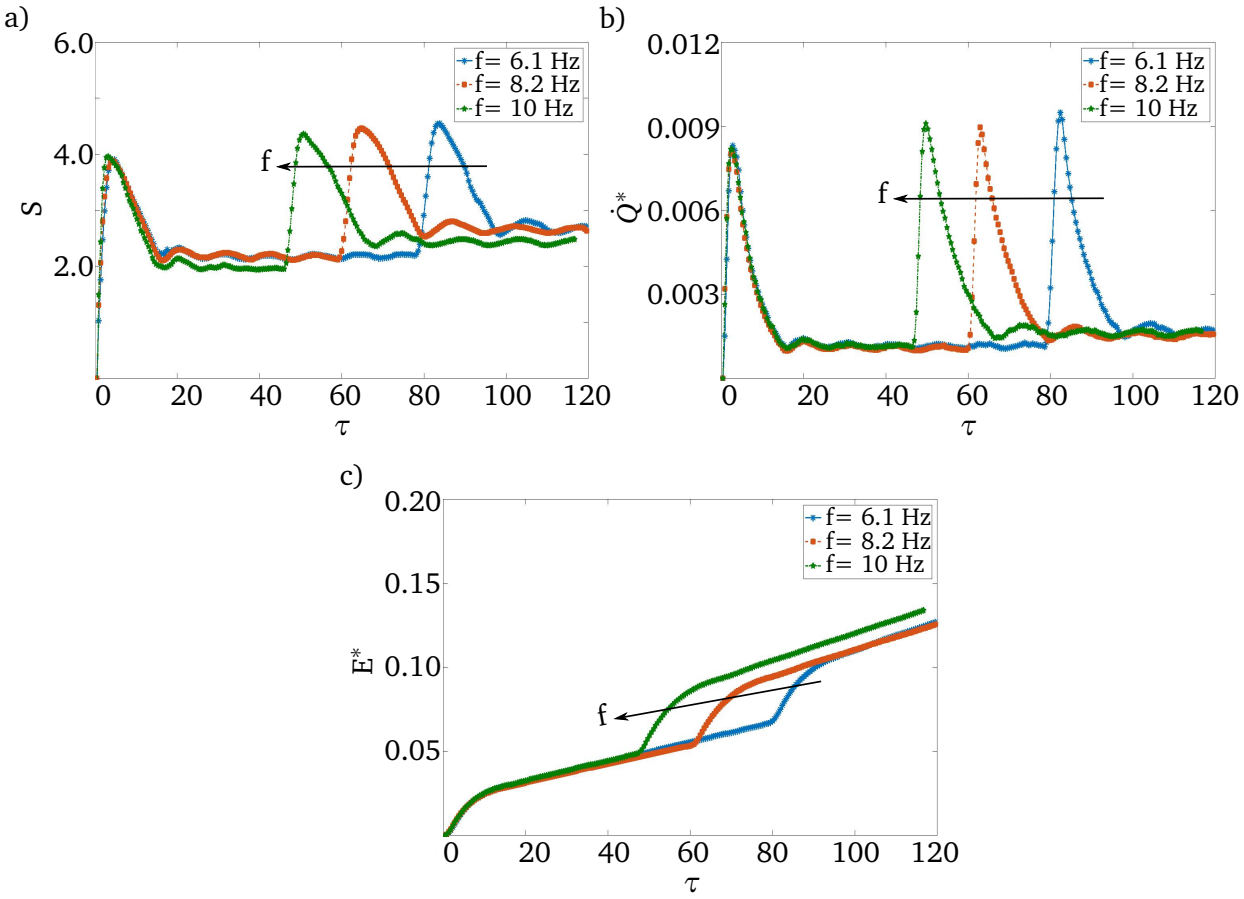

Figure A.13.: a) Spreading ratio, b) dimensionless heat flow, and c) dimensionless cumulative heat flow versus dimensionless time during the vertical coalescence of two successive drops impinging onto a bare heater for various drop generation frequencies (Re = 2160, We = 64, Ja = 0.13, Bo = 0.6, Pr = 9.7, and $p_R = 0.05$).

Influence of spacing parameter during the horizontal coalescence of two simultaneous drops impinging onto a bare heater:

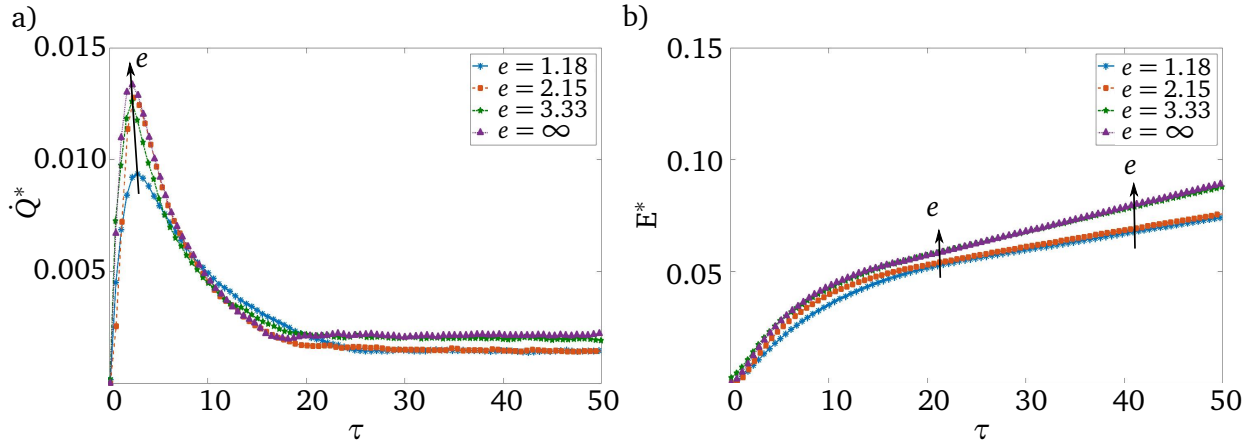

Figure A.14.: a) Dimensionless heat flow and b) dimensionless cumulative heat flow versus dimensionless time during the horizontal coalescence of two simultaneous drops impinging onto a bare heater for various spacing parameters (Re = 1710, We = 50, Ja = 0.09, Bo = 0.4, Pr = 9.7, and $p_R = 0.05$).

Influence of wall superheat during the horizontal coalescence of two simultaneous drops impinging onto a bare heater:

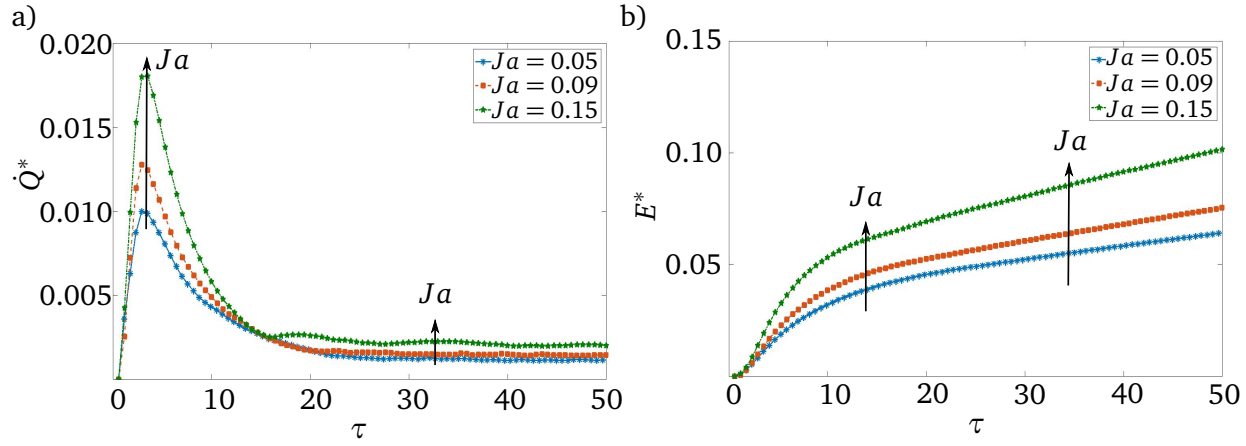

Figure A.15.: a) Dimensionless heat flow and b) dimensionless cumulative heat flow versus dimensionless time during the horizontal coalescence of two simultaneous drops impinging onto a bare heater for various Ja numbers (e = 2.15, Re = 1710, We = 50, Bo = 0.4, Pr = 9.7, and $p_R = 0.05$).

Influence of time interval during the horizontal coalescence of two non-simultaneous drops impinging onto a bare heater:

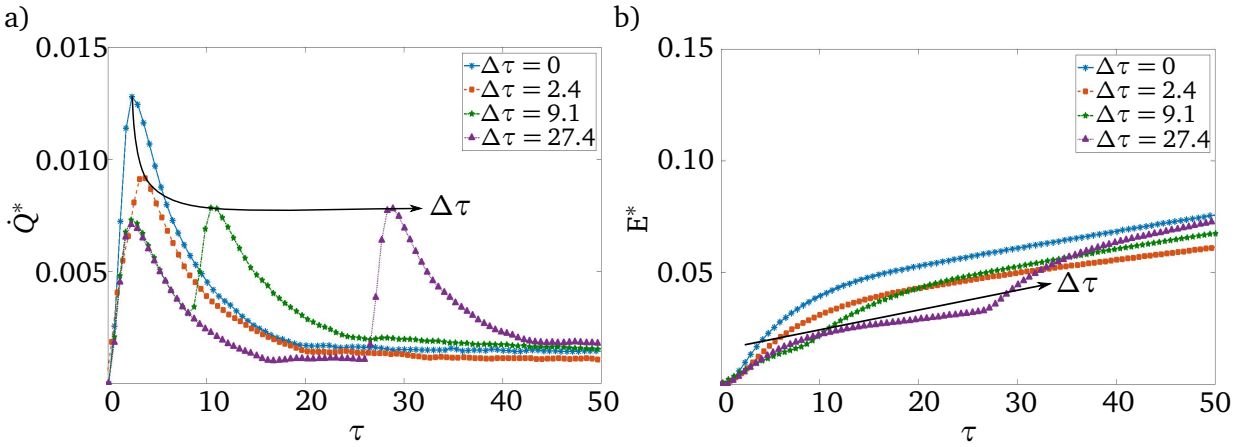

Figure A.16.: a) Dimensionless heat flow and b) dimensionless cumulative heat flow versus dimensionless time during the horizontal coalescence of two non-simultaneous drops impinging onto a bare heater for various dimensionless time intervals (e = 2.15, Re = 1710, We = 50, Ja= 0.09, Bo = 0.4, Pr = 9.7, and $p_R = 0.05$).

List of Figures

List of Tables